2012

Experimental Study of Lean Blowout with Hydrogen Addition in a Swirl-stabilized Premixed Combustor

Shengrong Zhu
Louisiana State University and Agricultural and Mechanical College

Follow this and additional works at: https://digitalcommons.lsu.edu/gradschool_dissertations

Part of the Accounting Commons

EXPERIMENTAL STUDY OF LEAN BLOWOUT WITH HYDROGEN ADDITION IN A SWIRL-STABILIZED PREMIXED COMBUSTOR

A Dissertation

Submitted to the Graduate Faculty of the
Louisiana State University and
Agricultural and Mechanical College
in partial fulfillment of the
requirements for the degree of
Doctor of Philosophy

in

The Department of Mechanical Engineering

by
Shengrong Zhu
B.S., Nanjing University of Aeronautics and Astronautics, Nanjing, China, 2005
December 2012

ACKNOWLEDGEMENTS

TABLE OF CONTENTS

LIST OF FIGURES

ABSTRACT

Lean premixed combustion is widely used to achieve a better compromise between nitric oxides emissions and combustion efficiency. However, combustor operation near the lean blowout limit can render the flame unstable and lead to oscillations, flashback, or extinction, thereby limiting the potential range of lean combustion. Recent interest in integrated gasification combined cycle plants and syngas combustion requires an improved understanding of the role of hydrogen on the combustion process. Therefore, in present study, combustion of pure methane and blended methane-hydrogen has been conducted in a swirl stabilized premixed combustor.

The measurement techniques implemented mainly include particle image velocimetry, CH*/OH* chemiluminescence imaging, planar laser-induced fluorescence imaging of OH radical. By investigating the flow field, heat release, flow-flame interaction, and flame structure properties, the fundamental controlling processes that limit lean and hydrogen-enriched premixed combustion with and without confinement have been analyzed and discussed.

As equivalence ratio decreases, for unconfined flames, the reduced flame speed leads flame shrinking toward internal recirculation zone (IRZ) and getting more interacted with inner shear layer, where turbulence level and vorticity are higher. The flame fronts therefore experience higher hydrodynamic stretch rate, resulting in local extinction, and breaks along the flame fronts. Those breaks, in turn, entrain the unburnt fuel air mixture into IRZ passing through the shear layer with the local vortex effect, further leading to reaction within IRZ. In methane-only flames, the width of IRZ decreases, causing flames to straddle the boundary of the IRZ and to be unstable. High speed imaging shows that periodic flame rotating with local extinction and re-light events are evident, resulting in high RMS of heat release rate, and therefore a shorter extinction time scale. With hydrogen addition, flames remain in relatively axisymmetric burning

structure and stable with the aid of low minimum ignition energy and high molecular diffusivity associated with hydrogen, leading to lower heat release fluctuation and a longer extinction time scale. For confined flames, however, the hydrogen effect on the extinction transient is completely opposite due to spiraling columnar burning structure, in comparison of a relatively stable conical shape in methane flames.

CHAPTER 1 : INTRODUCTION

1.1   Background and Motivation

As government environmental regulations become progressively stringent and public concern on the control of pollutant emissions increases, there are more considerable challenges imposed for the gas turbine industry. For example, most dry-low-NOx (nitrogen oxides) engines emit NOx below 25ppm and CO below 50ppm (both corrected at 15% O_2), and now target at ultra-low emission of less than 5ppm of NOx [1]. Several effective strategies for reducing NOx emissions have been developed to achieve the aggressive combustion emissions goal, including catalytic combustion, selective catalytic reduction (SCR), lean premixed combustion, water injection into the reaction zone as a dilutant, and rich burn-quick quench-lean burn (RQL) combustion [2, 3, 4, 5]. Of the above techniques, the one most widely implemented is lean-premixed combustion, as it not only reduces pollutant formation by the thermal mechanism, which is to burn fuel at lower temperatures and prevent the high energy needed for NOx formation and thereby minimize NOx formation, but also increases plant efficiency due to its implementation simplicity lowering the hydrodynamic head losses [6]. Therefore, modern premixed gas turbine combustors are usually operated at lean fuel conditions for reducing the production rate of NOx [7, 8].

In lean premixed combustion, once the rates of heat release and chemical radicals resulted from combustion reaction are insufficient to sustain the favorable reaction condition for a given flow velocity, flame will be detached from its stabilization location and physically convected out, or blown out, of the combustor. This is usually referred to as lean blow out (LBO). The lean flammability limit or lean blowout limit refers to the

condition at which LBO occurs, that is, when the time required for chemical reaction becomes longer than the characteristic flow residence time. The operation near the LBO limit, however, may induce undesirable combustion characteristics, such as a high level of noise and combustion instabilities caused by local flame extinction and heat release fluctuations, leading to poor combustion efficiency and poor operability of the combustor. The heat release fluctuations when appropriately coupled with the acoustics can lead to large pressure and velocity fluctuations near the dump plane, with the latter serving as a precursor to flashback especially with fuels associated with higher flame speeds such as hydrogen. To avoid LBO and the associated negative effects, modern premixed gas turbine combustors have to be operated with a relatively large margin from the LBO limit [9]. In order to extend the range of combustor operation closer to LBO, It is therefore of interest and desired to better understand the combustion characteristics close to LBO limit, and physical mechanism associated with LBO process.

Over the past several decades, extensive numerical and experimental studies on LBO phenomena have been conducted, including LBO observations characterized by large scale unsteadiness, and local extinction and re-ignition [10, 11, 12, 13, 14, 15]. LBO scaling as a function of combustion parameters (incoming flow velocity, equivalence ratio, pressure, temperature and fuel type) have been reported for specific combustor configurations [16, 17, 18, 19, 20, 21], and active or passive control strategies to extend LBO have been explored [15, 22, 23, 24, 25]. Several LBO mechanisms have been proposed, and include: balance between the rate of entrainment of reactants into the recirculation zone and the rate of burning [26], energy balance between heat supplied by the hot recirculating flow to the fresh gases and that released by reaction [27, 28, 29,30],

balance between contact time between the combustible mixture and hot gases in the shear layer and chemical ignition time [27, 31, 32, 33], and mechanisms related to local extinction by excessive flame stretch with a flamelet based description [34, 35, 36]. However, definitive conclusions on LBO remain a key challenge and need further investigation [36,37]. This is particularly true for blended fuels such as Syngas where hydrogen is often present along with carbon monoxide, methane and other gases.

It is widely accepted that both flow behavior and chemical kinetics play a role in the LBO, but their relative roles on this phenomenon need further clarification. In addition, Zhang et al [38] observed that the averaged flow field structure did not change with a fixed adiabatic temperature for a methane flame, or flames with 20%, 50%, and 75% H_2. This indicated that for the range of conditions studied chemical kinetics does not affect the flow field structure. In a bluff body stabilized premixed flame, however, it has been reported that near blowoff the structure of reacting flow field appears to be changed back to the sinuous structure observed in non-reacting flow, randomly oscillating between a spatially well-organized sinuous flow structure and something more symmetric [36]. This observation implies that we cannot simply attribute LBO to a decreasing temperature ratio as equivalence ratio decreases.

Moreover, it should be emphasized that the flame front involves key issues such as flame-vortex interaction, flame-wrinkling, flame holding and their relations to the flow field and turbulence levels. Therefore, it is believed that flame front instabilities play important roles in the blowout process in view of the reported observations of flame pulsations and flicker before the flame actually blows out [39, 40]. Experimental results have shown that combustion in most practical devices takes place in the so-called thin

3

laminar flamelet regime [41, 42], where small turbulent eddies can enter the preheat zone but not the inner reaction layer. In this regime, turbulent effects on flame structure are dominated by the flame curvature [41]. To understand the turbulent premixed combustion in this regime, the flame surface properties are of primary importance. Thus, it is important to examine the flame structure behavior in terms of its location, shape, curvature and orientation angle as the LBO limit is approached. These statistics contain the effects of the key postulated mechanisms for LBO pertaining to flame-vortex interactions, flame stretch and flame front instabilities.

Additionally, near blow-out, the typically unsteady flame is more sensitive to external perturbation. Thus, the confinement of the burner, influencing the flow motion, could have a significant effect on flame dynamics during LBO process. In a swirl stabilized burner with unconfined configuration, the flow field is characterized by an internal recirculation zone resulting from the vortex breakdown of the swirling flow and entrainment of ambient air. Flame is essentially affected by vortices shed from the edge of injector, and the flame response is dominated by this flame-vortex interaction [43, 44]. With confined configuration, the flow field pattern is altered by the presence of side walls, and features an internal recirculation zone and a corner recirculation zone. Both these two zones carry hot combustion products back to the burner exit, which provide a continuously stable source of heat and active species for flame ignition. Furthermore, the flame dynamics is effectively controlled by large structures induced by the resonant acoustic modes of the system. Further, the flame may directly interact with the wall if the chamber is relatively narrow and heat losses through the shell may play a role in the flame behavior. Kulsheimer et al. [45] reported that the flame response is modified by

4

confinement at moderate frequencies. Archer [46] found there are significant differences between unconfined and confined swirling flames in terms of the width and length of the IRZ, the velocity decay and the reverse flow velocity, the thermal time scales, and turbulence levels. Since a large number of studies appear in the literature on unconfined flames, and conclusions are generalized for a range of practical applications that are typically confined, it is therefore of interest to investigate and compare the LBO processes under both confined and unconfined conditions.

Hydrogen has a wide flammability range, low minimum ignition energy, and high flame speed. Therefore, hydrogen-enriched fuel has the benefit of extended lean flammability limits that allows stable ultra-lean combustion at lower temperatures needed to minimize the NOx production without any adverse effect on the combustion emissions of CO and unburned hydrocarbons. It may be assumed that the higher combustibility of the added hydrogen may increase NOx emission due to higher flame temperature (at a constant equivalence ratio), but this fact could be offset by the ability to burn an overall leaner mixture [47, 48, 49, 50] so that lower thermal NOx is produced. However, there are several challenges with hydrogen addition. The main challenge is the susceptibility to flashback due to increased flame speeds associated with hydrogen content. For example, the flame speed of a stoichiometric methane air mixture is about 40 cm/s whereas that of a hydrogen air flame is about 210 cm/s at 1atm and room temperature [51]. This mismatch between flame speeds leads to flame holding problems in a gas turbine engine environment. Additionally, in a lean flame, the preferential diffusion instability associated with hydrogen content will trigger the flame front instabilities, and cause it to be more wrinkled and convoluted. This thermo-diffusive instability is also likely to play a

5

role in the LBO. Since hydrogen addition is likely to improve the LBO limit [1, 21, 38], but with added complexities of flashback, increased flame-wrinkling etc, it is important to understand the controlling mechanisms associated with LBO in hydrogen enriched flames. This need serves as the primary motivation for the present study.
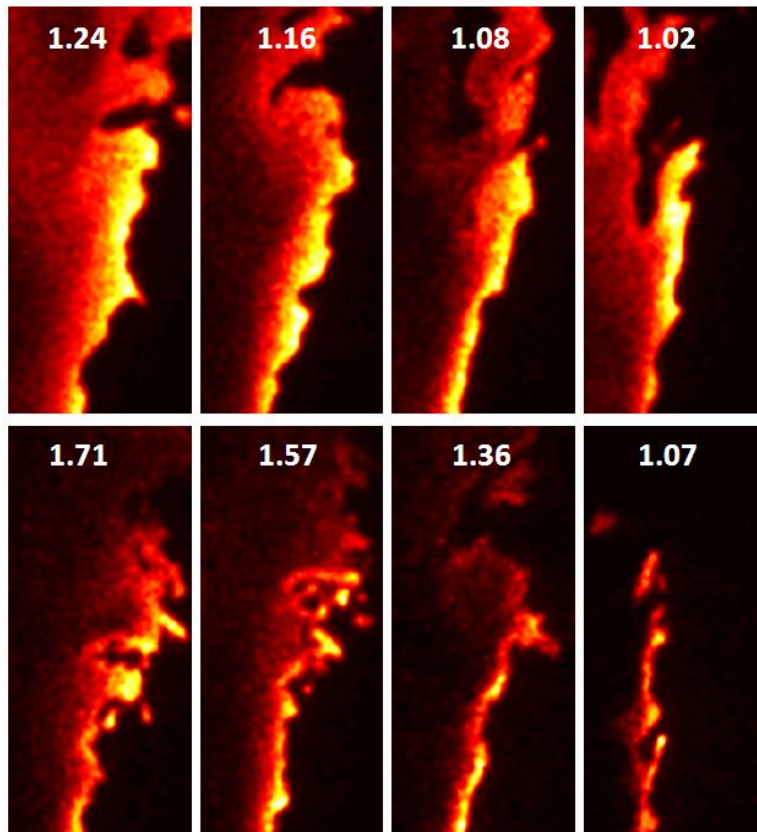
Figure 1-1 OH-PLIF images. Top row: methane flames. Bottom row: hydrogen flames. Ratios of Φ/Φ_{LBO} are shown in corresponding images.

In fact, the study of blending hydrogen into traditional fuel is also motivated by the need of finding alternative energy sources for traditional hydrocarbon fuels. With the significant increase of energy consumption and ever more challenging environmental regulations, alternative clean energy resources gain increasing attention. For example, coal-based Syngas is an environmentally clean source of energy, and typically composed

of primarily hydrogen and carbon monoxide, but the relative compositions vary widely depending on the coal source. Syngas fuels can improve flame stability. Such strategies have been investigated in laboratory scale flames with similar geometries to the ones used industrially. Several investigations have been reported [52 , 53] where the characteristics of Syngas flames have been examined. Again, this kind of hydrogen-enriched fuel is susceptible of flashback or prone to be thermo-diffusively unstable flame.

Table 1-1 Comparison of fuel properties of H_2, CH_4, and C_3H_8 at 300K and 1atm

Property	Hydrogen	Methane	propane
Molecular weight(g/mole)	2.016	16.043	42.080
Density(kg/m^3)	0.08	0.65	1.96
Mass diffusivity in air (cm^2/s)	0.61	0.16	0.10
Minimum ignition energy(mJ)	0.02	0.28	0.26
Flammability limits in air (Vol%)	4-75	5-15	2.1-9.5
Flammability limits (Φ)	0.1-7.1	0.5-1.67	0.52-2.36
Stoichimetric adiabatic flame temperature(K)	2480	2214	2268

Table 1-1 lists the comparison of some fuel properties. Figure 1-1 shows 2-D OH-PLIF fluorescence images for methane and hydrogen flames. It evidently shows for methane flames the reaction zones, bright yellow regions in fluorescence images, are winkled but connected, while for hydrogen, they are strongly localized and isolated as indicated by dark regions (flame extinction) in between bright yellow spots, especially as equivalence ratio decreases. This is typical flame burning structure for lean hydrogen flames due to its high preferential diffusivity, that is, cellular burning structure of strongly localized intense reaction and extinction. This unique characteristic associated hydrogen flames could result in modified LBO process, compared to methane flames.

7

In summary, lean premixed combustion is widely accepted as a favored strategy for meeting aggressive combustion emissions target, but it also imposes some operational challenges particularly with respect to combustion dynamics since lean premixed combustion is operated near the lean flammability limit. Adding hydrogen into the traditional fuel does enhance the lean flammability limit but the flame is prone to thermo-diffusively instability. Thus, it is tempting to explore the physical fundamental mechanisms of LBO, for better understanding its physical and chemical controlling processes, shedding light on more accurate predication and development of corresponding effective mitigation control techniques.

Therefore, in this study, the main goal is to expand the knowledge base concerning the fundamental controlling processes associated with LBO in hydrogen-enriched premixed combustion. This is done by experimentally investigating the flow field, the reaction zone, heat release, flow-flame interaction, and the flame structure properties as flame approaches the LBO limit. Measurements in the flame are made with 2-D/3-D particle image velocimetry (PIV), which is a non-intrusive, laser-based diagnostic technique for velocity measurements, CH*/OH* chemiluminescence imaging, Mie scattering imaging, planar laser-induced fluorescence (PLIF) imaging of OH radical. These data are then analyzed to generate some key mechanistic conclusions about LBO in methane and hydrogen-enriched flames.

1.2 Dissertation Outline

The structure of this dissertation is arranged as follows. In Chapter 1, LBO issue is addressed and the published studies are reviewed, and then followed with the study

objectives and a brief experimental methodology. Chapter 2 provides some relevant background of premixed combustion which is employed here. Chapter 3 describes the experimental setup, instrumentation, and data acquisition methods. Chapter 4 details some major data processing techniques. Chapter 5-8 present experimental results of PIV and chemiluminescence imaging, flame structure properties, synchronized PIV and OH-PLIF measurements, and high speed imaging at LBO limits. Chapter 9 includes the summary of this dissertation and recommendations for future work.

CHAPTER 2 : BACKGROUND

2.1   Chemiluminescence

Chemiluminescence is the light of electromagnetic radiation via the energy release from a chemical reaction, in which the molecules are returning from chemically (rather than thermally) excited energy state to their low energy or ground state. The simplicity of the detection system for chemiluminescence emissions makes it attractive as an analytical diagnostic tool for flames and combustion processes. In hydrocarbon flames, the strongest chemiluminescent signal peaks are generated by hydroxyl radical (OH*) and methylidyne radical (CH*), and main measurement-targeted emissions of chemiluminescence are OH*, CH*, C_2*, and CO_2*. OH* signal peaks at 309 nm due to $A^2\Sigma^+$-$X^2\prod$ transition, and it is the strongest features of most flame spectra; CH* presents three emission bands centered at 431, 390, and 314 nm respectively, with the first two being the strongest and corresponding respectively to the $A^2\Delta$-$X^2\prod$ and to the $B^2\Sigma^-$-$X^2\prod$ transitions; C_2* intensity peak is located close to 515nm, while CO_2* emission contributes to the continuum signal in the range of 310-600 nm in fuel-lean hydrocarbon flames [54].

As qualitative markers of flame front locations, both OH* and CH* emissions are used widely, because the maximum OH* intensity is near the maximum flame temperature [55] and CH* profile presents in a thin, high-temperature region [56]. As to the indications of heat release of combustion, all four aforementioned emissions are reported [57, 58, 59, 60] with certain uncertainty due to the influence of combustion parameters, i.e., equivalence ratio, pressure, temperature, and flame strain rate. In addition, the ratio of CH*/OH* spatially and temporally resolved and corrected with the

background signal of CO2* is also applied on determination of local equivalence ratio and heat release rate in [61]. In this study, OH* and CH* are used to indicate the flame reaction zone.

2.2 Flame Front Instability

Considering that most typical combustion systems are located in so called flamelet regime [62], where the flame fronts are wrinkled and propagate in form of relatively thin inner structure similar to laminar flame, the mechanisms responsible for laminar flame front instabilities are briefly reviewed. They mainly include hydrodynamic instability well known as the Rayleigh-Taylor instability, Darrieus-Landau instability, and differential diffusion instability. The first two are caused by the discontinuity of density, while the last one arises from unequal diffusivities including the thermal and mass diffusivities of unburnt and burnt gases. In fact, it has been reported that these mechanisms influence the turbulent flame speed under moderate values of the Reynolds number [63, 64].

For an upwardly propagating spherical flame, the lighter burnt gases are present within denser unburnt reactants, and then the gravitational effects will lead to the body force instability, that is, Rayleigh-Taylor instability. In this case, contribution from body force instability should be considered for the flame front instability.

When the chemical reaction time is much shorter than the flow characteristic time and the reaction zone can be regarded as to a passive surface such that the infinitely thin interface separates the low density combustion products and high density reactants, such discontinuity of densities on both sides of flame fronts will lead to the expansion of the

stream-tubes in both portion of flame fronts toward to burnt gases and portion of flame fronts toward to unburnt gases, which is so called Darrieus-Landau instability [65, 66]. And these deflections consequently cause a pressure gradient and further increase the initial displacement of flame fronts as the flame speed remains unchanged due to flame structure not affected, and they will finally lead to unconditionally unstable flame [67], if only hydrodynamic stretch is considered.

Differential diffusion instability is essentially caused by the non-uniform diffusivities of reactant gases and product gases. As is well known, flame propagating speed is significantly influenced by local flame temperature and the availability of active radicals for chemical reactions. So, the heat conduction and the diffusion of burnt and unburnt gases between two sides of flame fronts will play an important role in the further progression of wrinkled flame fronts induced by any perturbation. That means three diffusivities need considering: thermal diffusivity of unburnt gases D_{th}, mass diffusivity of deficient reactant $D_{m,def}$, and mass diffusivity of excess reactant $D_{m,exc}$. Lewis number, defined as $Le = {D_{th}}/{D_{m,def}}$, represents the thermo-diffusive effects. When Lewis number is less than unity, the mass diffusion of deficient reactant is faster than the thermal diffusion. Thus the crest of the wrinkled flame fronts toward unburnt gases will gain deficient reactant faster than heat loss, while the trough of the wrinkled flame fronts toward burnt gases will lose deficient more rapidly than heat gain. As a result, the flame speed of the crest will increase and that of the trough will decrease, leading to the amplification of the wrinkling perturbation. Then the flame will be thermo-diffusively unstable. When Lewis number is greater than unity, in the same line of reasoning, the flame speed of the crest will decrease and that of the trough will increase, resulting in

counteracting the wrinkling and smoothing the flame fronts and rendering the flame thermo-diffusively stable. As to the preferential diffusion instability, it refers to the shift of local equivalence ratio happening in the crest of flame fronts toward the unburnt gases when the deficient reactant diffuses faster than excess reactant.

2.3   Characteristics of Swirling Flow

To stabilize the flame in high velocity reactant streams, swirl based stabilization method is most widely applied in industrial burners, furnaces, and gas turbine combustors. Swirling flows were originally used to improve and control the mixing rate between fuel and oxidant streams to achieve flame geometries and heat release rates appropriate to the particular process application [68]. A sufficiently strong swirl creates an adverse pressure gradient in the jet core, which cannot be overcome by the kinetic energy of the fluid elements flowing in the axial direction, leading to a vortex breakdown, i.e., the formation of a closed, standing, toroidal vortex with flow reversal in the core region. The reverse flow carries hot combustion products back to the burner exit thus providing a continuously stable source of heat and active species for flame ignition of the flesh incoming mixture entrained and mixed by enhanced shear layer around the recirculation region, so that a combustion favorable condition is established. By altering the flow field (flow Reynolds number), swirling strength, and in turn the strength of the re-circulating zones, the flame could be forced to reside in either of the re-circulating zones or on the shear layer between the re-circulating zones. Considering the flow dynamics play an important role in flame stabilization, the characteristic of swirling flows, especially the involved vortex breakdown, is briefly reviewed.

13

The swirl intensity is usually characterized by the swirl number S, defined as the ratio of the axis flux of the tangential momentum to the product of the axial momentum flux and equivalent exit radius [69]. For a typical single element injector with a flat vane swirler,

$$S = \int_{R_h}^{R_n} \bar{v}\bar{w}r^2 dr / \int_{R_h}^{R_n} R_n \bar{v}^2 r dr \tag{2-1}$$

where R_n and R_h are the radii of the center-body and the inlet duct, respectively; v and w are the axial and tangential velocity, respectively.

If the axial and tangential velocities are assumed to be uniform and the vanes are very thin, the swirl number expression can be reduced as follows, geometrical swirl number [70],

$$S = \frac{2}{3}\left[\frac{1 - (R_h/R_n)^3}{1 - (R_h/R_n)^2}\right] tan\varphi \tag{2-2}$$

where φ is the swirler vane angle. For a hub-less swirler, it can be simplified as,

$$S = \frac{2}{3} tan\varphi \tag{2-3}$$

The vortex breakdown involved in swirling flows manifests itself as a sudden change in shape along the vortex lines, leading to redistribution of the axial momentum into radial direction. By varying, systematically and independently, the flow rate and the circulation imparted to the flow fluid (water) in a slightly diverging cylindrical tube, Sparkaya [71] observed three types of vortex breakdown: axisymmetric/bubble, spiral and double helix. In fact, there are seven distinct modes of breakdown [72], however, at high Reynolds numbers, the bubble and spiral modes are the only characteristic geometric forms [73]. The bubble mode usually dominates at high swirl numbers, while the spiral mode occurs at low swirl numbers.

Swirl injector   Corner recirculation zone   Vortex-breakdown-induced center recirculation zone

Shear layers   Precessing vortex core
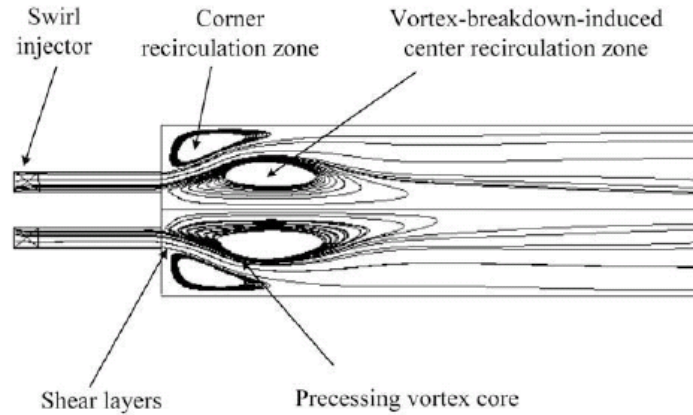
Figure 2-1 Typical flow structures in swirling flow [74].

A typical flow structure of swirling flow with bubble type includes a vortex breakdown induced center recirculation zone, inner/outer shear layers, and area expansion induced corner recirculation zones, as shown in Figure 2-1. This bubble structure is nearly axisymmetric and the interior of the center recirculation zone is dominated by low frequency motions. Fluid exchange with the outer flow occurs at the downstream end of the bubble by a simultaneous filling and emptying process via the toroidal vortex ring, possibly due to pressure instabilities in the wake of the bubble [71].

The spiral breakdown is characterized by a rapid deceleration, an abrupt kink, a corkscrew-shaped twisting of the fluid elements, and finally followed by large-scale turbulence, with the rotation of the whole spiral form around the axis. The frequency of this precessing vortex core (PVC) depends on the swirl level and flow rate. The whole structure is widely observed rotating with the outer flow, but the sense of the winding of the spirals has been observed to be both the same [71, 75] and "unmistakably opposite" [76, 77] to that of the swirling flow. It is the latter pattern, as emphasized in [78], that induces velocity deceleration at the centerline and even formation of a center

recirculation zone, providing conditions for flame holding. Therefore, it is important to determine which mode the actual flow presents with.

With the fact that both bubble and spiral types of vortex breakdown are observed in combustion [71, 79, 80, 81], it is necessary to understand the transition between these two modes. The bubble type may evolve either from a double helix, a spiral, or directly from an axisymmetric swelling of the vortex core, and the mode of evolution depends on the particular combination of the Reynolds number and the swirl level [82]. As shown numerically in [83], the increases in the swirl level, in the negative pressure gradient, or in the degree of divergence of the flow promote further upstream movement of a breakdown and the transition from a spiral type to a bubble type, and vice versa. There may be some special ranges of flow settings under which the two or more types of vortex breakdown can exist and transform spontaneously into each other by increasing or decreasing swirl level, as so called a hysteresis region in [82], but it should be emphasized that any transformation between two types will involve the axial movement of the breakdown position [75].

CHAPTER 3 : EXPERIMENTAL SETUP

3.1   Introduction

In this chapter, main experimental apparatus used in this dissertation work is introduced. This experimental apparatus described here is stationed at the combustion lab under Turbine Innovation and Energy Research (TIER) Center in Louisiana State University.
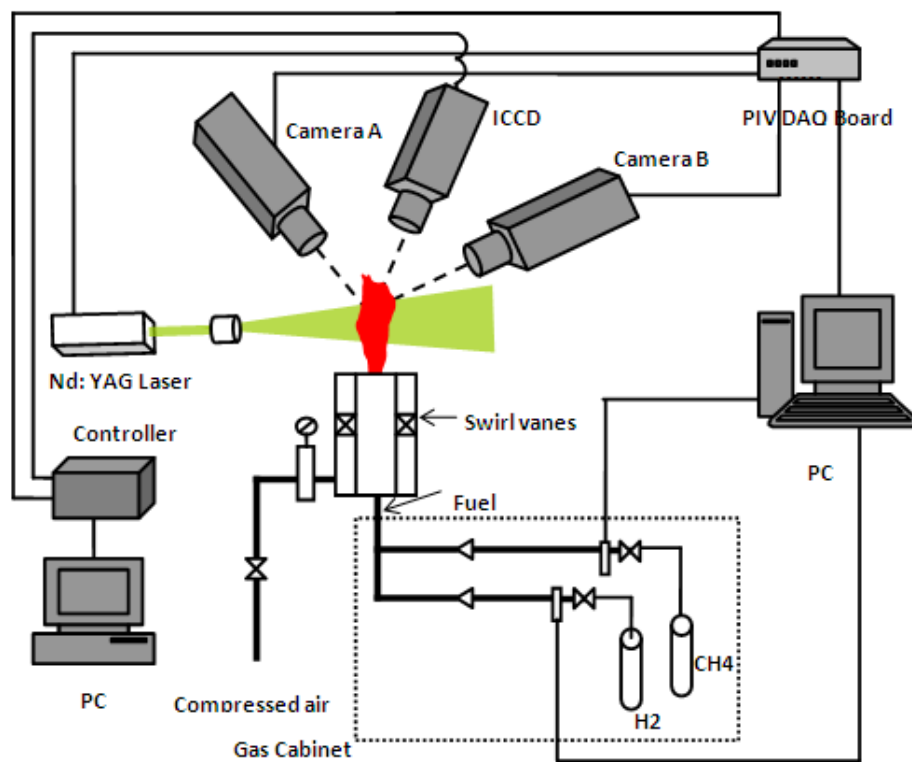
Figure 3-1 Schematic view of experimental setup

Figure 3-1 shows the schematic view of a typical experimental setup for simultaneous measurements of 3D-PIV and chemiluminescence imaging. The experimental setup includes air/fuel sources, a swirl-stabilized premixed combustor, a PIV system for Mie-scattering imaging and flow velocity measurement, and an ICCD

camera for chemiluminescence emissions measurement. The combustor consists of the inlet fuel and air-delivery system, and the premixing section. The flame is swirl-stabilized and attached to the center-body at the dump plane for measurement conditions in this study. The ICCD camera is located in between two PIV cameras but all cameras are placed in the same side of laser sheet for PIV measurement. The specific experimental configuration for a certain measurement in chapter 5-8 is different but similar to Figure 3-1. More details on the experimental setup in this study are described in the rest sections of this chapter.

3.2   Burner
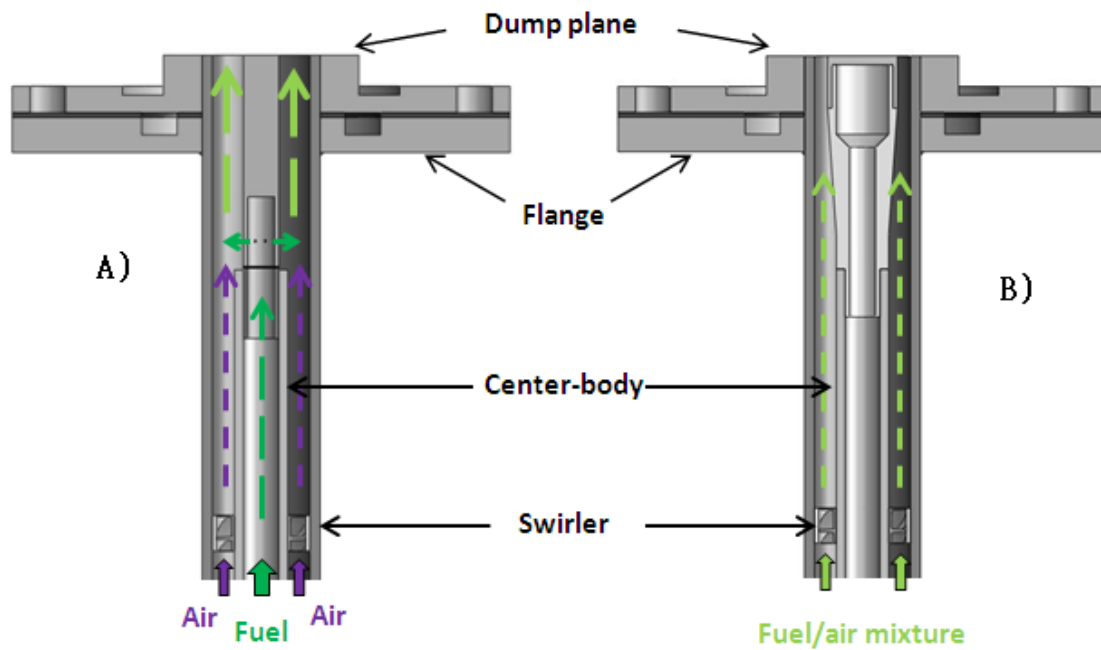
Figure 3-2 Sectional view of burner with two configurations

In this study, two different types of burner configurations, configuration A and B, are employed throughout this dissertation, as shown in Figure 3-2. The most used one is

the one with configuration B, as further shown in Figure 3-3. In Figure 3-3, A 45° swirl vane is fitted with a hollow center body. This center body extends beyond the swirl vane and is flush with the dump plane of the combustor. The exit diameter of the center body is 25.4 mm (1.0 inch) and the O.D. of the swirler is 34.9 mm (1.375 inch). The geometric swirl number is calculated to be S_g=0.76. Methane or hydrogen-enriched fuel mixture, and the air are injected radially into the annular air-fuel delivery system, 533 mm (21 inch) upstream of the dump plane, to ensure that the fuel and air is well premixed.
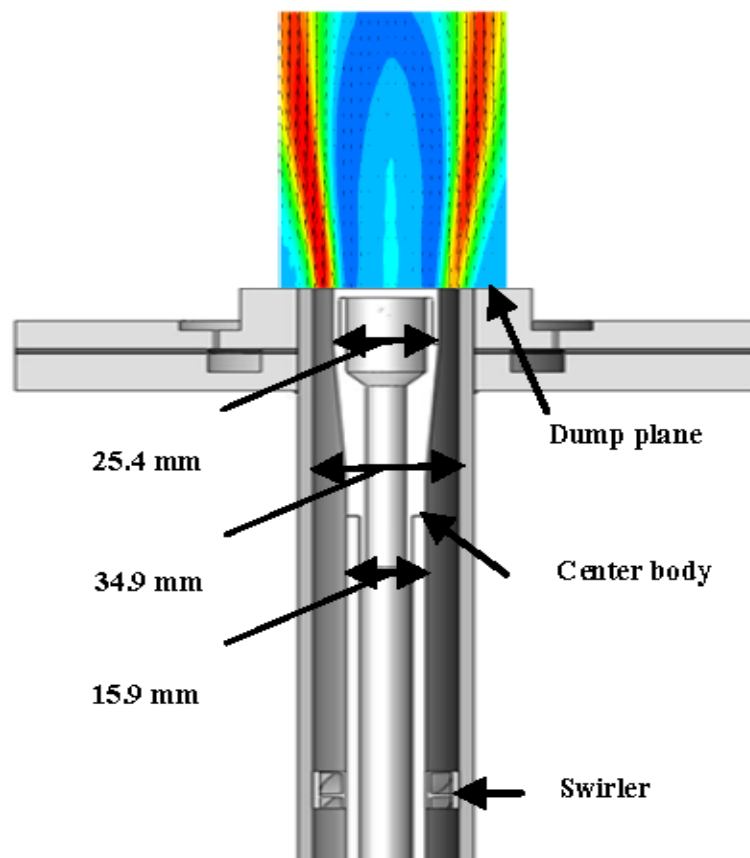
Figure 3-3 Sectional view of the burner with configuration B

Experiments show that the combustor with configuration A in Figure 3-2 can be operated only up to around 35% hydrogen enriched methane fuel without flashback

happening. So a simple modification was made; the straight center-body in configuration A was replaced with a conical shape center-body as in configuration B. The induced converging fuel/air mixture flow right before dump plane dramatically improved performance for burning hydrogen enriched flames. In addition, since fuel and air are mixed before they are induced into the burner, the fuel-air mixture before burning at the dump plane can be expected be well premixed. This burner can be operated at pure hydrogen without any flashback happening.
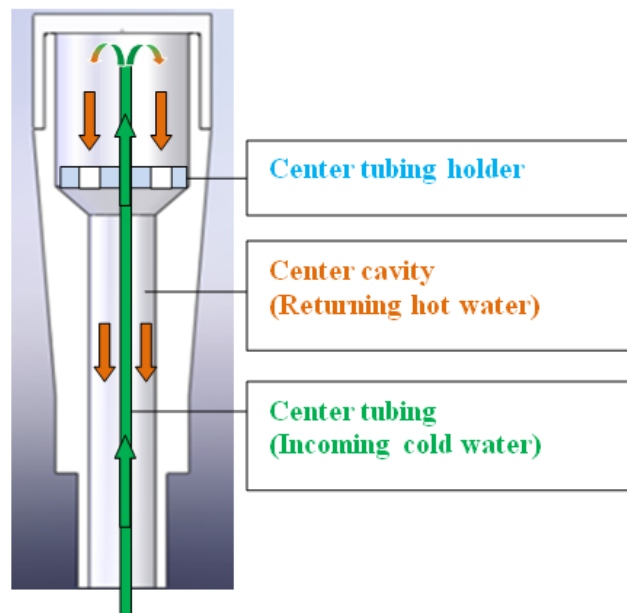
Figure 3-4 Schematic diagram of water cooling

In addition, the center-body with empty center can be used as either a center jet flow or water cooling. As to the water cooling system, Figure 3-4 shows the corresponding schematic diagram. The small center tubing of I.D. of 1.6 mm (1/16 inch) delivers the incoming cool water. The water spays out at the end of the small center tubing and impinges on the solid cap. Then the water turns around on the inner surface of

20

the solid cap and flows back via the center-body. This same scheme can also apply for pre-heating the center-body.

The fuel and air delivery system is schematically shown in Figure 3-5. The fuel is supplied from pressurized bottles of methane and hydrogen. The flow rates of air and fuel are all monitored by corresponding mass flow meters, and the ones for fuel are actually mass controllers. So the fuel flow rate can be set by LABVIEW DAQ board.
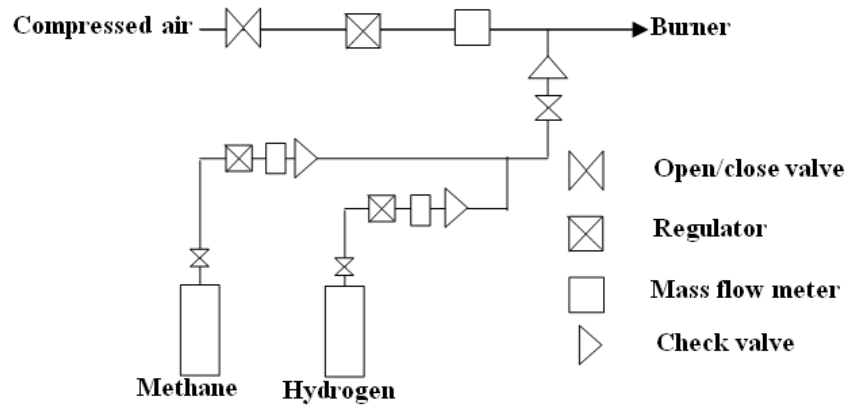
Figure 3-5 Schematic view of the fuel and air flow control/monitoring system

The global equivalence ratio for hydrogen-enriched methane mixture, it is calculated based on the ratio of stoichiometric air to fuel ratio (AFR) to actual AFR with blended methane and hydrogen. The hydrogen blend is expressed in the results as a volume percentage.

3.3   Instrumentation

3.3.1   Flow Field Measurement-PIV

Particle image velocimetry, PIV, is an optical and nonintrusive laser based method used to measure velocities and related properties in fluids, such as vortices, strain

and the like. It consists of Laser source, Laser sheet forming lenses, timing unit and camera(s). And the fluid should be homogenously seeded with small tracking particles, which, for the purposes of PIV, are generally assumed to faithfully follow the flow dynamics and normally are additionally added into the measuring flow field. These particles are then illuminated by Laser sheet in a plane of the flow at least twice within a short time interval, so called time delay or pulse separation, which is determined by the maximum flow velocity. And the light scattered by the particles is recorded either on a single frame (auto-correlation) or on a sequence of frames (cross-correlation). Finally the displacement of the particle images between the light pulses is determined through evaluation of the PIV recordings. It is the motion of these very seeding particles that is utilized to obtain velocity information. In order to be able to handle the great amount of data collected by utilizing the PIV technique, sophisticated post-processing of data is often required.

In this study, a commercial PIV system (IDT Inc) using two Sharp Vision 1400DE cameras is employed. These CCD cameras have a resolution of 1360(H) $\times$1024(V) pixels with pixel size of 4.65 $\times$4.65 μm^2. Both cameras are equipped with Nikon lens of 50mm focal length. To illuminate the flow field of interest, laser-light from a twin head dual cavity Nd:YAG laser is combined and frequency doubled in order to generate two green light pulses at 532 nm, with pulse energy of 120 mJ and pulse duration of 5 ns. The laser beam, with diameter of 5 mm, goes through the optics of a cylindrical and a spherical lens and forms a light sheet in the measurement field. During the measurement, the PIV system is operated at a frame rate of 10 Hz. The time between two laser pulses is between 20 and 40 µs, depending on the flow velocity; this time

increment is used to optimize the accuracy of data processing. The field of view (FOV) is approximately 85mm×60mm. The seeding particles are small enough to ensure good tracking of the fluid motion (Stokes number < 1) and big enough to scatter light for image capturing (also be resistant to high temperature). Here TiO_2 particles with nominal diameter of $3\,\mu m$ are introduced upstream of the swirler in order to distribute them homogenously and to follow the flow oscillation with a frequency up to 1 kHz [84]. Although the PIV measurements made do not resolve the 1 KHz time scale, it is important for the seeding particles to correctly represent the instantaneous fluctuations of the flow-field.

Figure 3-6 Two cameras configuration of 2D-PIV measurement for a large measurement domain

IDT pro-VISION software was used to analyze the PIV data, and the adaptive interrogation mode was used since it provides a second-order accurate mesh free

algorithm [85]. A 60×50 mesh has been used to get 3000 vectors per frame with 32×32 correlation windows. It yields a spatial resolution of approximately 1.1×1.0 mm. Using a portion of the light sheet with approximately 2.0 mm thickness and a short inter-frame time helps to freeze the out-of-plane motion of seed particles. Sets of 500 image pairs are usually recorded for each data set and statistically processed for the mean and RMS values. Considering a typical value in the measurement error of 0.1 pixel units [86], which combines bias and RMS errors, and a typical displacement of 8 pixel units in this experimental PIV measurement, this error is 1.25% as a percentage of the mean local velocity.
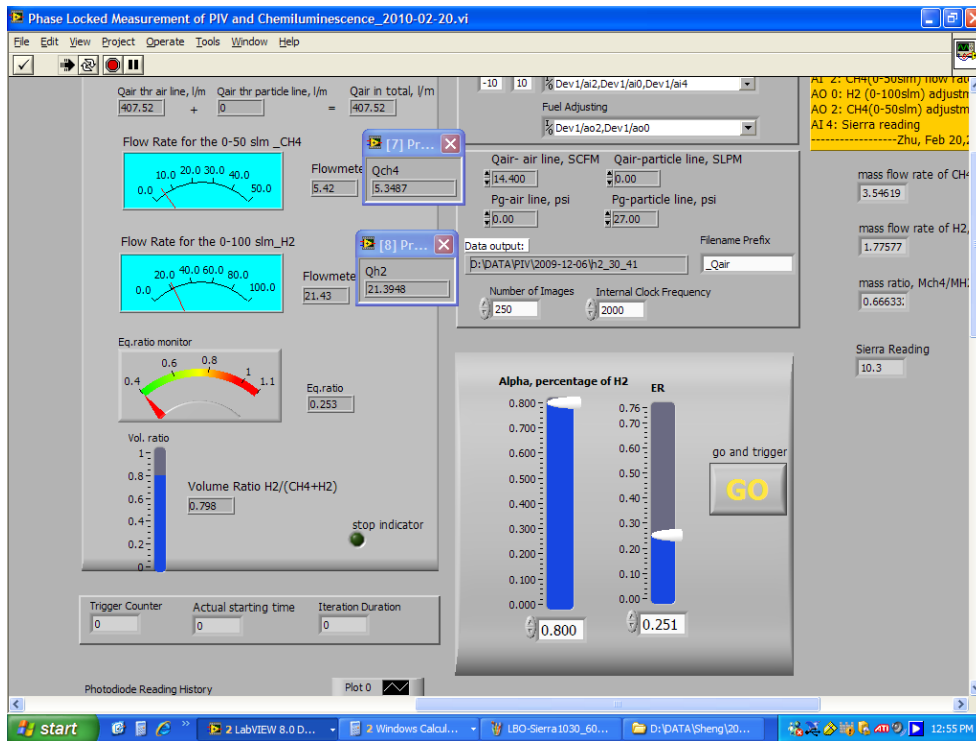
Figure 3-7 A screenshot of a LabVIEW control panel for simultaneous measurements of 3D-PIV and CH/OH chemiluminescence

Additionally, to enlarge measurement domain, two PIV cameras are aligned vertically to take velocity measurement individually with a certain common domain for data post-processing, as shown in Figure 3-6.

3.3.2 Data Acquisition with LabVIEW

LabVIEW, a graphical programming language by National Instruments, is used for the data acquisition here. A program code written in LabVIEW processed the data collected on the A/D data acquisition board (PCI-6229) and sent out the control signals to corresponding devices, and displayed and stored all the relevant information. Sheathed BNC cables were also used to minimize cable noise. PCI-6229 has four 16-bit analog outputs (833 kS/s), 32-16bit analog inputs (250 kS/s), 48 digital I/O, 32-bit counters, and digital triggering Correlated DIO (32 clocked lines, 1 MHz). A snapshot of a LabVIEW control panel for simultaneous measurements of 3D-PIV and CH/OH chemiluminescence is shown in Figure 3-7.

3.3.3 CH* Chemiluminescence Measurement with ICCD Camera

For chemiluminescence measurement, an intensified CCD camera (Princton Instruments PI-MAX 2) equipped with an F-mount Nikkor f: 78/3.8 UV sensitive lens is utilized to resolve heat release characteristics through corresponding chemiluminescence imaging technique. The CCD array of the camera has 1024x1024 resolutions with 12.8x12.8 μm^2 pixel size.

For CH* chemiluminescence measurement, a filter mounted on the camera lens is used to transmit the light at λ=430 nm which corresponds to the $B^2\Sigma$--$X^2\Pi$ (0, 0)

emission band of the CH* radical [87], and to attenuate all other wavelength contributions. Gain was adjusted based on the operating condition and the gate duration for the image acquisition was set to 400 μs.

3.3.4   OH* Chemiluminescence Imaging

A typical configuration of high speed camera and UV intensifier for Chemiluminescence measurement is shown in Figure 3-8, including an UV lens, UV intensifier, and the high speed camera. The achromatic ultraviolet lens (Nikkor, Inc) of 105-mm focal length with f/#4.5 is used to focus the light emitting from the flame into the camera intensifier. The collected radiation of OH* first passes through an interference filter, centered at 308 nm and with a full-width-half-maximum (FWHM) of 10 nm, which corresponds to the primary spectral region for the OH to $A^2\Sigma^+$-$X^2\prod$ electronic transition. The UVi camera intensifier (Invisible Vision Ltd. Model number 1850-10) is used to enhance imaging of weak Chemiluminescence signal. This intensifier is especially designed for high speed cameras and video systems, with ultra high speed shuttering. It is capable of gating low down to 30 ns and light gain up to 400,000 photon counts. Working range covers from UV to NIR (200 nm-85 nm). Then it is followed the Photron SA-3 high speed camera, in between there is a normal lens (Nikkor, Inc) of 50-mm focal length with f/#1.4. The SA-3 camera can be operated at 2000 frame per second with 1024×1024 pixels resolution, and up to 120K fps with reduced resolution. In addition, the availability of external triggering in the intensifier and the high speed camera enables the synchronization with PIV or other measurement systems.
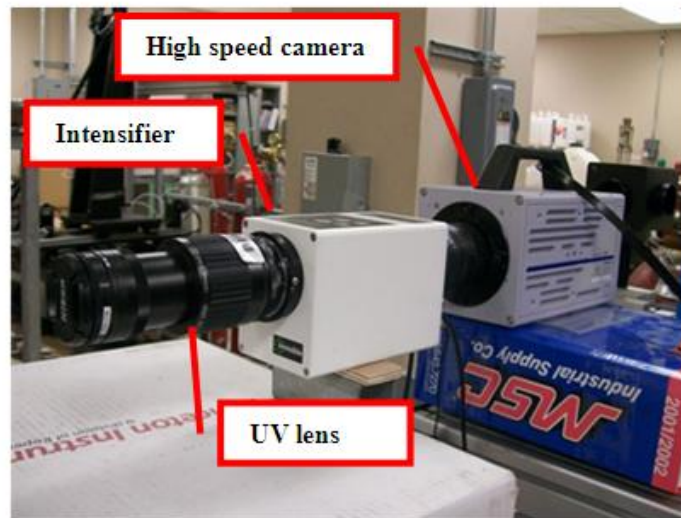
Figure 3-8 Configuration of high speed camera with an UV intensifier.

3.3.5 PLIF System

Planar laser-induced fluorescence (PLIF) is an optical and non-intrusive diagnostic technique widely used for flow visualization and quantitative measurements of velocity, concentration, temperature and pressure. Corresponding calibrations are needed for quantitative measurements [88, 89, 90].

A typical PLIF setup consists of a light source (usually a laser), a set of lenses to form light sheet, fluorescent medium (such as flames), collection optics, a detector (usually intensified CCD camera), and a synchronizer. The light sheet generated by the lens set from light source illuminates the medium, which then fluoresces. The fluorescent signal is filtered with collection optics and captured by the detector. And during this capturing, the synchronizer is used to synchronize light source and detector by sending a series of triggering signal to them. The common used lasers as light sources are pulsed lasers, such as Nd:YAG laser, dye lasers and exciter lasers, which not only provide a

27

higher peak power, but also have a very short pulse time valuable for good temporal resolution.
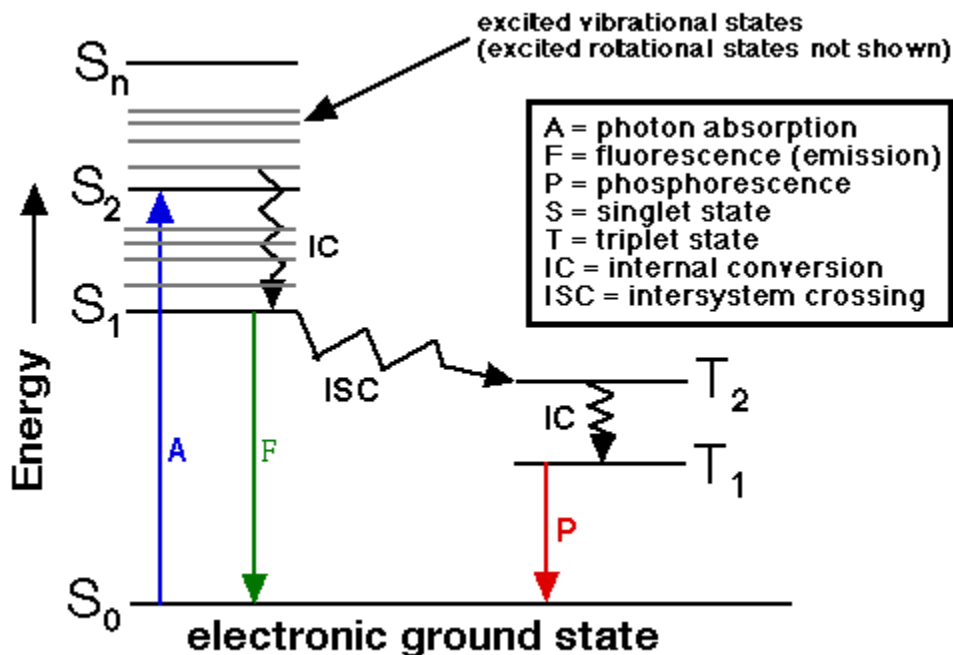
Figure 3-9 Jablonski Diagram [91]

The fluorescence is related to the various properties of the medium so that the flow properties can be evaluated. It results from a transition process that occurs when certain molecules so called fluorophores, fluorochromes, or fluorescent dyes absorb light. Then their energy level is raised from the ground/lower energy state to an electronically excited state, which is energetically unstable with respect to the former. As they decay from this excited state, the excitation energy is released by emitting fluorescent light, and these molecules return to the ground state. These de-excitation pathways, featured with very rapid rates, usually are classified into three broad categories: A) radiative transition processes, in which electromagnetic radiation occurs as the exited molecule returns to

28

lower energy states; B) non-radiative transition processes, in which the populations in the initially excited states are transferred into others without any accompanying emission; C) absorption processes, in which the molecule absorbs another photon and is excited to even higher molecular states. The process responsible for fluorescence is illustrated by a simple electronic state diagram, termed of Jablonski Diagram, as shown in Figure 3-9 [91, 92].

The most common combustion species detected by PLIF are OH, CH and NO. CH and OH are the primary species identifying the reaction zones and burnt gas zone, respectively, and NO is used to monitor pollutant byproducts formed in a flame. For detecting the instantaneous reaction zones, then CH-PLIF seems a better choice, but OH-PLIF is more frequently used in combustion application because the corresponding exciting laser wavelength is more accessible. And it has been shown that the maximum OH concentration within the flame front is a good measure of the strength of chemical activity (or burning rate) in the flame [93].

For OH measurement, [94] studied the ultraviolet bands of OH in detail and gave the fundamental data required for evaluation of various transitions. The most common excitation bands correspond to the Q rotational branch and the R rotational branch in the (1, 0) vibrational transition corresponding to approximately 283.7 nm and 281.2 nm respectively in the temperature range of 1000 to 1500k. The fluorescence is usually collected broadband from (1, 1) band center on 315 nm using 10 nm band pass filter.

The OH-PLIF imaging system can be divided into three subsystems: the excitation, detection and processing systems. The excitation system comprises of a dye laser pumped by an Nd: YAG laser. The third harmonic generator of the Nd: YAG laser

generates 355 nm laser beam to pump the dye laser with pulse energy of about 250 mJ at a frequency of 10 Hz. The Courmrin 153 dye solution is used to produce light at 566 nm. Then through the frequency doubled unit BBO-I crystal, the frequency of the laser beam is doubled at about 283 nm wavelength and with about 10 mJ pulse energy. The detection system here is the same ICCD camera used for chemiluminescence measurement. Additionally, the fluorescence image acquisition is performed by WinView program.

CHAPTER 4 : DATA POST PROCESSING

4.1   Flame Front Detection and Progress Variable \<c\> Map
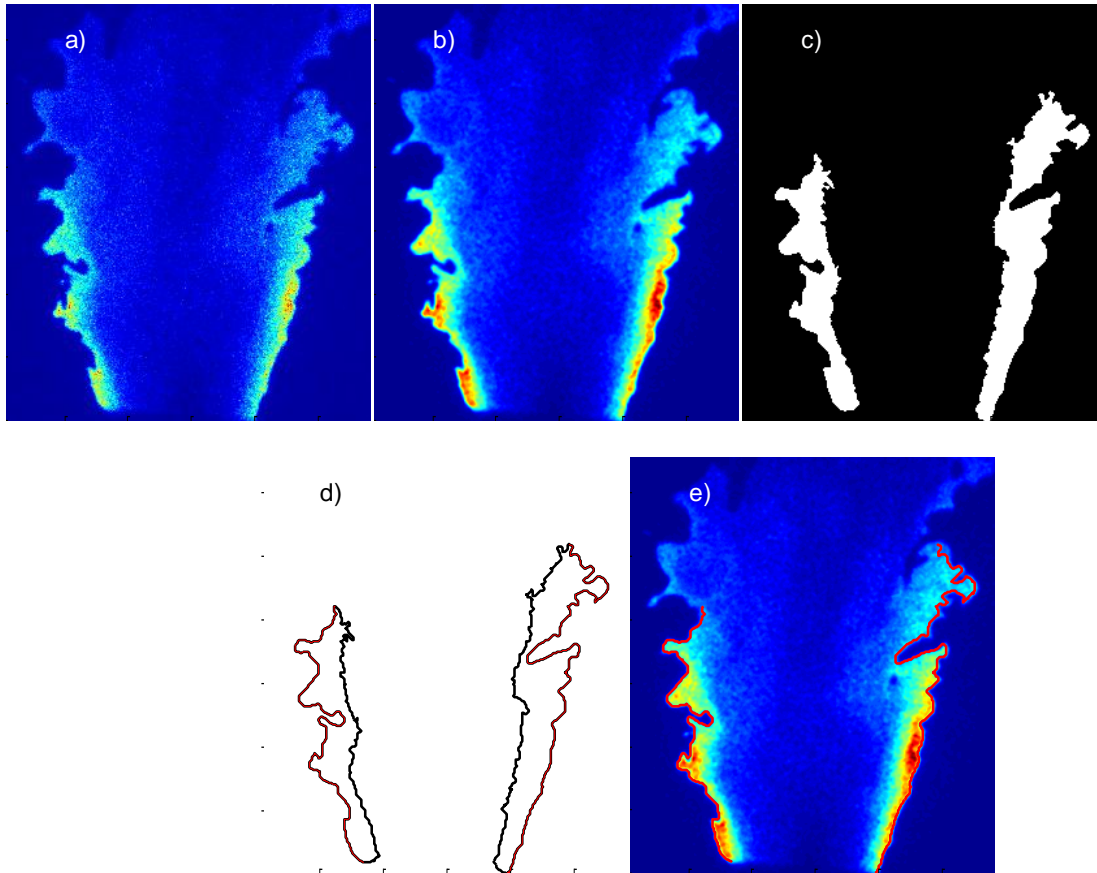
Figure 4-1 Identification procedure of flame fronts from OH-PLIF image, a) an instantaneous raw image, b) corrected and filtered image, c) binary image, d) detected edges (black) and flame fronts (red), and e) fluorescence image superimposed with flame fronts.

The flame front in the premixed flame, the very thin reaction zone with most of chemical reactions taking place, is characterized by high local heat release rate associated with those reactions and separates burnt and unburnt gases due to thermal expansion. Information associated with the flame front is very important as it involves most of energy released by combustion, flame interaction with flow which in turn affects the flame front behavior, flame structure, burning velocity and etc. The common flame

markers used experimentally to identify the flame front are OH* and CH*, since the maximum OH* intensity is near the maximum flame temperature [55] and CH* profile presents in a thin, high-temperature region [56]. Typically, flame front detection is obtained by using planar laser induced fluorescence (PLIF) of the CH or OH radicals [95, 96]. It is also known that Mie scattering images of seeding particles in the combustion flow field show particle-concentration jump across the reaction zone in the flame front due to gas thermal expansion. This flame-front detection technique using Mie-scattering has been used by several investigators [97, 98] to identify the flame front and the associated flame speed.

Figure 4-2 Snapshot of flame

In this study, OH-PLIF images were topologically processed to extract the flame front, and then further analyzed to obtain the flame curvature and surface density.

For the flame front detection from OH-PLIF images as shown in Figure 4-1, each raw image is first corrected with background image and laser intensity distribution. Image filtering is performed by convoluting 5x5 pixel median filter and Gaussian filter over the entire image to further reduce noise. A threshold of 50% of maximum

32

fluorescence intensity is chosen to convert the intensity scale image into binary image as in Figure 4-1c), with ones for completely burnt regions and zeros for un-burned fresh mixtures. From this binary image, the boundary of ones, that is, the interface between hot products and fresh mixture, can be tracked. since the flame is stabilized in the inner shear layer as shown in Figure 4-2, the very portion of binary image boundaries that located in the outer is the true flame fronts, as shown red lines in Figure 4-1d). Figure 4-1e) shows the corrected and filtered fluorescence image superimposed with detected flame fronts. It evidently shows that the flame fronts are successfully detected.
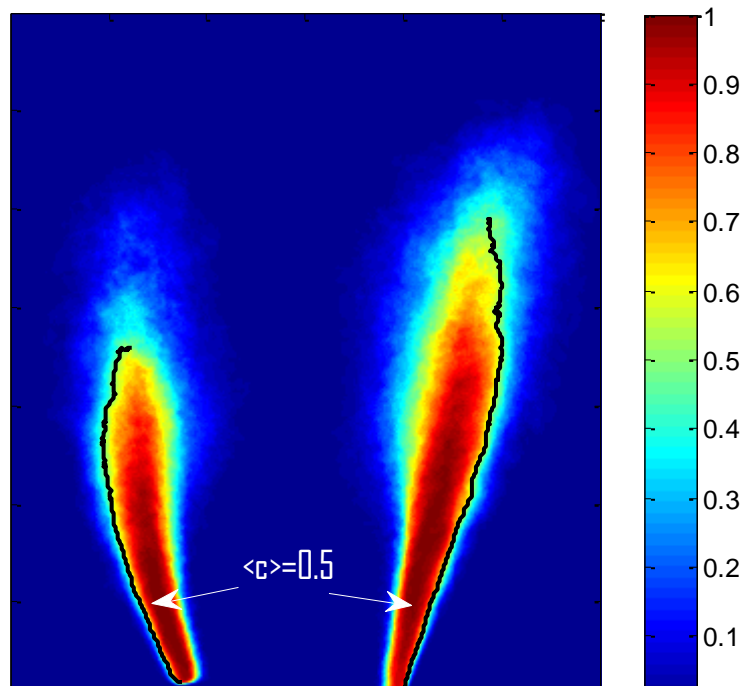
Figure 4-3 Progress variable <c> map superimposed with corrected <c>=0.5 lines.

For the progress variable <c> map, which represents probability of the flame front being at a given location, it can be computed from averaging the whole sequence of binary images converted from fluorescence images, as shown in Figure 4-3. Again, for

extracting a line with a specific <c> value, attention should be paid to the fact that only outer portion of lines are effective, as the black lines for <c>=0.5 shown Figure 4-3.

4.2 Flame Front Curvature

From the instantaneous flame front topological images from OH-PLIF measurement, the local flame front curvature can be calculated to investigate the flame structure properties and the length scales along the flame surface. Here the probability density function (PDF) of the curvature, k, is determined for a more comprehensive representation of the statistics. To evaluate curvature, the procedure of Sioka et al. [99] is followed. As described in previous section, the binary image of burnt and unburnt regions is first generated from each instantaneous fluorescence images (similar to the evaluation process of flame front detection). The positions of flame fronts are then extracted from each such binary image and their Cartesian co-ordinates (x, y) stored, and parameterized as a planar curve in terms of a path length variable s. By this process, the flame contour is characterized via two functions x(s) and y(s), and a cubic spline interpolation is applied. Finally the curvature k can be obtained as an inverse of the curvature radius r_m by:

$$k = \frac{1}{r_m} = \frac{\dot{x}\ddot{y} - \dot{y}\ddot{x}}{(\dot{x}^2 + \dot{y}^2)^{3/2}} \tag{4-1}$$

where k and r_m are defined positive if the flame element is convex toward the reactants. Based on the whole data set of k values determined from hundreds of fluorescence images, the PDF distribution of the flame curvature can be determined.

4.3   Flame Surface Density

Two-dimensional measurement of flame surface density Σ can be estimated by using the determined flame front instantaneous images. Here the topographic method described in Shepherd et al. [100] is adopted where the progress variable space <c> is subdivided into 10 intervals between 0 and 1, and then the corresponding flame zone area, A(<c>), is determined directly from the <c> map by adding up the area of each pixel corresponding to <c> value. Since the length of the flame is a function of <c>, L(<c>), it can be calculated by smoothing the flame edge and then dividing it into segments of equal length (0.1 mm). From the <c> map, each segment is assigned a <c> value and the flame lengths accumulated to give a total flame length, L(<c>), for each data set. Then the flame surface density, Σ(<c>), can be calculated readily from those date sets:

$$\Sigma(<c>) = \frac{L(<c>)}{A(<c>)} \tag{4-2}$$

4.4   Flame Strain Rate

The instantaneous flame front locations extracted from OH-PLIF images are used in conjunction with corresponding PIV data to determine the stretch rate information along the flame fronts. Two-dimensional flame stretch rate can be calculated using [101],

$$K = K_s + K_c \tag{4-3}$$

$$K_s = -n_x \times n_y \times \left(\frac{\partial u}{\partial y} + \frac{\partial v}{\partial x}\right) + (1 - n_x^2) \times \frac{\partial u}{\partial x} + (1 - n_y^2) \times \frac{\partial v}{\partial y} \tag{4-4}$$

$$K_c = S_L / R_c \tag{4-5}$$

where

K_s is the tangential strain rate;

K_c is flame curvature induced flame stretch rate;

S_L is the laminar burning velocity;

R_c is the radius of flame curvature;

n is the flame surface normal vector, and n_x and n_y are the x and y components of n;

u and v are the velocity components in the x and y directions.

In turbulence flame, there is a distribution of flame stretch rate, and the strain rate contribution is dormant. Bradley et al [102] suggests that for values of Karlovitz number K_a greater than 0.1 and of turbulent Reynolds number R_t greater than 100, the PDF of stretch rate is similar to that of strain rate. So here, the flame curvature effect is no considered and only hydrodynamic stretch rate Ks is computed via PIV data and detected flame fronts from OH-PLIF images.

4.5   Abel Inversion

To consider a radiation source is cylindrically symmetrical and it is observed in the side-on direction, the line-of-sight emission can be described by the Abel equation, as shown in Figure 4-2,

$$I(x) = \int_{-\infty}^{+\infty} f(r)dy \tag{4-6}$$

where r is the radial location, f(r) is the original radial distribution. If f(r) is negligible when r is greater than R, then the Abel equation can be re-written as,

$$I(x) = 2 \int_{r}^{R} \frac{f(r)rdr}{(r^2 - x^2)^{1/2}} \tag{4-7}$$

To obtain the original radial distribution function f(x) for the lateral intensities I(x), we have Abel inversion,

$$f(r) = -\frac{1}{\pi} \int_r^R \frac{(dI/dx)dx}{(x^2 - r^2)^{1/2}} \tag{4-8}$$
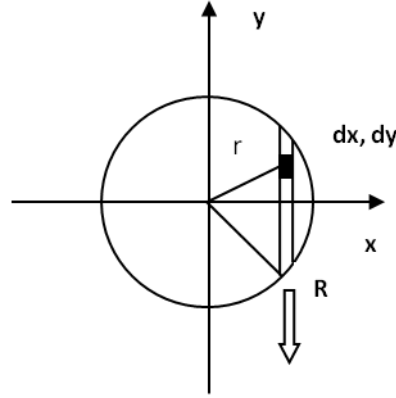
Figure 4-4 Schematic diagram of the line of sight

It shows that the integrand diverges at r=x, which make it difficult to apply directly in practice. Here the numerical algorithm developed by Nestor and Olsen [103], so called Nestor-Olsen method, which transforms the Abel inversion equation into a summation to allow processing of discrete sets of data. This method is widely employed due to its easy computation with reasonable accuracy [104, 105]. The relationship between the emission f(r) and the integrated I(x) is given by,

$$f(r_j) = -\frac{2}{\pi \Delta x} \sum_{i=j}^N I(x_i) B_{j,i} \tag{4-9}$$

where the x-axis is divided into zones of equal width Δx, with the ith zone being $x_i \leq x < x_{i+1}, x_i = i\Delta x$, and the coefficients are as follows,

$$B_{j,i} = A_{j,i-1} - A_{j,i}, for\ i \geq j + 1$$

$$B_{j,i} = -A_{j,i}, for\ i = j$$

$$A_{j,i} = \frac{((i+1)^2 - j^2)^{\frac{1}{2}} - (i^2 - j^2)^{\frac{1}{2}}}{2i+1} \tag{4-10}$$

For the entire 2D image of side-on observation of the radiation, this Abel inversion can be applied onto each row of the image in order to obtain the 2D distribution of the radial emission.

4.6   Proper Orthogonal Decomposition

Proper orthogonal decomposition (POD) is a statistical method to decompose a series of measurements into an orthogonal basis and corresponding time constants if the data acquisition is time-resolved. The orthogonal basis consists of a set of eigenmodes, or POD modes, representing distinct coherent flow structures arranged in descending order of their contribution to the overall resolved kinetic energy. Therefore, if the flow dynamics is dominated by a few large and energetic flow structures, then they will be captured in the first modes. The time constants for each mode can be obtained by projecting the original data onto the corresponding POD mode and yield all of the temporal information. In present study, the POD was calculated by using snapshot method of POD [106,107,108] for flame images captured by a high speed camera, to further explore the flame front dynamics responsible for the LBO behavior. In following, the procedure of snapshot method of POD based on flame images will be briefly introduced. And the application onto 2D or 3D velocity field can be easily deduced.

Assume that there are N flame images, and each image is R×C matrix and in turn has R×C data points. First arrange the fluctuating part of image intensity for the N snapshots as:

$$X = [x^1 \, x^2 \, ... \, x^N] = \begin{bmatrix} x_1^1 & x_1^2 & \cdots & x_1^N \\ \vdots & \vdots & \vdots & \vdots \\ x_{RC}^1 & x_{RC}^2 & \cdots & x_{RC}^N \end{bmatrix} \tag{4-11}$$

Then we have auto-covariance N×N matrix $\mathbf{C}$:

$$C = U^T U \tag{4-12}$$

Solve this eigenvalue problem:

$$CA^i = \lambda^i A^i \tag{4-13}$$

Arrange the solutions by eigenvalue in a descending order as:

$$\lambda^1 > \lambda^2 > ... > \lambda^N = 0 \tag{4-14}$$

Then the POD modes can be written as:

$$\boldsymbol{\phi}^i = \frac{\sum_{n=1}^{N} A_n^i \boldsymbol{x}^n}{\left\| \sum_{n=1}^{N} A_n^i \boldsymbol{x}^n \right\|} \tag{4-15}$$

Where i=1, 2,…, N.

For the mode coefficients or time constants, they then can be calculated by projecting X onto POD modes. For example, in the nth instant snapshot, the coefficient for i^{th} mode, a_i, can be calculated by:

$$a_i = \boldsymbol{\phi}^i \cdot \boldsymbol{x}^n \tag{4-16}$$

Similarly, the complete coefficient set in this instant, **a**^{n}, can be written as:

$$\boldsymbol{a}^n = [\boldsymbol{\phi}^1 \ \boldsymbol{\phi}^2 \ ... \ \boldsymbol{\phi}^N]^T \boldsymbol{x}^n \tag{4-17}$$

For re-construction, an instant n^{th} snapshot (fluctuating part) can be built as:

$$x^n = \sum_{i=1}^{N} a_i^n \boldsymbol{\phi}^i = [\boldsymbol{\phi}^1 \ \boldsymbol{\phi}^2 \ ... \ \boldsymbol{\phi}^N] \, \boldsymbol{a}^n \tag{4-18}$$

CHAPTER 5 : FLOW FIELD AND REACTON ZONE CHARACTERISTICS

5.1   Introduction

In this chapter, experimental investigation in the flow field, the reaction zone, and the flame structure properties has been performed as flame approaches the LBO limit. 2D-PIV, non-intrusive laser-based diagnostic technique for velocity measurements, was used to capture flow field information, and a COMS high speed camera equipped with an intensifier was employed for OH* chemiluminescence imaging to obtain the information regarding the reaction zone and its behavior. The schematic view of this experiment setup is shown in Figure 5-1. The experiment data is then analyzed to generate some key mechanistic conclusions about LBO in methane and hydrogen-enriched flames.
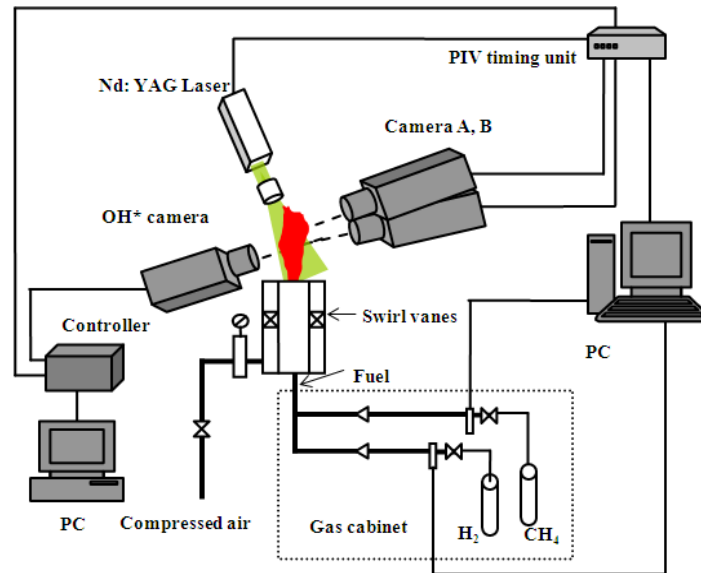
Figure 5-1 Schematic view of experimental setup

The test matrix, in terms of equivalence ratio, is listed in Table 5-1, with all data taken at a Reynolds number of 17,670 based on the bulk velocity. For hydrogen-enriched

methane mixture, the global equivalence ratio is calculated based on the ratio of stoichiometric air to fuel ratio (AFR) to actual AFR with blended methane and hydrogen. The hydrogen blend is expressed in the results as a volume percentage.

Table 5-1 Experimental test matrix (hydrogen percentage based on volume basis)

Fuels	Φ_{LBO}	Φ_1	Φ_2	Φ_3	Φ_4
CH_4	0.675	0.744	0.694	0.689	0.684
$40\% H_2$	0.450	0.669	0.474	0.464	0.457
$60\% H_2$	0.345	0.654	0.447	0.359	0.354
$80\% H_2$	0.255	0.432	0.340	0.268	0.264
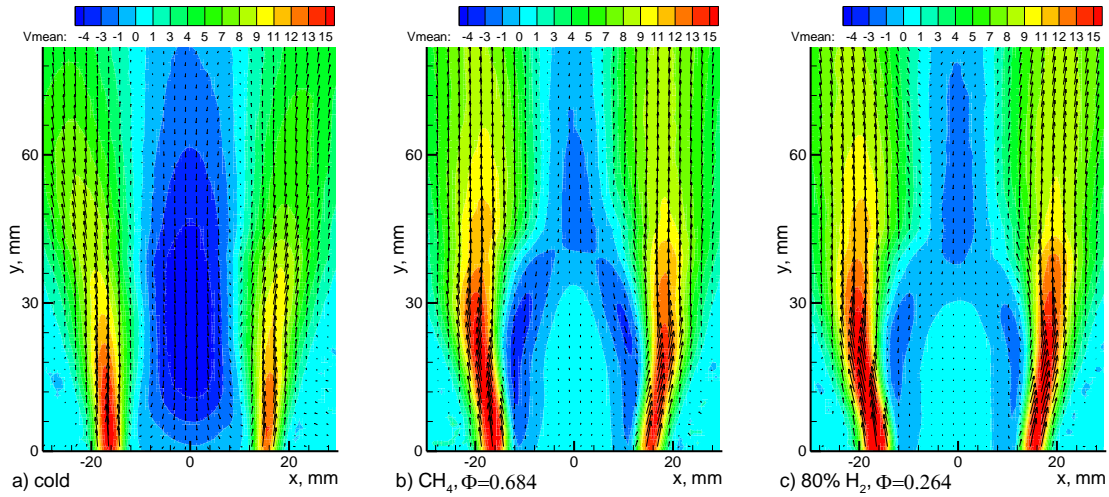
Figure 5-2 Axial velocity field for (a) non-reacting flow, (b) CH$_4$ flame at Φ=0.684 , and (c) 80% Hydrogen-enriched flame at Φ=0.264

In presenting the results, we will discuss the flow field behavior first and then examine the high speed chemiluminescence images to correlate the heat release behavior with the flow dynamics. The methane-only results will be contrasted with the data

41

representing different hydrogen contents. We will conclude with an assessment of the LBO mechanisms for both the methane-only and the hydrogen-enriched flames.

5.2 Flow Field
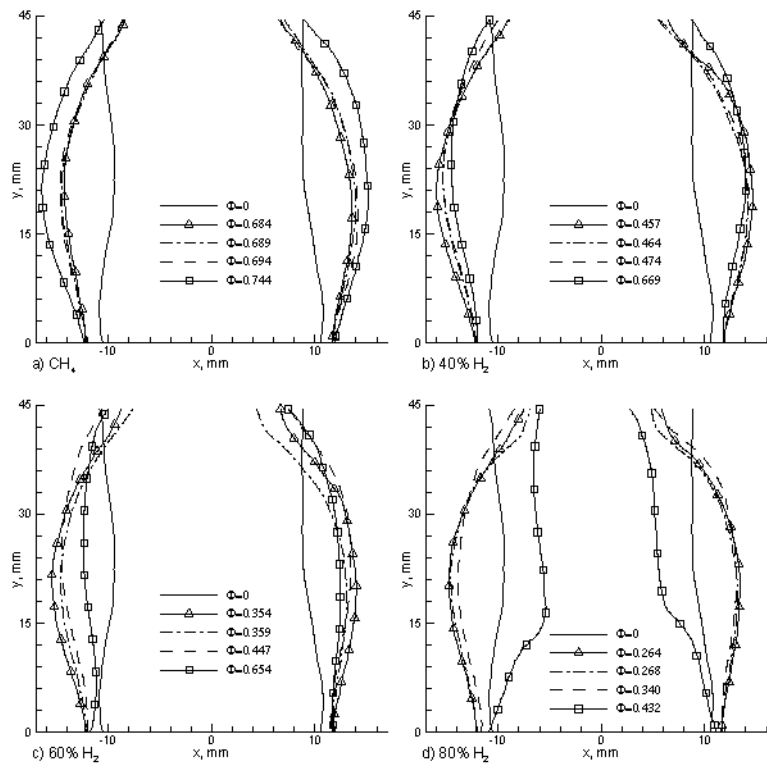
Figure 5-3 Boundaries of IRZ for (a) CH$_4$ flames, (b) 40% H$_2$ flames, (c) 60% H$_2$ flames, and (d) 80% H$_2$ flames

Figure 5-2 shows the contours of mean axial velocity for the non-reacting flow and for the reacting cases of methane-only and 80% hydrogen-enriched flames, superimposed with corresponding velocity vectors. In the non-reacting flow, represented only by the swirling air flow, it is clearly seen that a pair of nearly axisymmetric recirculation zones are established above the dump plane, centered at nearly y/D=1.4 (y≈50 mm), along with two weak corner recirculation zones. In the reacting flow with methane or 80% hydrogen-enriched flames, a similar flow pattern is found as the ring-

pair shape structure of internal recirculation zone (IRZ) in the non-reacting flow, but positioned at nearly y/D=0.86 (y≈30 mm). It is noted that all reacting cases in this study have similar flow patterns.

Figure 5-3 shows the boundaries of the IRZ for cases of the methane-only flame, and the hydrogen-blended flames with 40%, 60%, and 80% hydrogen respectively, along with in the boundaries for the non-reacting flow. In all the reacting cases, there was no flashback observed, and so changes in the observed flow patterns are not related to any flashback mechanism. The IRZ boundaries are obtained directly from the PIV measurements. The width of IRZ in the non-reacting flow initially increased immediately after the dump plane, and then decreased slightly, followed by an increase along the axial direction. The IRZ closes further downstream (beyond the axial region shown). This initial non-monotonic behavior is believed to be due to the effects of the center-body and the swirling flow. Very close to the dump plane, the recirculation mainly results from center-body effect. The region above the center-body creates a negative pressure gradient along the axis, and in turn, leads to the back-flow. Farther from the dump plane, the negative pressure gradient caused by the center-body reduces and the width of recirculation is decreased. Further downstream, the effect of the swirl generated upstream by a swirler dominates. The decay of the tangential velocity of the swirling flow induces another negative pressure gradient in the axial direction and increases the size of the recirculation zones. For all the reacting cases the width of the IRZ initially expands and then decays due to reduction of the tangential velocity. This behavior is influenced by the increased vorticity resulting from combustion-induced vorticity generation. Along the axial direction, the recovery of adverse pressure gradient caused by center-body was

43

compensated for much earlier by the negative pressure gradient resulting from swirling effect, and the initial decay in the IRZ was not observed.
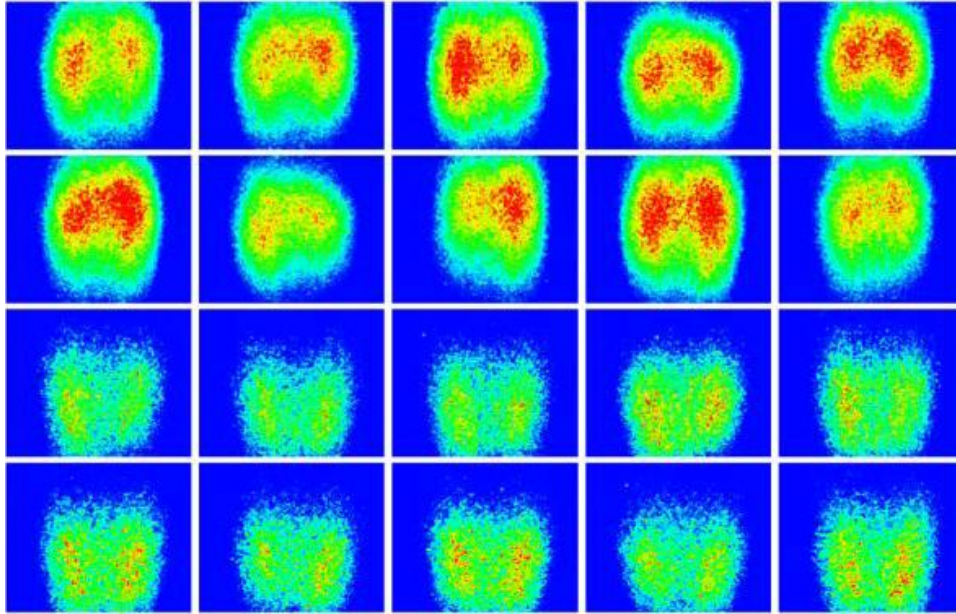
Figure 5-4 Instantaneous OH* distributions for CH₄ flame at Φ=0.684 (top two rows) and 80% H₂ flame at Φ=0.264 (bottom two rows). Time increases from left to right with step increments of 0.2s

In addition, as shown in Figure 5-3, in the case of hydrogen-enriched flames, the width of IRZ increases as the equivalence ratio Φ is reduced. This behavior is mainly due to lower heat release leading to reduced axial velocities and increased local swirl level when Φ decreases. The increased local-swirl leads to a broadened width of the IRZ with reduced Φ. However the width of IRZ in the methane flame surprisingly decreases as the LBO limit is approached. This behavior is counter to the observation for the hydrogen-enriched flames noted above and points to the existence of different LBO behavior for the two cases. As will be discussed, the OH* measurements indicate that the methane flames are lifted, especially when approaching the LBO limit, while the hydrogen-enriched flames are all attached.
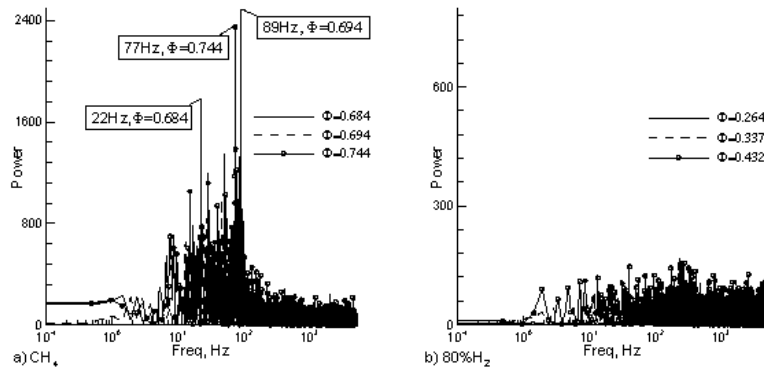
Figure 5-5 Power spectra of OH* signal for (a) CH$_4$ flames, and (b) 80% H$_2$ enriched flames

Figure 5-4 shows the instantaneous OH* distributions at time step increments of 0.2 second for both the methane-only (top two rows) and hydrogen-enriched (bottom two rows), and these point to key differences between the two flames. In the top two rows in Figure 5-4, for methane, the flame near LBO is clearly lifted from the dump plane and the lift-off shows variation in size with time. The OH* distributions show a periodic variation in the intensity distributions. This is characteristic of a precessing vortex core (PVC) that is generally sensitive to external perturbation [109]. For the hydrogen flame in the bottom two rows in Figure 5-4, the OH* distributions are anchored closer to the dump plane and the intensity distributions remain fairly steady implying the absence of a helical PVC. It should be noted that Lewis number for methane is near unity while that for hydrogen is much lower leading to preferential diffusivity of the fuel-mixture toward the flame front for the hydrogen-enriched cases. This mechanism could have a role in the stronger flame attachment for the hydrogen flames. As will be discussed later, the different OH* behaviors for the methane flame and the hydrogen flame near LBO are related to different modes of the instability of vortex breakdown.
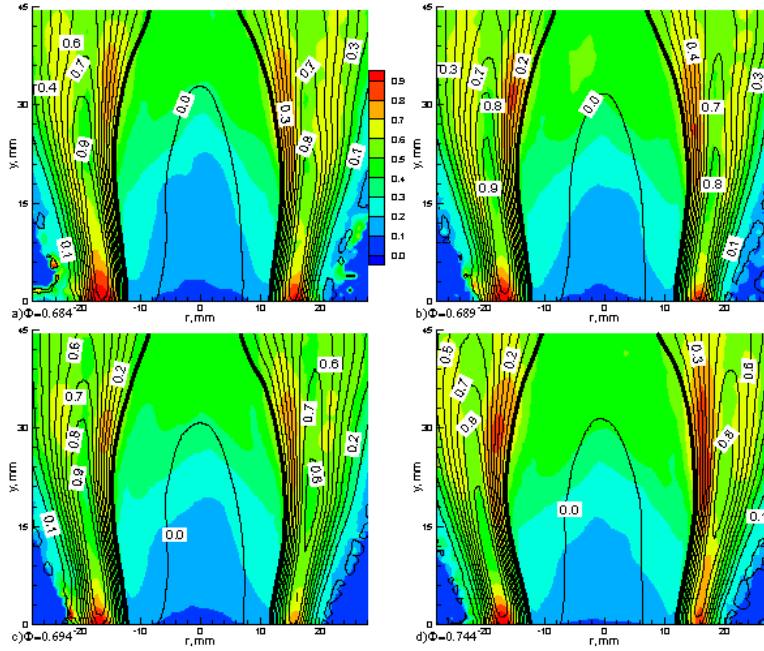
Figure 5-6 Normalized V_rms color contour superimposed with normalized V_mean line contour and thickened IRZ lines for CH₄ flames for a) Φ=0.684, b) Φ=0.689, c) Φ=0.694, and d) Φ=0.774

In order to verify the occurrence of PVC, a high speed measurement of OH* signal was carried out in a region spanning y from 17 mm to 52 mm, and x from -40 mm to 25 mm. Gate time and framing rate were set at 90 μs and 10K fps, respectively. The signal was recorded for 2.1 seconds. A total of six different locations with x steps of 15 mm and y steps of 10 mm were processed, and two different calculation spot sizes of 1x1 mm^2 and 5x5 mm^2 were used to do the spectral analysis. It is found that neither location nor spot size affects the calculated spectral results. Figure 5-5 shows the power spectrum plots of OH* signal frequency in methane flames and 80% hydrogen-enriched flames, obtained at point (-15 mm, 30 mm) and with calculation spot size of 1x1 mm^2. Figure 5-5 shows that all three measured methane flames of equivalence ratios of 0.684, 0.694 and 0.744 have strong spectra, located at 22 Hz, 89 Hz and 77 Hz, respectively. The maximum Strouhal number (based on outer diameter of feed tube and average velocity)

46

obtained from the spectral analysis is of the order of 0.05 which is much smaller than a jet-vortex shedding frequency for which Strouhal numbers in the range of 0.1-0.3 are expected. The periodic unsteadiness for the methane flame is therefore associated with a helical PVC. Clearly as LBO is approached, the PVC frequency decreases and is related to the PVC breakdown preceding LBO.
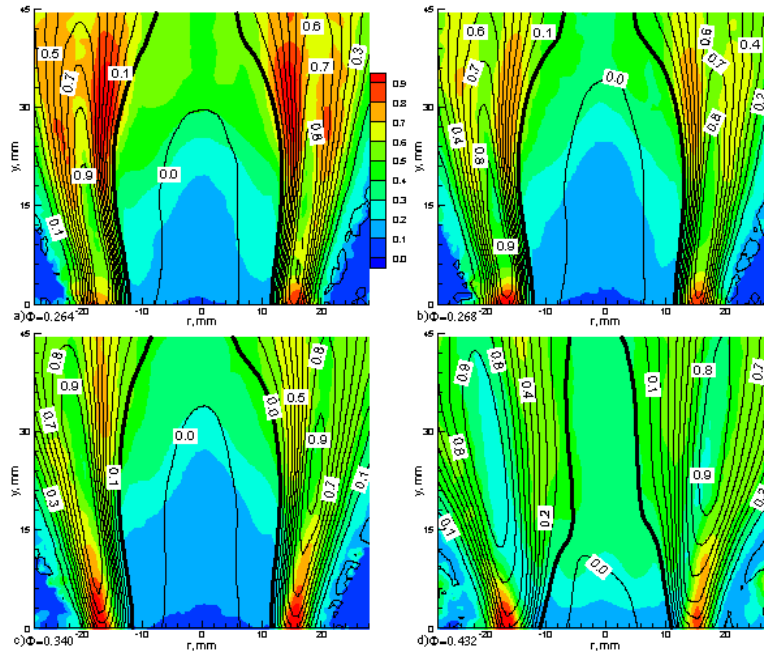
Figure 5-7 Normalized V_{rms} color contour superimposed with normalized V_{mean} line contour and thickened IRZ lines for 80% H_2 flames for a) Φ=0.264, b) Φ=0.268, c) Φ=0.340, and d) Φ=0.432

In Figure 5-5b, for 80% hydrogen-enriched flames, a peak frequency in the spectrum is not obtained. Similarly, there is no evidence of a spectrum peak observed in the 40% or 60% hydrogen-enriched flames. These results indicate broad-band unsteadiness absent of any PVC observed for the methane flame. This indicates that hydrogen addition mitigates the PVC behavior observed for methane flames. Major differences between the hydrogen and methane flames are the higher flame speed and lower Lewis number of hydrogen. The higher flame speeds potentially increases the axial

47

velocities, but as Figure 5-2 shows, the differences in the axial velocity between the two flames are small. Hydrogen has a much lower Lewis number than methane and is characterized by greater flame front instability and wrinkling associated with the preferential diffusivity of the hydrogen. It is speculated that this flame-front instability and wrinkling transitions the PVC into a more stable bubble type of vortex breakdown.
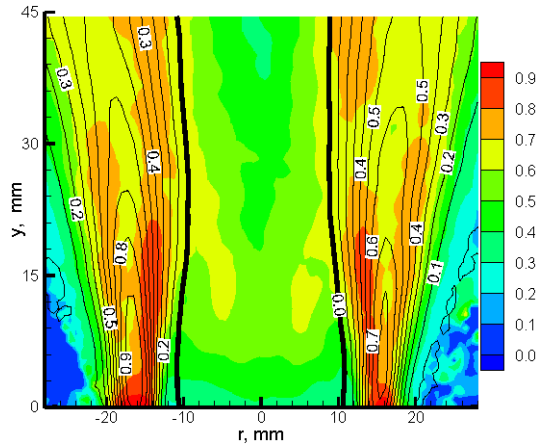
Figure 5-8 Normalized V_{rms} color contour superimposed with normalized V_{mean} line contour and thickened IRZ lines for non-reacting flow

Figure 5-6 and Figure 5-7 show the color contours for axial velocity RMS superimposed with line contours for axial velocities and thick-black lines representing the envelope of IRZ in methane flames, and in the 80% hydrogen-enriched flames, respectively. Both axial velocities and their RMS are normalized with their corresponding maximum values in each case, in order to compare the distributions of the axial velocity fluctuation. It can be observed that the regions with high RMS are all located in the shear layer for both methane and hydrogen-enriched flames, whereas the RMS inside the IRZ is low. The RMS values can be associated with flame stretch and stretch-related extinction. In regions of high RMS, it can be argued that flame extinction can occur due to high stretch and particularly at low Φ where flame speeds and resistance to stretch are

reduced. In Figure 5-6 and Figure 5-7 it can be seen that the RMS values near the flame base are much higher for the methane-only case which may explain the existence of flame quenching and lift off observed earlier for methane-only flame as LBO is approached. The low RMS inside the IRZ is also notable since it plays an important role in the LBO mechanism especially for hydrogen-enriched flames as discussed in the next section.
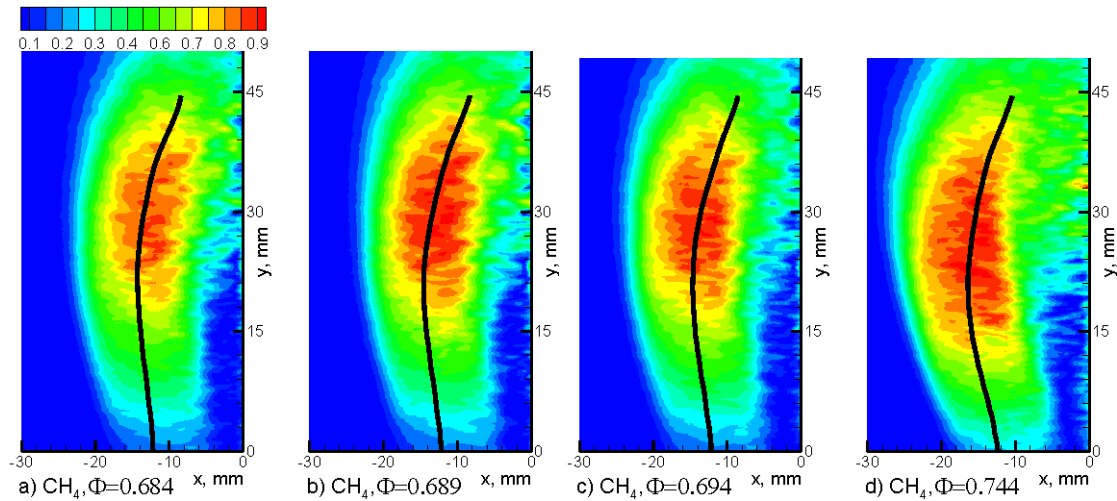
Figure 5-9 Abel inverted radial distributions of averaged OH* superimposed with IRZ lines for methane flames for a) Φ=0.684, b) Φ=0.689, c) Φ=0.694, and d) Φ=0.744

For reference purposes, Figure 5-8 shows the RMS for the non-reacting case which reflects a more uniform distribution of RMS than the reacting cases. Further, the axial velocity RMS decreases downstream in view of decreasing shear and the absence of any combustion-generated turbulence. Considering that the reaction takes place in the inner shear layer that borders the IRZ, as shown in next section (Figure 5-9 and Figure 5-10), there are two paths for flames to advance toward a favorable reaction region of lower turbulence levels-downstream and inward toward the IRZ. Thus, an important

determinant in the LBO is the relative location of the flame front and the region of the high turbulence which, in turn, is linked to the location of the IRZ.
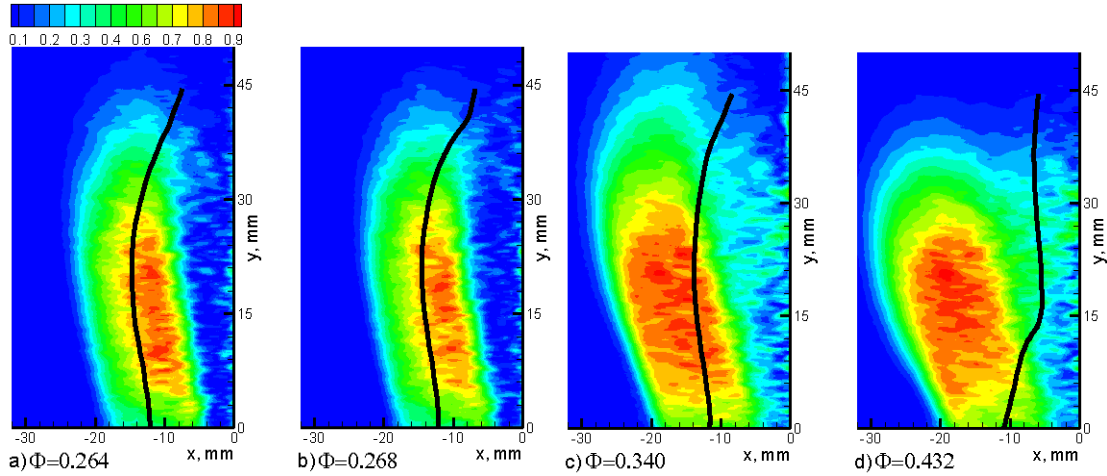
Figure 5-10 Abel inverted radial distributions of averaged OH* superimposed with IRZ lines for 80% hydrogen-enriched flames for a) Φ=0.264, b) Φ=0.268, c) Φ=0.340, and d) Φ=0.432

5.3   Reaction Dynamics

To capture the flame front behavior, OH* images are obtained using a gated ICCD camera. In each flame, a total number of 1250 OH* images were captured. For every data set, each image was first corrected by the background image, then filtered and averaged over the whole sequence of 1250 images to yield the mean line-of-sight OH* image. This averaged global OH* image was then numerically Abel inverted to unfold the radial distribution of OH* signal by using Nestor-Olsen algorithm, which transforms the Abel inversion equation into a summation to allow processing of discrete sets of data and is widely employed due to its easy computation with reasonable accuracy [110, 111, 112]. Figure 5-9 and Figure 5-10 show the Abel inverted radial distributions of the background-corrected OH* intensity averaged over 1250 images, superimposed with the corresponding boundaries of the IRZ represented by the thickened black lines, for pure methane and 80% hydrogen-enriched flames, respectively. The OH* intensities have

50

been normalized by individual intensity maximum and only half of the measurement domain is shown for clarity. Figure 5-9 shows that methane flames are lifted (very low OH* at the base), especially for equivalence ratio 0.684 as mentioned earlier, while Figure 5-10 shows that hydrogen-enriched flames are all attached to the dump plane. In order to compare the relative positions of the flame front and the IRZ, the geometric center of the flame front is calculated from the images in Figure 5-9 and Figure 5-10 and this is plotted in Figure 5-11 along with the boundaries of IRZ for pure methane and 80% hydrogen-enriched fuels. For methane flames in Figure 5-9 and Figure 5-11a, as equivalence ratio decreases from 0.744 to 0.684, the center of reaction zone (OH*) moves radially inward from 16 mm to 12 mm approximately, and downstream from 25 mm to 30 mm, and the IRZ boundary also moves inward. At LBO, the center of the flame sits at the edge of the IRZ and is displaced downstream from the base (lifted). Thus, as shown in Figure 5-9, the flame straddles the IRZ boundary (black line) and the portion of the flame in the shear layer sees high turbulence level (Figure 5-6). Thus at LBO, where the flame speeds are lower, the portion of the flame in the high RMS region is susceptible to extinction and LBO is initiated from here. For the 80% hydrogen-enriched flame shown in Figure 5-10 and Figure 5-11b, when Φ is decreased from 0.432 to 0.264, the center location of reaction zone also moves radially inward from 17 mm to 12 mm, but does not change axially, located around 16 mm at all times. On the other hand, the IRZ boundary moves outward. Therefore, as Φ decreases towards LBO, the reaction in the hydrogen-enriched flames takes place almost completely within the IRZ, where hot combustion product exists and residence times are longer, providing a favorable combustion environment. The flame shape changes from a conical to a more elongated columnar

51

shape as the equivalence ratio is reduced, especially in hydrogen-enriched flames (e.g. in Figure 5-10).
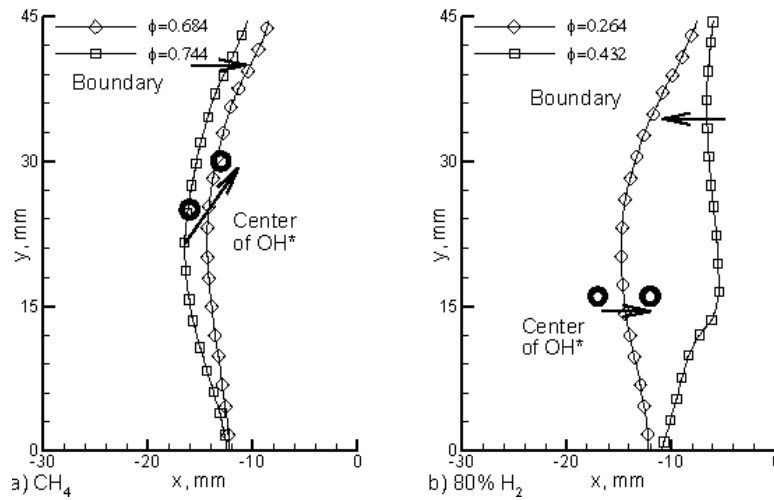
Figure 5-11 Boundaries of IRZ (lines) and centers of reaction zones (circle symbols) for a) CH₄ flames, and b) 80% H₂ flames
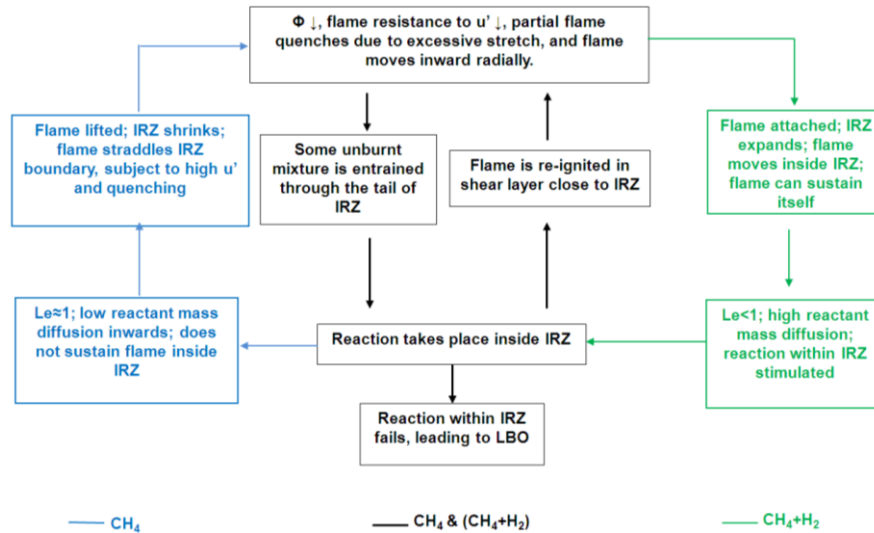
Figure 5-12 Hypothesis diagram for LBO mechanisms of methane and hydrogen-enriched flames.

5.4 LBO Mechanism

Based on the measurement of the reaction zones and the flow field, a LBO mechanism is proposed and described in Figure 5-12. The basic process of LBO is as

follows: as equivalence ratio reduces, the flame resistance to turbulence and stretch is reduced and flame quenching can occur locally in regions of high u'-RMS. The flame moves to the region of lower turbulence level and toward the boundary of IRZ (OH* maxima closer to IRZ observed). Hot combustion products and some unburnt reactant mixture are entrained into the IRZ via the rear of the toroidal vortex; the reactants can easily burn within IRZ due to higher temperatures, longer residence times and lower turbulence. This process sustains high temperatures within the IRZ which, in turn, can re-ignite the locally extinguished flame in the shear layer close to the IRZ. As the equivalence ratio is further reduced, the flame cannot sustain itself in the high turbulence regions, the reactions and high temperatures within the IRZ fail to survive, leading to the final LBO. This generic LBO mechanism is shown by the group of solid-boundary boxes in the middle of Figure 5-12.

For methane flames, with a Lewis number around one, the low fuel mass diffusivity does not promote diffusion of reactants into the IRZ in order to sustain a flame there. Further, as noted earlier, as LBO is approached the flame is lifted and straddles the boundary of the IRZ (Figure 5-9a and Figure 5-11a) resulting in a portion of the flame in the shear layer subject to high turbulence and quenching. The extinction initiated in the shear layer region spreads as equivalence ratio is lowered leading to the final LBO. These mechanisms are shown in the set of boxes on the left in Figure 5-12.

With hydrogen-enriched fuels, the IRZ expands as LBO is approached and the attached flame moves inside the IRZ (Figure 5-10a and Figure 5-11b), where local temperature is relatively high and the flame can sustain itself in this low stretch region. Additionally, with the Lewis number being less than one, the excess hydrogen reactant

53

with high mass diffusivity in the shear layer diffuses more rapidly into the IRZ with a favorable combustion environment. Since the molecular diffusion is more rapid than the thermal diffusion from the IRZ, the burning inside the IRZ more than compensates for the heat loss by local flame quenching leading to an almost constant axial location of the OH* maxima observed in Figure 5-10 and Figure 5-11b. The reactions within the IRZ function as a pilot flame that can sustain itself within the IRZ as the equivalence ratio is further decreased leading to relatively low values of the LBO for hydrogen-enriched flames. The LBO happens after this IRZ flame kernel itself fails to survive. These mechanisms for hydrogen-enriched flames are shown on the right in Figure 5-12.

5.5   Conclusions

An experimental study was performed in a swirl-stabilized combustor with the goal of understanding the flame behavior as the equivalence ratio was decreased toward LBO. Fuels used were pure methane, and methane blended with 40%, 60%, and 80% hydrogen. The following major conclusions are made:

- Both the center-body and swirl levels affect the central inner recirculation zone (IRZ). The near field is dominated by the center-body wake, while the far field is influenced by the swirl.

- As the equivalence ratio approaches the LBO limit, the width of IRZ in the methane-only flame decreases, while that in the hydrogen-enriched flame increases. The PIV and OH* spectral measurements show that the vortex breakdown is in a spiral mode (PVC) in the methane flame while a bubble type vortex breakdown is observed in the hydrogen-enriched flames. It is

believed that the flame front instability associated with the preferential diffusivity of the hydrogen content transitions the PVC into a more stable bubble type of vortex breakdown.

- For methane flames, approaching the LBO limit, the reaction zone is moved inward toward the IRZ, and convectively moved downstream with flame quenching at the base. The decreased width of the IRZ serves as a barrier to burn methane under much leaner conditions, compared to the hydrogen-enriched flames with a larger IRZ. As equivalence ratio is reduced toward LBO, the flame straddles the boundary of the IRZ with the outer half of the methane flame in the high-turbulence shear layer region where flame quenching is initiated. At LBO, the region of flame extinction extends farther and the flame is no longer able to sustain burning.

- For hydrogen-enriched flames, the increased width of IRZ approaching LBO limit leads to the flame region to be within the IRZ and sustains reactions in this region where temperature is relatively. Further, as LBO limit is approached, the excess reactant with the high mass diffusivity hydrogen in the shear layer diffuses more rapidly into the IRZ with a favorable combustion environment. Reactions take place within the IRZ with the help of longer residence times, and serves as a pilot flame to re-ignite reactants in the shear layer.

CHAPTER 6 : FLAME STRUCTURE CHARACTERISTICS

6.1 Introduction

In this study, the main objective is to investigate the topological properties of lean flames as equivalence ratio is reduced and LBO limit is approached for both methane and hydrogen-enriched flames. As noted earlier, the statistical flame properties capture the effect of several key flame-front mechanisms that can potentially play an important role in LBO, and an effort is made in this paper to understand the cumulative effect of these mechanisms via statistical flame-front properties. These statistics include flame orientation angle, flame brush thickness, and flame curvature. Considering the flame is expected to be very unstable and vulnerable to small perturbations approaching LBO, OH-PLIF imaging, which is a non-intrusive, laser-based diagnostic technique, is used to capture the flame structure and the flame front as LBO limits are approached. These image-data and the identified flame front are then processed for the flame structure properties analysis.

Table 6-1 Experimental test matrix (hydrogen percentage based on volume basis)

Fuels	Φ_{LBO}	Φ_1	Φ_2	Φ_3	Φ_4
CH_4	0.655	0.67	0.71	0.76	0.81
$40\%H_2$	0.425	0.44	0.48	0.53	0.58
$60\%H_2$	0.315	0.33	0.37	0.42	0.47
$80\%H_2$	0.205	0.22	0.26	0.31	0.36
$100\%H_2$	0.140	0.15	0.19	0.22	0.24

The test matrix, in terms of equivalence ratio, is listed in Table 6-1, with all data taken at a Reynolds number of 11,044 based on the bulk velocity. The percentage of blended hydrogen is defined as $\alpha_{H2}=V_{H2}/(V_{H2}+V_{CH4})$, where V_{H2} and V_{CH4} are the volume flow rates of hydrogen and methane in the unburned fuel mixture, respectively. The global equivalence ratio is calculated based on the blended methane and hydrogen mixture and is defined conventionally as the ratio of stoichiometric air to fuel ratio (AFR) to actual AFR with both fuels present.
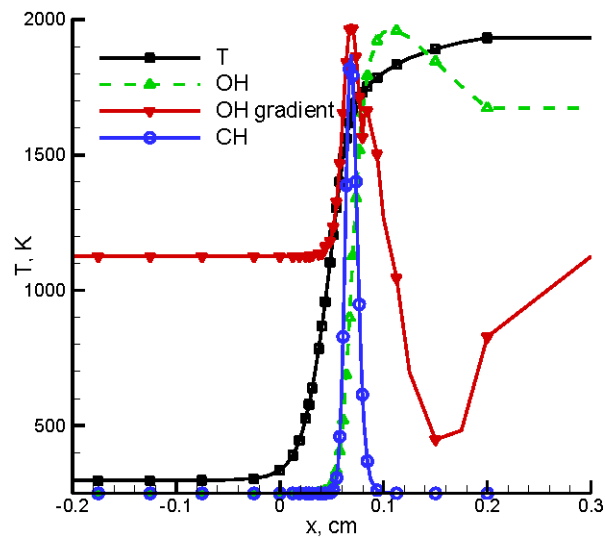
Figure 6-1 CHEMKIN simulation of CH$_4$ premixed flame

Considering that OH exists in the high temperature regions of both reaction zone and burned gases, and that it exists in super-equilibrium concentrations in the reaction zone [113], a strong gradient in the OH-PLIF image can be expected along the flame front due to the strong temperature gradient resulting from the chemical reaction. Therefore, by tracking the gradients of the OH-PLIF distributions, the profile of the reaction zones can be detected more precisely compared to a flame-front identification directly based on OH-PLIF intensity level, the one discussed in data processing chapter. As shown in

Figure 6-1, the CHEMKIN 1D simulation result of a laminar premixed methane flame at Φ=0.81 shows that the OH concentration peaks slightly later than CH concentration, while the location of the maximum gradient of OH coincides with the location of the maximum CH concentration. In the structure of a premixed flamelet, CH is presented in the inner layer of large chemical reactivity [114]. It therefore indicates that the maximum gradient of OH is located within the primary reaction zone, and so it has been extensively used to identify flame fronts [115, 116]. Therefore, in this study, the flame front detection technique based on the gradients of OH-PLIF images was employed. The basic procedure is shown in Figure 6-2. First each raw OH-PLIF image was subtracted from a background image taken in the absence of a flame. This background-corrected image was then filtered by a Gaussian filter to minimize the digitalization noise and normalized with the maximum OH-PLIF signal. Finally the flame front, identified by thresholding the gradient of the OH fluorescence field, was detected by using the Canny edge detection algorithm [117].
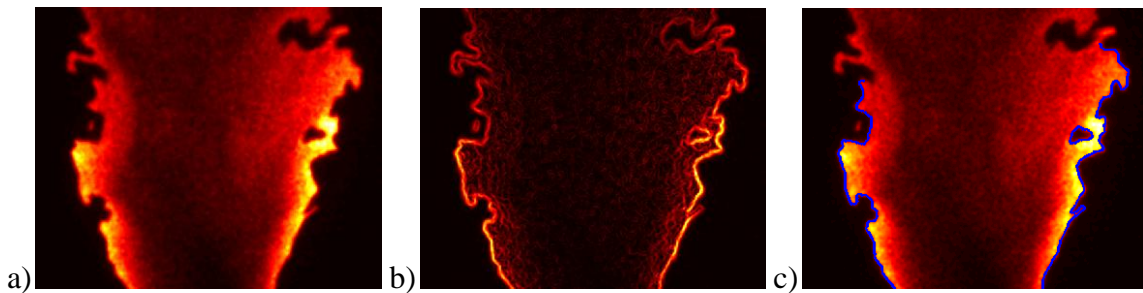
Figure 6-2 Flame front detection procedure: a) background corrected and filtered OH-PLIF, b) gradient of OH-PLIF, and c) OH-PLIF superimposed with detected flame fronts

6.2 Flame Brush Thickness
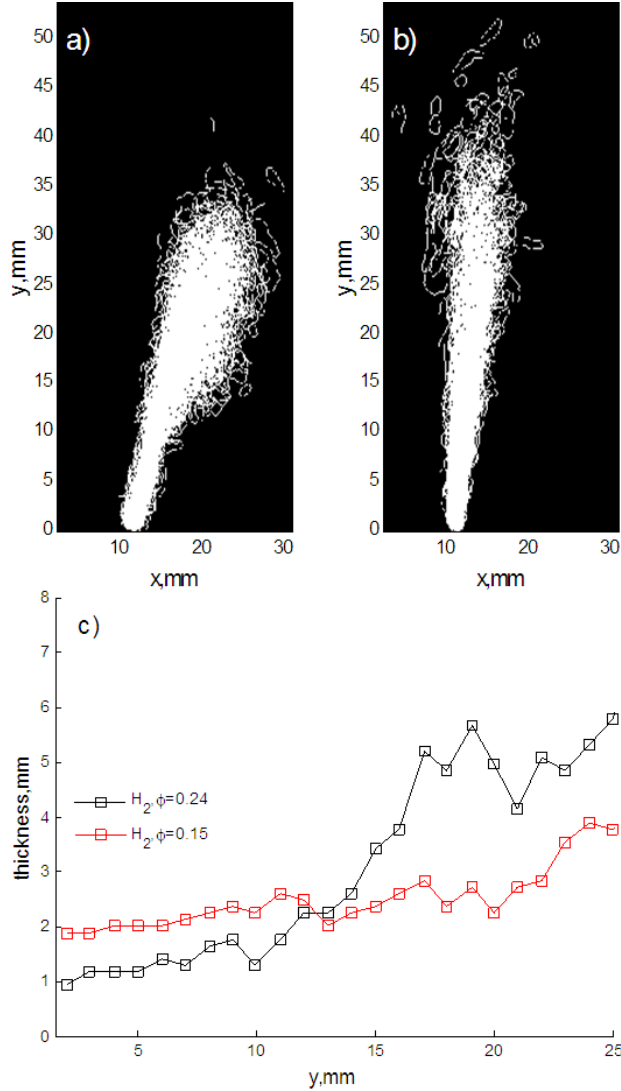
Figure 6-3 Flame brushes of 100% H$_2$ flames for a) Φ=0.24. b) Φ=0.15. c) Flame brush thickness.

Turbulent flame brush, one of important flame front properties describing the spatial distribution of heat release of a turbulent flame, represents the span from the mean flame front in which instantaneous flame realizations fluctuate, and therefore is an estimation of flame front fluctuation and an indication of instability. The instantaneous flame fronts were identified as described above based on the OH gradients from each background

59

corrected OH-PLIF image, then the whole sequence of images were processed to yield the time ensemble of flame fronts, as shown in Figure 6-3a and b of RHS flames for H_2 fuels with equivalence ratios of 0.24 and 0.15, respectively. To evaluate the flame brush thickness at different heights, the full width of half maximum of instantaneous flame front counts at a given height was used to estimate the flame brush thickness, and shown in Figure 6-3c. First, for both equivalence ratios of 0.24 and 0.15, the flame brush thickness grows gradually with axial distance, an observation consistent with prior studies [118, 119, 120, 121]. Flame brush thickness grows according to the turbulent diffusion law [120]. With Taylor hypothesis of y=Ut, where U is the mean gas flow velocity in the axial direction and t is time, the dependence of flame brush thickness on the axial distance can be transformed to the dependence on time. According to Taylor theory of turbulent diffusion, the relation between flame brush thickness δ_T and turbulent dispersion σ then can be derived as $\delta_T \sim \sigma \sim u't \sim u'y/U$, for flame close to flame holder [29]. Therefore δ_T grows with axial distance. Second, as equivalence ratio decreases from 0.24 to 0.15, flame brush thickness increases to maximum of twice (from ~1 mm to 2 mm) in near field (y<13 mm). For all other fuel compositions tested, they have a similar trend as in Figure 6-3c. It indicates that the local turbulence is relatively increased in the near field as equivalence ratio decreases and LBO limit is approached. This may arise from the combination of increased local extinction events and alternating variations of strain rate close to center-body. The results demonstrate that the ultimate blowout may be caused the reduced stabilization of the flame root close to center-body, and therefore modifying the flow field in this region in burner design to better sustain the flame root would extend the LBO limit.

6.3 Flame Orientation Angles
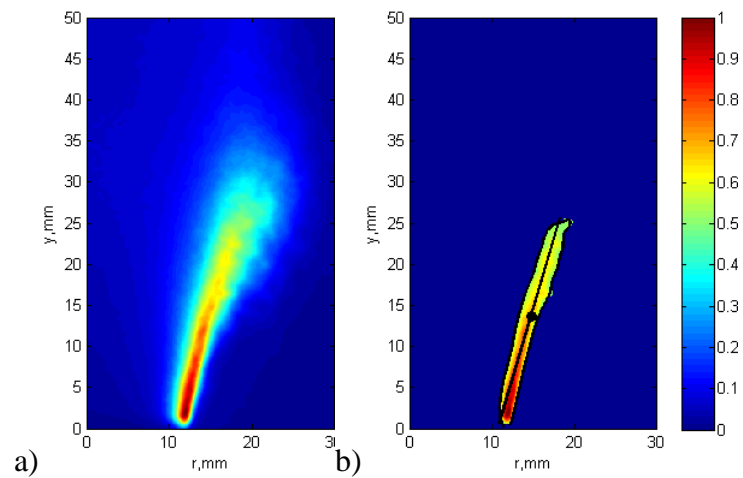
Figure 6-4 Estimation procedure of mean flame position: a) time-averaged OH-PLIF, and b) masked time-averaged OH-PLIF superimposed with line segment presenting flame
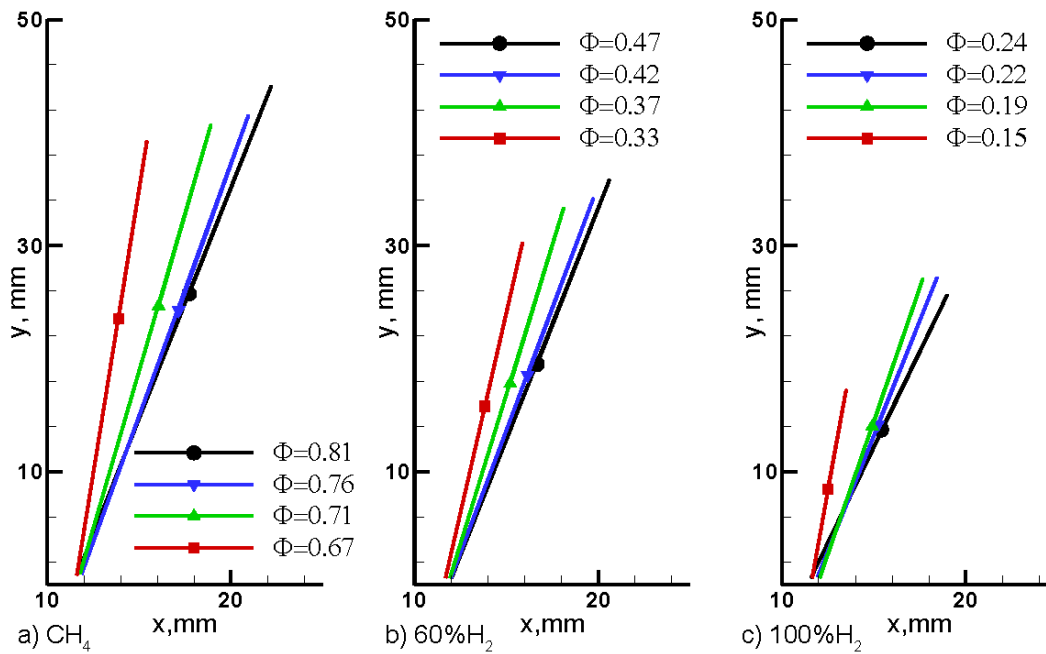
Figure 6-5 Mean flame positions for a) CH$_4$, b) 60% H$_2$ and c) 100% H$_2$

Although detectable amounts of OH exist in both the reaction zone and the high temperature product region [116, 122], as shown in Figure 6-1, the locations with high level of OH fluorescence represent regions in which the reaction mostly likely takes place. In order to examine the spatial position change of flame structure as equivalence ratio reduces, the ensemble of OH-PLIF images was used to estimate the mean flame postion and flame length. The time averaged OH-PLIF image in Figure 6-4a) is masked with its 50% the maximum fluorescence signal, and then a line segment, representing the mean flame structure position and flame length, is estimated using least-squares regression as showed in Figure 6-4b). The corespending results are shown in Figure 6-5a)- 5c) for CH_4, 60%H_2 and 100% H_2 flames, respectively. For all measured cases, as equivalence ratio deduces, the flame length decreases resulting in reduced reactivity, and the flame orientation angle between the flame fronts and dump plane is increased. In fact, the root cause for this observed change in flame orientation angle may be explained by the basis of the source terms of the vorticity transport equation:

$$\frac{D\boldsymbol{\omega}}{Dt} = \boldsymbol{\omega} \cdot \nabla \boldsymbol{V} - \boldsymbol{\omega}(\nabla \cdot \boldsymbol{V}) + \frac{1}{\rho^2}(\nabla\rho \times \nabla p) \qquad (6\text{-}1)$$

Equation (6-1) describes the invisid transport of vorticity $\boldsymbol{\omega}$. On the right hand side of the equation, the first two terms represent the effects of vortex stretching and the gas expansion due to heat release, respectively. The third term accounts for the baroclinic torque effect. For viscous flow, there will be another term for contributions of viscous diffusion and dissipation. As equivalence ratio decreases, the reduced heat release leads to decrease in density jump across the flame brush thickenss. The conbination of reduced density dilation ratio and the increased thickness results in lower density graident, and thereby less generation of positive vorticity (pertaining to right hand side flame as shown

in Figure 6-4 inside the flow resirculation zone, which induces negative pressure gradient, and in turn, leads to negative velocity along the axis. Then the slight recovery of adverse pressure gradient leads to the downstream convection of reaction zones, resulting in an increased flame orientation angle and shrunk flame toward internal recirculation zone .

6.4 Distributions of OH-PLIF Maxima
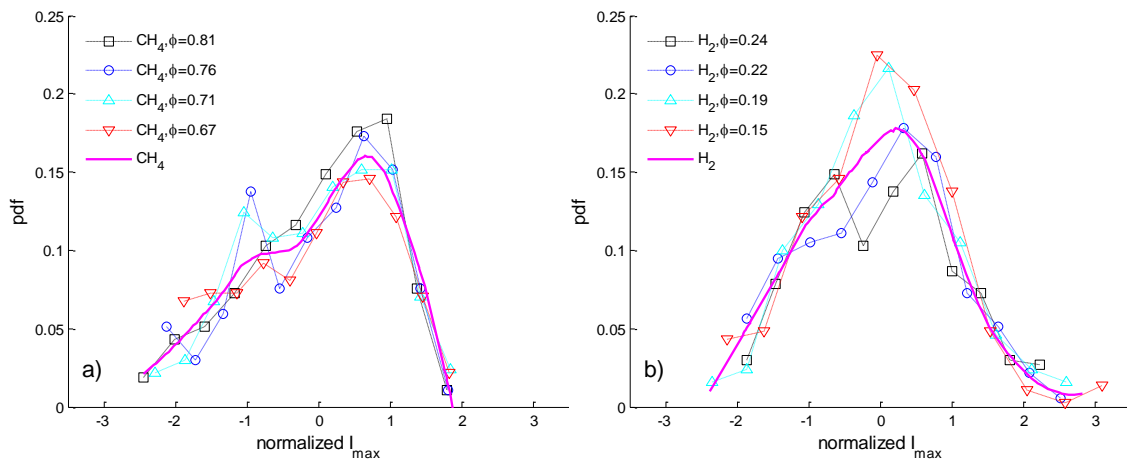
Figure 6-6 Distribution of normalized OH-PLIF maxima for a) CH$_4$ and b) 100% H$_2$.

Since linear fluorescence measurement was used here, the OH fluorescence intensity can be used to reasonably represent the relative OH concentration. The maximum OH concentration within the flame front is a good measure of the chemical reaction intensity in the flame [123]. For a given fuel composition, instantaneous maxima of OH-PLIF signal in the image sequence were indentified, subtracted with their mean value, and then normalized with their deviation. The distributions of normalized OH-PLIF maxima are shown in Figure 6a)- 6b) for CH$_4$ and H$_2$ flames, respectively. For tested conditions, the distribution pattern does not vary much with equivalence ratio for each flame, while it

changes with fuel composition- negative skewed (skewness= -0.56) in CH_4 flames and nearly even undefined (skewness= 0.08) in H_2 flames, that is, the mass of the distribution is concentrated on the right side of the mean for CH_4 flames and relatively evenly spread on both sides of the mean for H_2 flames. In fact, the way OH-PLIF maxima are picked here is to implicitly select the reaction regions positively enhanced by curvature, if any, because it always unbiasedly chooses the instantaneous maximum fluorescence signal in each OH-PLIF instant. For a steady and high turbulent flame, however, the dominant influence on flame wrinkling is the turbulence [124], so the distribution of OH maxima should be close to Gaussian. Considering the randomness of running experiment and taking each data set, and distribution of OH maxima in a same pattern for all four equivalence ratios for each fuel composition, it is reasonable to assume the OH-PLIF measurement operated at 5 Hz does not under-sample the OH maxima statistically. Then, the relatively even distribution of OH maxima implies H_2 flames are relatively steady, while the negative skewed distribution indicates CH_4 flames are unsteady, i.e., processing vortex core, strong flame quenching or rolling present. Actually, in our another experimental test with high speed imaging [125], it was found that methane flames are strongly asymmetric with great reaction strength in left and right periodically about 10-15 Hz, while hydrogen enriched flames burn in a more axisymmetric structure. These results demonstrate that fuel composition can affect the LBO control process via altering flame response.

6.5 Flame Front Curvature

To study the flame wrinkling behavior as LBO limit is approached, the flame curvature probability density functions (PDFs) are calculated. The instantaneous flame front curvatures are calculated based on the OH gradients from each OH-PLIF image and then the whole data set obtained from the image sequence are equally divided into 51 bins to calculate the PDF distributions. Figure 6-7a and c show the flame curvature distributions for CH$_4$, 60% H$_2$, and 100% H$_2$ flames, respectively. Here, three different equivalence ratios per case were chosen to present their PDFs for clarity. As the LBO limit is approached, the curvature distribution is narrowed in CH$_4$ flames in Figure 6-7a), and more evidently as hydrogen blend increases as in Figure 6-7b)-c). Comparing Figure 6-7a)-c), it is found that: 1) the calculated range of flame curvature increases with hydrogen blend: about $\pm 3mm^{-1}$ for CH$_4$ flames, $\pm 3.5\ mm^{-1}$ for 60% H$_2$ flames, and $\pm 4\ mm^{-1}$ for 100% H$_2$ flames, respectively; 2) the flame curvature distribution shifts toward positive side as hydrogen content increases.
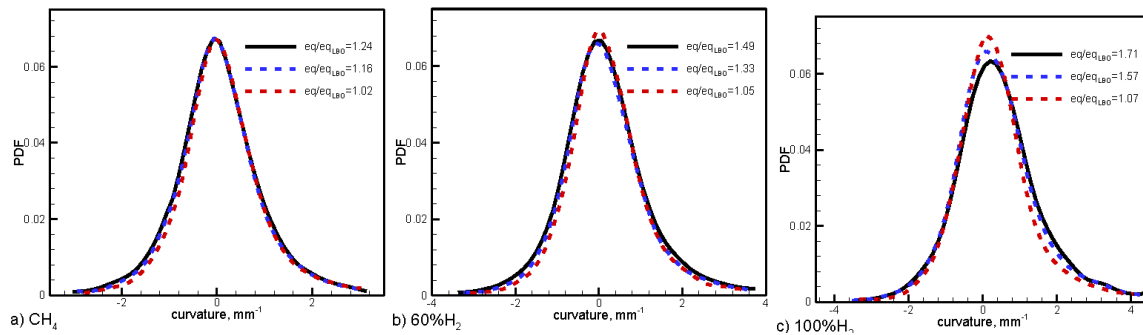
Figure 6-7 Flame curvature distributions for a) CH$_4$, b) 60% H$_2$ and c) 100% H$_2$.

To interpret the curvatures shown in Figure 6-7a)-c), the mean, standard deviation, skewness and kurtosis of the curvature distributions are calculated and shown in Figure 6-8. Figure 6-8a) show all mean flame curvatures are positive, indicating that flames burn

in spherical structures convex with respect to reactants, as opposed to cylindrical (zero curvature) or saddle (negative curvature) configurations, especially for high hydrogen level of fuels due to the high preferential diffusivity. In addition, as equivalence ratio decreases, the mean flame curvature gradually increases in CH_4 flames while it decreases in H_2 flames. In 60% H_2 flames, there is no monotonic trend observed in mean curvature but seemingly behaving in a way as the transient between CH_4 and H_2 flames.
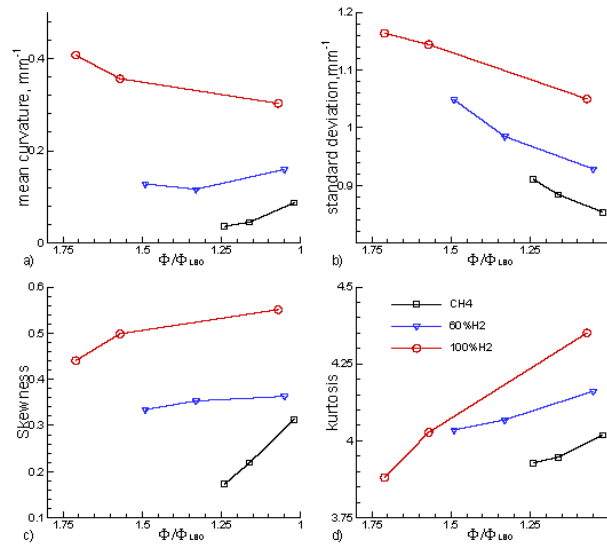
Figure 6-8 Moments of curvature PDFs: a) mean, b) standard deviation, c) skewness, and d)Kurtosis

It should be noted that, furthermore, the increase (in methane flames) or decrease (in hydrogen flames) in the mean flame curvature is relatively small variation in regard to the same type of fuel. For example, all measured mean flame curvatures are less than 0.1 mm^{-1} in methane flames even though increasing as equivalence ratio decreases, while they are all greater than 0.3 mm^{-1} in hydrogen flames albeit decreasing as LBO limit is approached. These relatively small variation indicate that as equivalence ratio decreases, there is a reduced prevalence of larger spherical features for methane flames, whereas a reduced dominance of smaller spherical features for hydrogen flames. That is, the

66

relatively slight increase in mean curvature for methane flames does not sustain the reaction subject to higher flame stretch (negative effect for Lewis ~1), leading to LBO happening at a higher equivalence ratio, while the fairly small decrease in mean flame curvature (but still at least 3 times higher than methane flames) in hydrogen flames survives the flame against relatively lower flame stretch (positive effect for Lewis <1), leading to LBO occurring at a lower equivalence ratio.

Figure 6-8b)-d) show that as equivalence ratio decreases the standard deviation of the flame curvature decreases for all cases, while both the skewness and kurtosis increase. Higher skewness indicates a further bias to spherical burning structures, that is, flame burns more in convex curves toward reactant side and quenches more in concave areas. Larger kurtosis (>3) means the distribution becomes peaky compared to normal distribution (=3), and further away from Gaussian distribution. It indicates that the dominant effect of turbulence on flame wrinkling is reduced and the fuel preferential diffusivity effect increases, promoting further flame wrinkling and even cellular burning structure featured with small scale wrinkled flame fronts, localized regions of intense reaction and quenching. Therefore, it can be expected that the fuel properties would play an important role in the final LBO control process.

6.6 Conclusions

In a swirl stabilized combustor, the flame structure characteristics near LBO and the effects of hydrogen addition have been experimentally investigated by using OH-PLIF imaging over five types of fuel mixtures from pure methane to pure hydrogen. The flame structure properties have been calculated in terms of flame brush thickness, curvature,

length and orientation angle between flames and dump plane. As equivalence ratio decreases and LBO limit is approached, the major conclusions are as follows:

- Flame brush thickness increases in near field, indicating increased local unsteadiness. It demonstrate that the ultimate blowout could be caused the reduced stabilization of the flame root close to center-body, and therefore modifying the flow field in this region in burner design to better sustain the flame root would extend the LBO limit.

- The conbination of reduced density dilatation ratio and increased flame brush thickenss decreases the density gradient across flame brush thickness, leading to reduced baroclinic torque effect on induced negative axial velocity, increased flame orientation angle between flames and dump plane, and thereby shrunk flame toward internal recirculation zone .

- The distribution pattern of OH maxima does not change much with equivalence ratio for a given fuel composition, while it changes with fuel composition. It is negative skewed (skewness= -0.56) in CH_4 flames and nearly even undefined (skewness= 0.08) in H_2 flames, indicating fuel composition can affect the LBO control process via altering flame response.

- The flame curvature distribution is narrowed in CH_4 flames, more evidently as hydrogen blend increases. And it shifts toward positive side as hydrogen content increases. The calculated range of flame curvature increases with hydrogen blend: about $\pm 3\ mm^{-1}$ for CH_4 flames, $\pm 3.5\ mm^{-1}$ for 60% H_2 flames, and $\pm 4\ mm^{-1}$ for 100% H_2 flames, respectively.

- The relatively slight increase in mean curvature for methane flames does not sustain the reaction subject to higher flame stretch, leading to LBO happening at a higher equivalence ratio, while the fairly small decrease in mean flame curvature (but still at least 3 times higher than methane flames) in hydrogen flames survives the flame against relatively lower flame stretch, leading to LBO occurring at a lower equivalence ratio.

- The increase in both skewness and kurtosis of PDF distribution of the flame surface curvature shows that flames are more inclined toward spherical burning structure, and fuel preferential diffusivity effect on flame wrinkling increases, promoting further flame wrinkling and even cellular burning structure featured with small scale wrinkled flame fronts, localized regions of intense reaction and quenching .

:

CHAPTER 7 : HIGH SPEED IMAGING AT LBO LIMITS

7.1   Introduction

In this experiment, the main objective is to experimentally investigate the LBO transient behavior of unconfined and confined premixed methane flames with different levels of hydrogen addition, and to characterize the flame front behavior and time scales as lean blow out occurs. Measurements mainly include high speed imaging of OH* chemiluminescence and photo-diodes for integrated light intensities (both for time scales), and planar laser induced fluorescence imaging of OH (for flame front behavior). The corresponding experimental setup is shown in Figure 7-1.

Additionally, to estimate temperature effect in extinction transition, temperatures on center-body and quartz shell wall (for confined flames) are recorded at 1000 Hz by using two K-type surface thermocouples made from 0.013 mm thickness thermocouple alloy foil with 0.05 mm diameter leads. One thermocouple is placed on the inner surface of center-body, and the other one is installed on the outer surface of the quartz shell with a distance of 25.4 mm (1d) from burner dump plane.

A key contribution of this paper is the measurement of an extinction time scale representing the LBO event. It was observed from the high speed photodiode and chemiluminescence images or signals that the path to extinction was inherently unsteady with a defined periodicity (10-15 Hz), and that immediately preceding extinction there was a rapid drop off in the emitted intensity which could be represented by an extinction time scale.

In presenting the results, we will first discuss the LBO limits and the extinction time scale, and then examine the flame front characteristics and the fluctuation of heat

release rate, and finally inspect the flame dynamics from high speed imaging. It is observed that the extinction time scale behaves differently for confined and unconfined flames, is correlated with the heat release fluctuations, and they both have a strong dependence on the hydrogen content in the fuel feed.
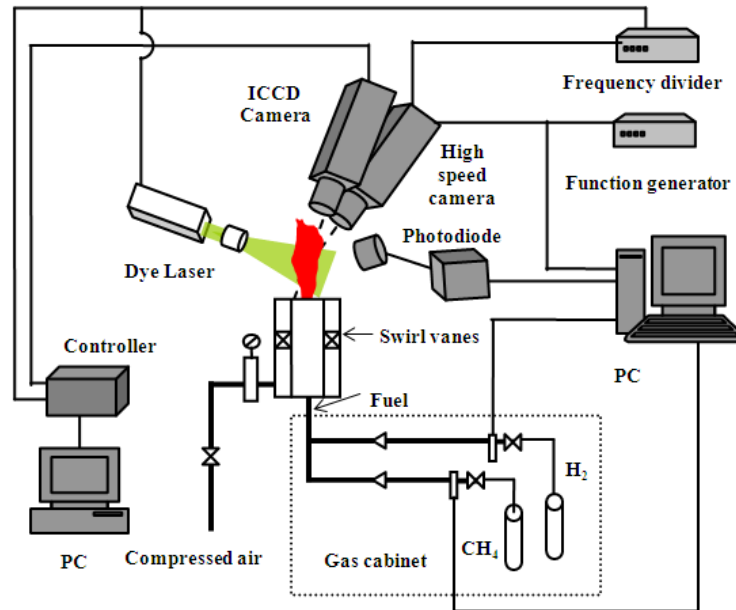
Figure 7-1 Schematic view of experimental set-up

7.2   LBO Limits and Extinction Time Scale

A total of 10 different conditions were tested, and for each, the measurements were repeated 5 times to acquire a small statistical sample for averaging and to verify repeatability and consistency in the data. Each LBO limit was calculated by averaging the five equivalence ratios at which the lean blowout occurred. Figure 7-2a) shows the measured LBO equivalence ratio limits with error bars. The maximum measurement uncertainty is about 14%. With hydrogen addition, the LBO limit gradually reduces for both the unconfined and confined cases reaching values in the neighborhood of 0.2. For a

given fuel composition, the confined flame can burn leaner since, due to the presence of a constraining shell, there is no direct entrainment of the cold ambient air and less heat loss compared to the unconfined condition. Further, the confined flame benefits from the stabilization provided by the corner recirculation formed between the combustor shell and the annular shear layer representing the feed stream. In addition, it will be shown in the section on flame stabilization, the confined flame as it approaches LBO moves inwards and burns inside the internal recirculation zone (IRZ) which is a favorable combustion environment with hot combustion products present. This favors a lower LBO, and as observed in Figure 7-2a), the confined flame LBO is about 0.1 lower (ranging from 0.15 lower for pure methane and 0.1 lower for 60% H_2) than the unconfined flame.
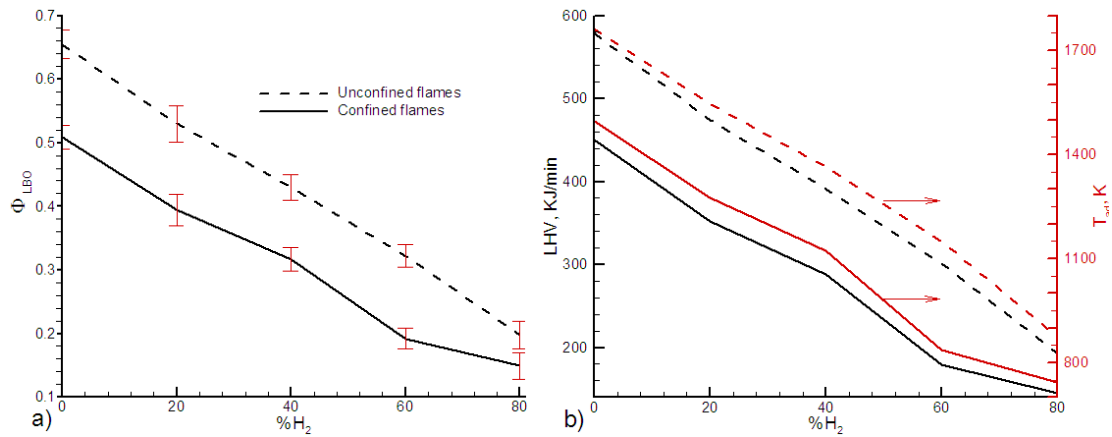
Figure 7-2 Equivalence ratios, heat release rates, and adiabatic flame temperatures at LBO

Figure 7-2b) shows the calculated adiabatic flame temperatures and estimated heat release rates at LBO limits. The adiabatic flame temperatures are calculated using CHEMKIN code with GRI-mech 3.0 mechanism, and heat release rates are estimated by the lower heating values (LHV) of the fuel mixtures. Both adiabatic flame temperatures

and heat release rates decrease significantly and almost linearly with hydrogen addition for both the unconfined and confined flames. For example, for both unconfined and confined cases, the adiabatic flame temperature and heat release rate for 80 % H_2 flames are half and one third those of CH_4 flames, respectively. If only radiation heat loss is considered, the ratio of heat loss to heat generation (heat release rate) for 80% H_2 flames can be estimated to be about 19% that of CH_4 based on a $(T_{ad}^4 - T_i^4)$ assumption for radiative loss, where T_i is either ambient temperature T_∞ for unconfined flames or quartz shell wall temperature T_w for confined flames. This indicates a significant increase in heat retention due to H_2 addition, and coupled with an associated reactivity increase, is another contributing source for lowering LBO limits with H_2 addition.
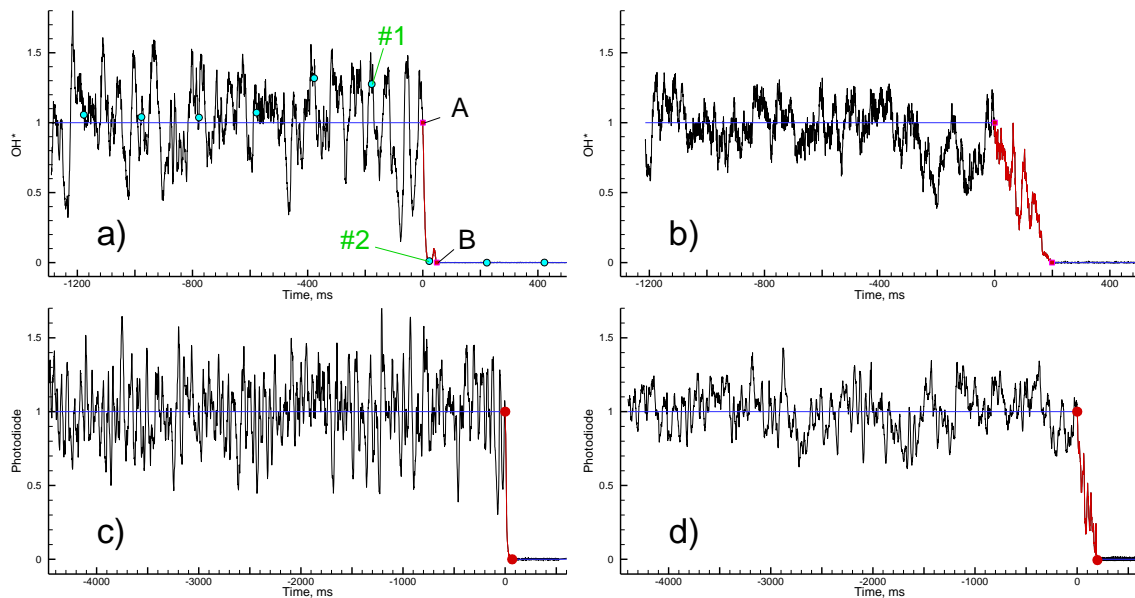
Figure 7-3 Normalized integrated OH* time series for unconfined flames for a) CH₄ and b) 60%H₂, c) and d) are corresponding photodiode data for a) and b), respectively

Figure 7-3a)-b) show the time series of the normalized integrated OH* signal obtained from the high speed imaging for the unconfined flames. The OH* signal is normalized by the time-averaged OH* signal up to the point marked A in Figure 4a

which is identified as the last point in the time trace reaching the normalized value (i.e., after this point the signal begins to drop off reflecting the last stages of LBO). A similar behavior and time scale is confirmed with the corresponding data recorded by a photodiode, as shown in Figure 7-3c)-d), for an extended period of the last five seconds. The results for methane only are shown in Figure 7-3a) and c), and for 60% hydrogen enriched flame, the time series is shown in Figure 7-3b) and d). The OH* signal shown captures the whole extinction transient from a sustained flame just prior to LBO (as shown by the normalized OH* signal oscillating about a normalized value of 1) to complete blow-out (with a zero value representing a background no-signal condition). The LBO extinction time scale is defined as the time increment between the last sampling point reaching the normalized OH* signal value of 1 (identified as point A in Figure 7-3a)) and the first point reaching the background value of 0 (identified as point B). This region A-B, identifying the extinction event, is shown in Figure 7-3 by the red colored curve segment of the integrated OH* signal with end points marked by A and B. With this definition of the extinction time scale, Figures 7-3a) and Figure 7-3b) show that the extinction time T_e for 60% hydrogen enriched flame is 199 ms and is much larger compared to the methane only flame for which the extinction time scale is only 48.5 ms. This difference underscores the significant role that hydrogen plays in the extinction process, but as seen in Figure 7-4, hydrogen addition has a markedly different effect on confined and unconfined flames.

For each measurement condition, 5 separate runs were conducted and the mean estimated extinction times were calculated, averaged and normalized by a characteristic resident time D/U, where D is the outer diameter of the swirler (and also the inner

diameter of the burner), and U is the bulk velocity, respectively. According to our previous flow velocity field measurements with Particle Imaging Velocimetry [31], the width of the IRZ is nearly 1D and the length is about 1-2 D. Since the flame front region is usually an envelope around the IRZ, the scaling time D/U will provide some estimate on the characteristic residence time in the flame region.
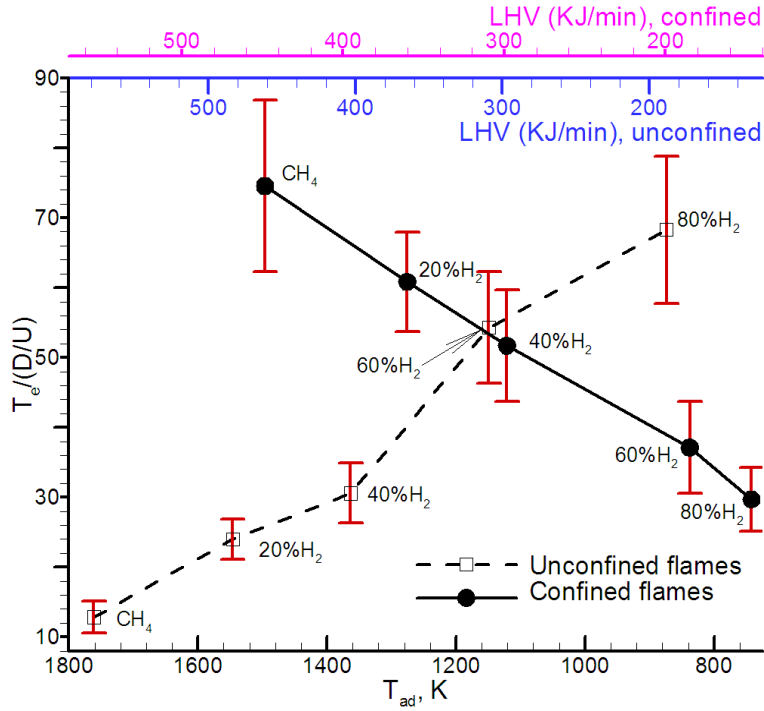
Figure 7-4 Extinction time T_e normalized by the resident time D/U

The normalized extinction time with error bars is plotted in Figure 7-4, with a maximum estimated measurement uncertainty of 18% (based on RMS sum of the repeatability norm and time-resolution norm) as a function of the estimated adiabatic flame temperature (lower horizontal axis) and the LHV (upper horizontal axis). The hydrogen content is indicated at each data point, and as shown in Figure 7-2, %H_2 and T_{ad} are almost linearly correlated. Figure 7-4 shows that all estimated extinction times are

an order of magnitude greater than the characteristic time D/U in the burner. This indicates that for all the conditions tested, the complete extinction of the flame takes much longer than the time for the flow to convect out, supporting the well-stirred reactor concepts of blowout. Further, as the hydrogen blend increases, the estimated extinction time increases for unconfined flames, while it decreases for confined flames.

Figure 7-5 Instantaneous OH-PLIF for unconfined flames for row a) CH4, b) 40% H_2, and c) 80% H_2. In each row of images, first image was captured before extinction starts, and second one during the extinction as denoted by t/T_e

This is a surprising result, and an important one, since the trends are opposite to each other, and the role of hydrogen is significant. As noted in Figure 7-4, the extinction time dependence on hydrogen content and adiabatic flame temperature appears to be almost linear. For unconfined hydrogen-rich flame, as noted earlier, the higher heat retention and lower radiative heat loss combined with higher reactivity is likely to be a reason behind for the longer extinction times. Unconfined methane-rich flames have considerably higher heat losses and shorter extinction times. For confined flames, heat losses are likely reduced due to the shell, and the corner recirculation provides added flame stabilization. In this case, hydrogen has significantly shorter extinction times while, for methane flames the extinction times are extended. Thus, other factors besides heat loss from the flame are in play here, and in order to explore the reasons for such behavior, we will examine the flame front behavior, the heat release fluctuations and the high-speed flame dynamics.

7.3   Flame Stabilization

Figure 7-5 shows the instantaneous OH-PLIF images near and during the extinction transient for the open unconfined flames for methane and for increasing hydrogen blends going up to 80% hydrogen. The specific time instances in these images are shown in Figure 7-3a, where the laser pulses for the synchronized OH-PLIF imaging are marked by solid circle symbols. The first image (#1) is captured right before extinction is initiated (less than one second away from the extinction starting point marked by A in Figure 7-3a), and the second image (#2) is captured during the extinction process and in the near vicinity of the point marked as B in Figure 7-3a. For methane

flames in row a), the OH fluorescence images show high intensity regions near the edge of the center-body (x/d=0.5), and they decay toward the middle of the burner. The regions with high level of OH fluorescence indicate super-equilibrium OH formed in the reaction zones, and the regions with medium and low levels of OH shows the burned gases whose concentration and temperature has decayed towards equilibrium when they were convected away from the reaction zone. Regions without OH represent the gases with low temperature such as ambient air or fresh reactant flow. These instantaneous OH-PLIF images reveal that the reaction for the unconfined flame takes place near the inner shear layer between the incoming swirling fresh reactant flow and relatively hot internal recirculating flow. As the hydrogen blend increases in the images from row a) to row c), the reaction zone marked by high intensity of OH becomes much thinner and more frequently disconnected, but they are still stabilized inside the inner shear layer and along the edge of the center-body. Additionally, the second image in each row shows the flame profile during the extinction process. However, it should be noted that the time instance of the second image relative to the start of the extinction (point A in Figure 7-3a) is not the same for the different fuel blends. For example, the second image in row a) for methane flame is near the half-way mark of the extinction transient (t/T_e=0.46, where T_e is the extinction time scale and t is measured from the start of the extinction process), and shows that the reaction zone is very small compared to that before the extinction, and recedes back to the dump plane. The second image in row b) for 40% hydrogen enriched flame is captured near the end of extinction transient (t/T_e=0.97), and only a small spot of flame is left above the center-body.
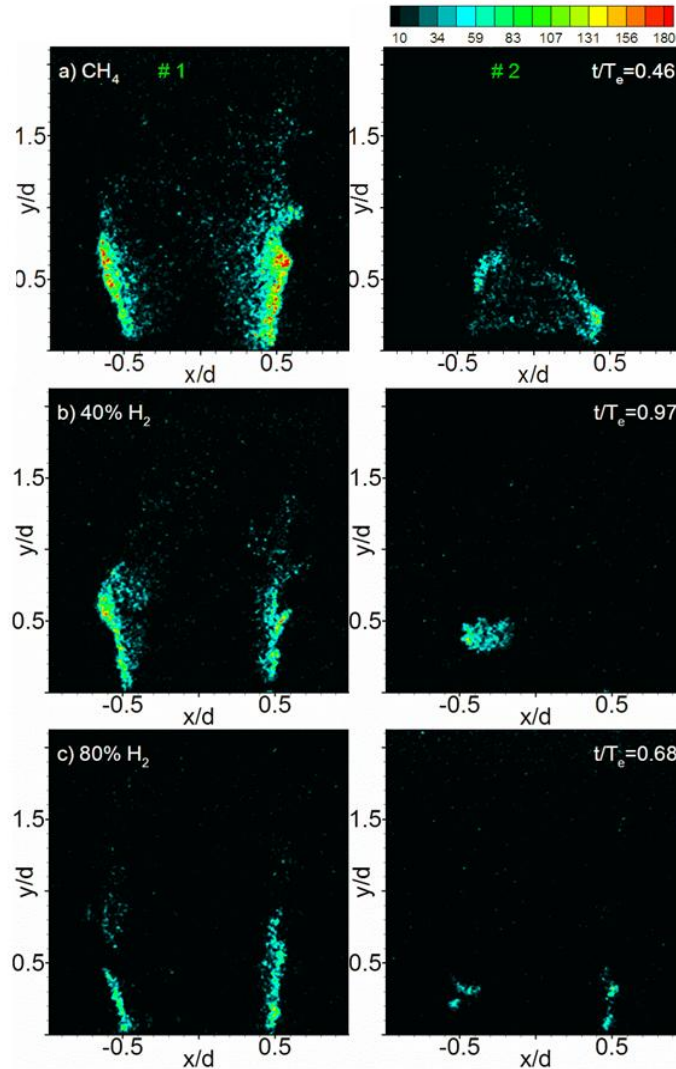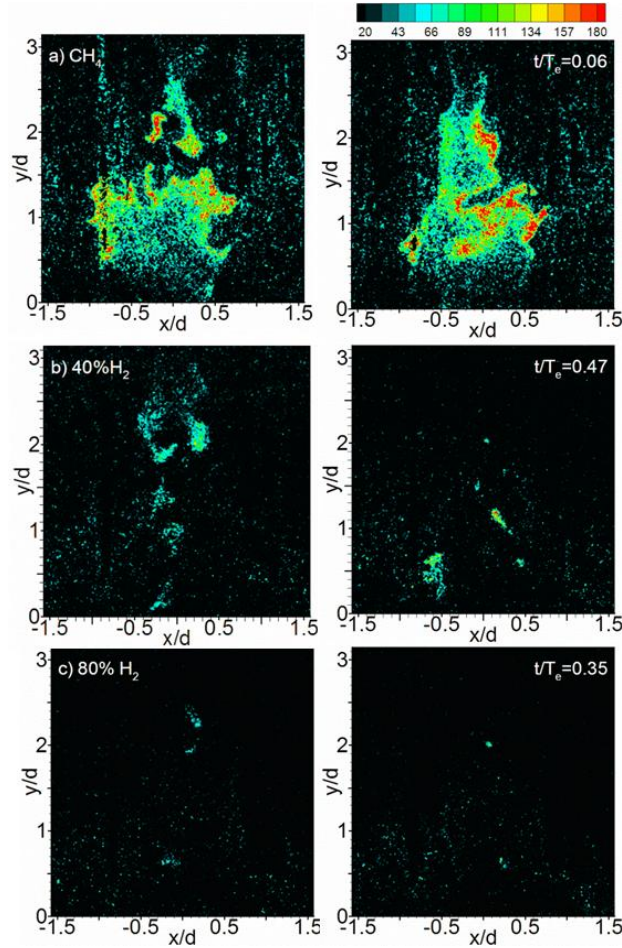
Figure 7-6 Instantaneous OH-PLIF for confined flames for row a) CH4, b) 40% H_2, and c) 80% H_2. In each row of images, first image was captured before extinction starts, and second one during the extinction as denoted by t/T_e

Figure 7-6 shows the OH-PLIF images near and during the extinction transient for the confined flame cases. Compared to Figure 7-5, the confined flames in Figure 7-6 show completely different flame stabilization mechanism near flame extinction. In row a) for the methane flame, the OH-PLIF images clearly show the reaction zone is significant across the middle of the center-body indicating that the reaction takes place inside IRZ, where the relatively high temperature from the recirculated products in the IRZ favors the combustion. This is part of the reason why confined flames can burn at leaner condition. As hydrogen content increases, e.g., in row b) with 40% hydrogen flames, the reaction

clearly moves further inside the IRZ and near the axis of the burner, and the flame shape transitions from a conical shape to a columnar shape, indicated by the elongated and more complex structure of the high OH-level region. This transition to columnar shape is accompanied by strong unsteadiness, and we believe this is responsible for the decreasing
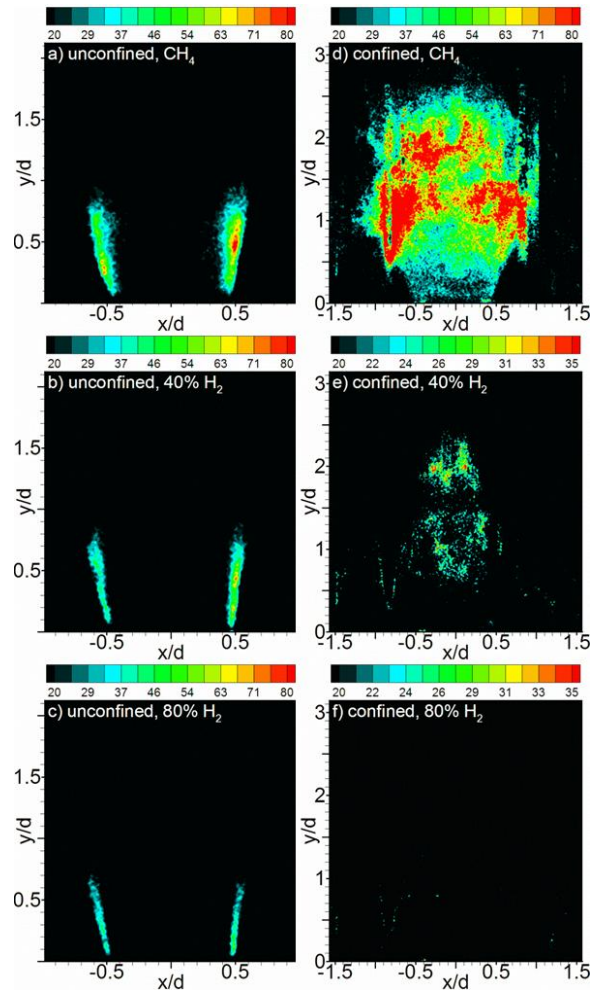
Figure 7-7 Time averaged OH-PLIF over very last 5 seconds before extinction

extinction time scale with hydrogen addition in confined flames. As hydrogen blend increases further, the flame and reaction regions become more isolated and localized, exhibit greater unsteadiness, and with only small localized spots of relatively high OH fluorescence level observed in the 80% hydrogen flames (shown in row c).

Figure 7-7 shows the time averaged OH-PLIF images that are averaged over the last 5 seconds before extinction starts. Within this 5 seconds, the variation of global equivalence ratio is negligible considering the fact that the change in global equivalence ratio is only 0.01 per minute. Figure 7-7a)-c) for the unconfined flames clearly show that all unconfined flames are stabilized near the inner shear layer and along the edge of center body of the burner, and the time averaged reaction zone reduces in terms of intensity and size as hydrogen addition increases. Figure 7-7d)-f) of confined flames indicates that in all the confined flames the flame stabilization take place inside the IRZ and near the the burner axis. For the 80% H_2 flame the reaction is extremely lean and isolated, and the time averaged OH-PLIF image over 5 seconds does not capture the flame shape clearly. Thus, our conclusion is that for the confined flame the IRZ plays an important role in the flame stabilization and as hydrogen content is increased, the flame is increasingly moved inwards into the IRZ (presumably due to the higher molecular diffusivity of hydrogen relative to methane). The IRZ contains recirculated hot products, and provides the ignition source for flame stabilization allowing the flame to burn leaner.

7.4   Fluctuation of Heat Release Rate

The next issue is the reduction in extinction time scale with hydrogen addition for confined flames, and the opposite trend with the unconfined flames. Our preliminary observations noted earlier are that this is related to the flame unsteadiness as LBO is approached. To explore this further, high speed OH* chemiluminescence data was examined. OH* and CH* are the strongest chemiluminescence signals in hydrocarbon flames, and are often used as indicators of heat release rate [32, 33]. Here the integrated

OH* from high speed imaging is used to estimate the fluctuation of the heat release rate. Figure 7-8 shows the ratio of RMS (OH* ') and mean (<OH*>) of OH* signal for confined and unconfined flames. With hydrogen addition, the fluctuation of OH*, that is, fluctuation of heat release rate, gradually decreases in unconfined flames (as shown in Figure 7-3a-b and c-d), while it increases in confined flames. The trends shown in Figure 7-8 when compared to those in Figure 7-4 shed important light on the behavior observed for the extinction time scales. Near LBO, the unsteadiness represented by the RMS (OH*) or heat release increase with hydrogen addition in confined flames. The higher unsteadiness implies higher straining rates (assuming stress and strain are related) and therefore the thin flame fronts near LBO are subjected to the high straining and can be quickly extinguished leading to short extinction times. In unconfined flames, the RMS (OH*) levels actually decay with hydrogen addition, and this implies that the flame fronts are subjected to relatively lower straining at higher hydrogen levels for the unconfined flames leading to longer extinction times.
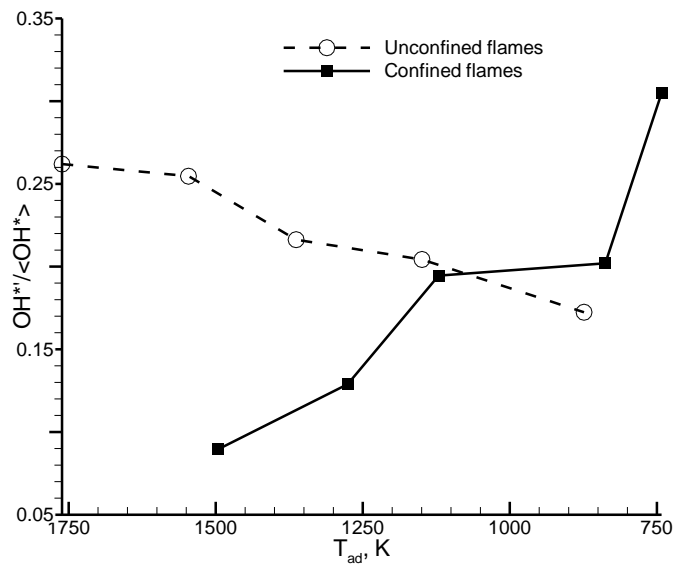
Figure 7-8 OH* fluctuation

82

7.5 High Speed Flame Imaging

In order to further visually investigate the flame dynamics at LBO limits, high speed flame imaging without any spectral filtering were performed with framing rates of 5000 Hz for unconfined flames, and 2000 Hz for confined flames, as shown in Figure 7-9 to Figure 7-12. For each set of images, they are arranged in a time sequence and marked by t/T_e values, where T_e is the estimated extinction time scale as defined and shown in Figure 7-3, and t is the actual time measured back from the extinction initiating point (Point A in Figure 7-3a). In all cases, the plots are shown from t/T_e of -1 to the extinction point of 1. The size of plotting domain is 50×50 mm^2 and 80×80 mm^2 for unconfined and confined flames, respectively. The black dashed line represents the central-axis of the burner.
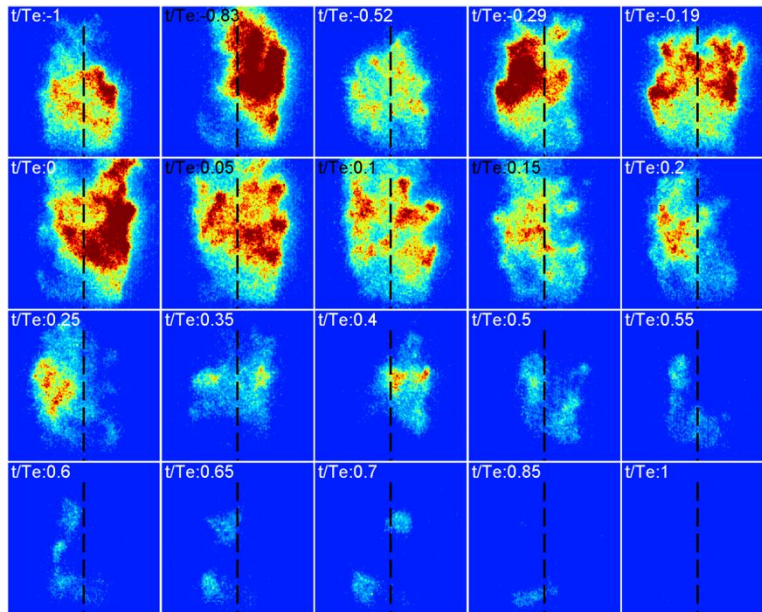
Figure 7-9 Final LBO events for unconfined CH$_4$ flames

For unconfined CH$_4$ flames in Figure 7-9, when the flame is away from the extinction transient (t/T_e <0), one can observe significant regions of extinction alternating

83

from the left (t/T_e=-0.83) to the right (t/T_e =-0.29) with re-light between these asymmetric extinction events. This asymmetric burning structure with strong burning zones periodically appearing on the left and right, along with chemiluminescence fluctuations, continue through to extinction, but the total integrated chemiluminescence decreases gradually as the extinction point is approached. In the images at t/T_e=0.55 and 0.6, weak alternating-spiral-shape flame filaments appear near the center-body, indicating significant flame quenching. In the images at t/T_e=0.6 and 0.7, disconnected reaction filaments are convected downstream. Then, final blowout happens after the flame kernels fail to survive.
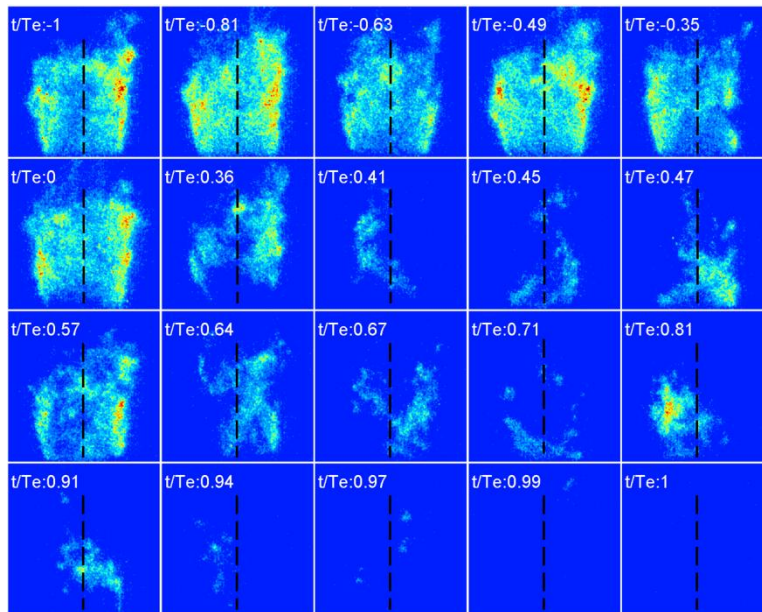
Figure 7-10   Final LBO events for unconfined 60% H$_2$ flames

Thus, for the unconfined 60% H$_2$ flames, away from the extinction transient, the flame profile appears to be symmetric (Figure 7-10) from t/T_e= -1 to 0. Closer to the extinction transient, and between t/T_e=0.36-0.45, loss of symmetry is observed with alternating patterns of extinction and re-light as in CH$_4$ flames. This process is repeated

in sequence with reduced reaction strength till the final flame kernel near center-body fails to survive.

To better assess the differences and investigate the flame dynamics further, another measurement of high speed imaging was carried out for open methane and 60% hydrogen enriched flames, by placing the high speed camera looking down with declination angle of about 30^0. The results of instantaneous image sequence clearly show methane flame is rotating but hydrogen enriched flame is not. These image sequences was then further analyzed by applying proper orthogonal decomposition (POD) and discussed in next section.
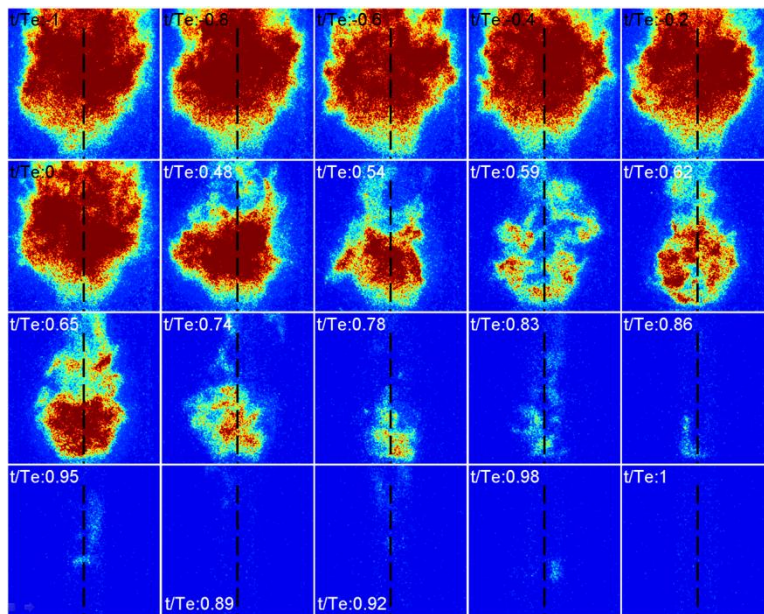
Figure 7-11 Final LBO events for confined CH$_4$ flames

Results for the confined flames are shown in Figure 7-11 for CH$_4$. For $t/T_e<0$, a large and stable conical reaction zone resides downstream and across the middle of the IRZ. Note that for the confined flame, a corner recirculation exists and there is reduced heat loss with confinement, and for these reasons, unlike the unconfined flame, the flame

structure remains relatively stable till t/T$_e$ of 0 providing an extended extinction time. From t/T$_e$=0 to 0.54, the flame shrinks in size and strength, the center of reaction zone gradually moves upstream, and eventually resides inside the IRZ and next to the center-body. During this process, there is a strong pull-back of the high chemiluminescence region along the axis, and the flame eventually recedes and is quenched. Because no significant extinction and re-light events are observed, the overall fluctuation levels and RMS in OH* (and straining rate) are relatively smaller which contributes to an extended time for extinction.
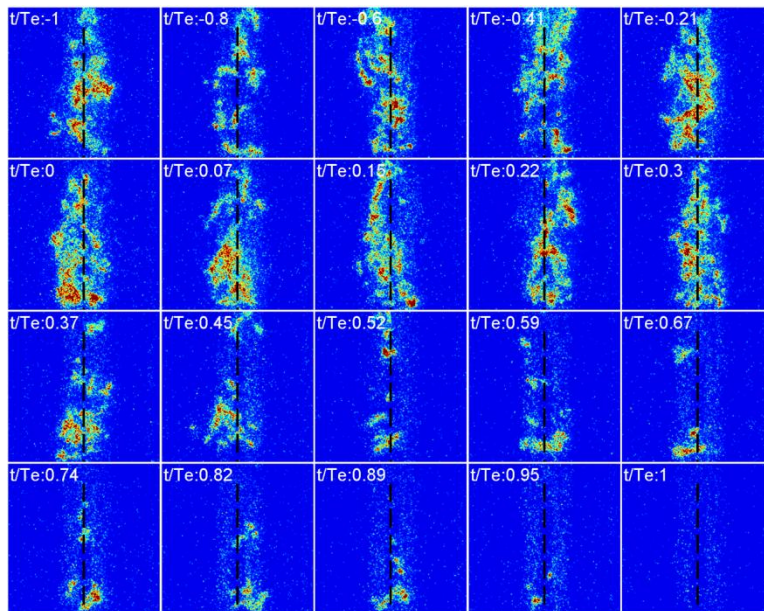
Figure 7-12 Final LBO events for confined 60%H$_2$ flames

For 60% H$_2$ confined flames in Figure 7-12, the reaction evidently takes place inside the IRZ in an elongated columnar shape, and time-resolved images indicate a strongly sinuous swirling motion. Before extinction, the dominant columnar burning structure appears to be helical and is strongly localized with significant unsteadiness as the hydrogen concentration increases. High speed imaging shows that close to LBO, the

localized flame kernels distributed along the middle of the burner is fed by the entrainment of unburnt reactant mixture via the rear of the toroidal vortex of IRZ, leading to higher unsteadiness and heat release fluctuations (OH* RMS), and in turn, higher straining rates resulting in shorter extinction time scales with hydrogen addition. During the extinction transient $t/T_e>0$, the columnar burning structure reduces in length with one end always residing next to the center-body, and eventually shrinks to a spot leading to complete extinction.

7.6 POD Analysis

To further explore the flame front dynamics responsible for the LBO behavior, proper orthogonal decomposition (POD) was applied to the high speed flame images as outlined in data processing section.
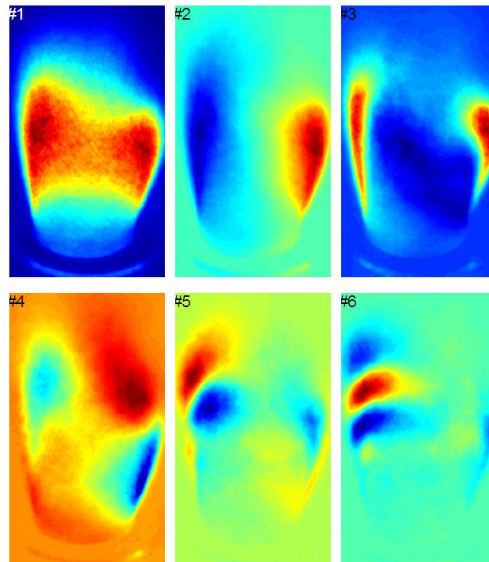
Figure 7-13 First six POD modes for unconfined CH$_4$ flames (flame images captured with 30^0 declination angle).

Figure 7-13 shows the first six POD modes for unconfined methane flames. Modes 1-4 represent the mean flame burning shape, flame rotating, flame flapping inward and outward, and flame jumping up and down, respectively. Modes 5-6 indicate the vortex shedding. Thus, the flame rotating mode is the most dominant feature in this case. The time constant for this mode was then used to do spectral analysis. It shows a distinct peak at ~70 Hz, as shown in Figure 7-14.
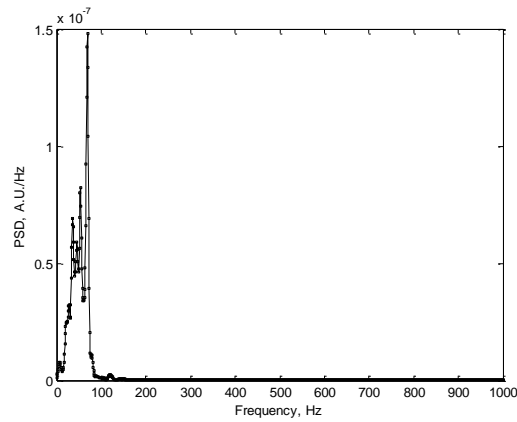
Figure 7-14 Power spectrum for mode 2 for unconfined CH$_4$ flames.
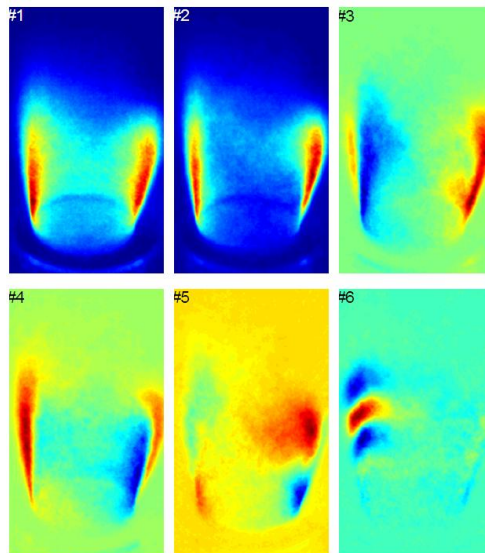
Figure 7-15 First six POD modes for unconfined 60% H$_2$ flame (flame images captured with 30^0 declination angle).

Figure 7-15 shows the first six POD modes for unconfined 60% hydrogen enriched flame. Mode2 mimics mode 1 with correlation coefficient of 0.96, representing the average axisymmetric burning pattern but with less reaction in the recirculation zone. Modes 3-4 are the flame flapping and modes 5-6 represent flame jumping and vortex shedding. Compared to Figure 7-13 of POD modes for methane flame, the major difference is that the dominant burning structure is symmetric and not rotating in hydrogen enriched flame. This may explained by following. At LBO limit, local quenching occurs due to local excessive flame stretching or cold unburnt gas entrainment. To successfully re-ignite the flame, the corresponding minimum ignition energy (MIE) should be reached. And the MIE of methane is much higher than hydrogen. For example, at 25 ^{0}C and 1 atm the MIEs are 0.017 mJ and 0.30 mJ for hydrogen and methane air mixture in equivalence ratio about 1, respectively [126]. Then for methane flame, once local quenching happens, it could be harder to get it re-ignited by neighborhood, resulting in extinguished areas traveling along the swirling flow until more favorable condition is met. Therefore, for methane flames, the appearance of flame rotating with local extinction regions periodically occurring around the axis indicates high straining rates, and leads to strong fluctuation of OH* oscillation and therefore a shorter extinction transient. However, for 60% H_2 flames, due to small MIE and also high molecular diffusivity associated with hydrogen content (leading to local enrichment), they may relight the quenching regions if occurring, and the flame has a relatively symmetric structure till late in the extinction stage, and this elongates the extinction transient.

89
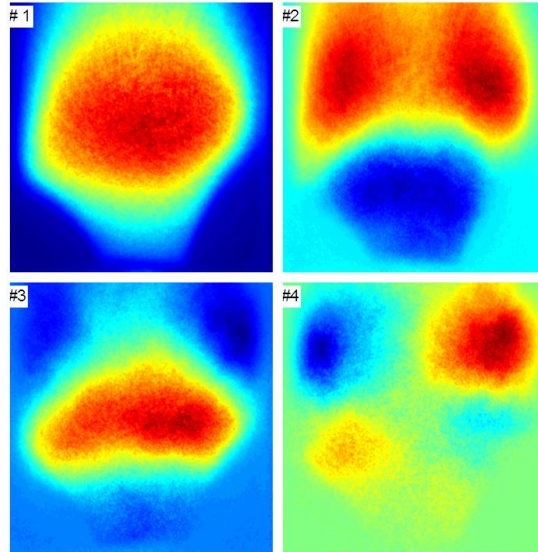
Figure 7-16 First four POD modes for confined CH$_4$ flame.

For confined methane flame, the first four POD modes are shown in Figure 7-16. Mode 2 show the reaction in the counter rotating vortex pair downstream or right above burner tip, while mode 3 represents the reaction in the middle of recirculation zone. As shown in Figure 7-17, the coefficients of mode 2-3 are significantly correlated with a correlation coefficient of -0.83. In fact, these two modes mimic the longitudinal mode of acoustics, representing reaction zone pinching and detaching from the centerbody. FFT show the frequency peak at about 4 Hz. The burning pattern of burning right above the centerbody is dominant especially during the extinction transient, as observed in Figure 7-11. It sustains flame longer due to favorable combustion environment of higher temperature and lower turbulence. Mode 4 is less important and shows the waving of flame tips in the downstream.
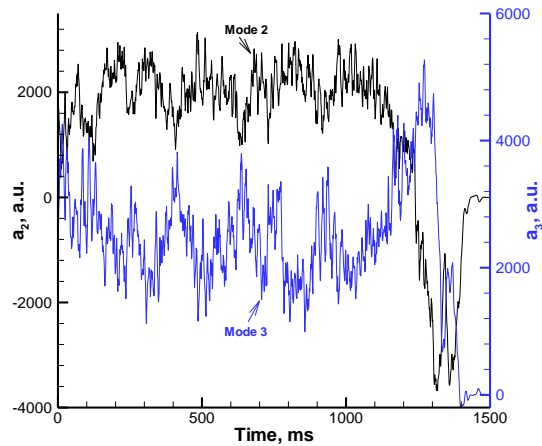
Figure 7-17 POD mode coefficients for confined CH$_4$ flame.
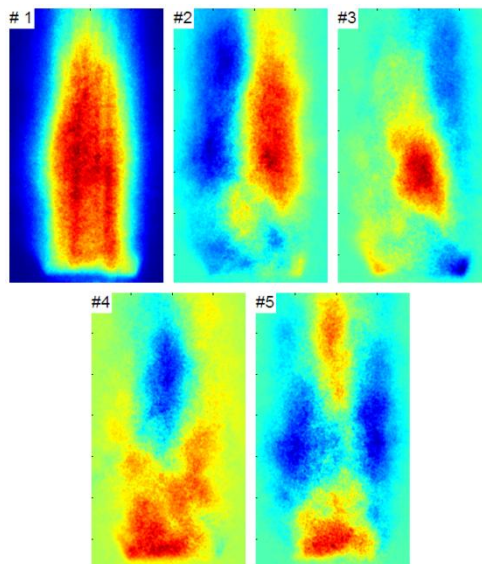
Figure 7-18 First five POD modes for confined 60% H$_2$ flame.

Modes 2-3 of confined 60% hydrogen enriched flames In Figure 7-18, show the flame spiraling around the axis. Mode 4 represents flame burning right above the burner tip or downstream, or the transient between these two conditions. Mode 5 shows flame expands or shrinks radially. The spectra associated with modes 2-4 by applying FFT to their time constants show a distinct frequency peak at 16 Hz as shown in Figure 7-19.

From the time series of images, it is observed that the columnar burning structure is always spiraling and the reaction is fed by the entrainment of unburnt and burnt gases from downstream.
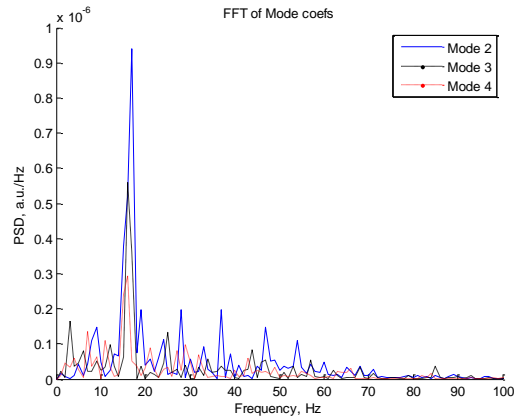
Figure 7-19 Power spectrum for mode 2-4 for confined 60% H$_2$ flames.

7.7   Temperatures on Center-body and Shell Wall
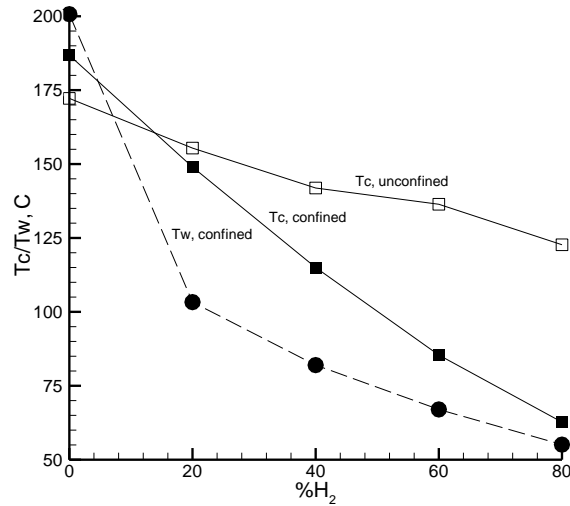
Figure 7-20 Temperatures of center-body and shell wall at extinction.

Since the temperatures at reaction boundaries, such as the center-body tip (T$_c$) and the quartz shell wall (T$_w$) for confined flames, could alter LBO limits and thereby LBO

characteristics, temperatures on these two boundaries have been measured to further evaluate the contributing factors to the inverse trend of extinction time scales in unconfined and confined cases, and shown in Figure 7-20. Temperatures T_c and T_w are calculated by averaging over last one second before extinction is initiated. It shows that from CH_4 to 80% H_2, T_c decreases about 50 ^{o}C in unconfined flames, while it decreases about 130 ^{o}C along with 150 ^{o}C dropping in T_w for confined flames. Thus clearly, flame dynamics plays a major role in unconfined flames since consideration of T_c alone would imply that hydrogen-enriched flames would have shortened extinction times, which is clearly not the case. For confined flames, however, boundary temperatures T_c and T_w show the same trend as extinction time scale with respect to hydrogen addition. This indicates that in confined flames these temperature boundaries could be another factor, in addition to flame dynamics, contributing to the opposite trend of extinction time scale.

7.8   Conclusions

An experimental study of synchronized OH-PLIF and high speed OH* imaging along with light intensity recording was performed in a swirl-stabilized combustor for unconfined and confined hydrogen-blended methane flames with hydrogen levels ranging from 0% to 80% by volume. Conditions close to LBO and during the LBO transient were monitored. The following major conclusions are observed.

1. Hydrogen addition lowers the LBO limit (lower than 0.2 in equivalence ratio), and for a given fuel composition, confined flames can burn at leaner conditions (nearly 0.1 leaner in equivalence ratio) compared to unconfined flames. The calculation of adiabatic flame temperatures and heat release

rates based on LHV shows the significant increase in heat retention with hydrogen addition for unconfined flames which contributes to longer extinction times.

2. H_2 addition increases extinction time for unconfined flames, and reduces it for confined flames. These inverse trends appear to be correlated with the RMS fluctuations of OH*.

3. In unconfined flames, the flames near LBO are stabilized along the inner shear layer between the relatively hot IRZ and incoming swirling fresh reactant flow for all methane and hydrogen enriched cases tested. POD analysis shows periodic flame rotating with local extinction is dominant for methane flames well ahead of the extinction transient, and are potentially associated with high RMS and straining rates leading to shorter extinction times. For hydrogen-enriched flames, the flame structure is relatively symmetric and stable, leading to reduced RMS of OH*, lowered heat release fluctuation, and therefore longer extinction time.

4. In confined flames, the flame front spans the IRZ for methane flames, and is relatively symmetric and stable in the early phases of extinction. For high hydrogen, the flame is within the IRZ due to the higher molecular diffusivity, and flame structure appears to be columnar with high hydrogen addition. Before extinction, the dominant columnar burning structure appears to be a helical swirling motion which results in high unsteadiness, leading to high OH* RMS, and a shorter extinction time. Additionally, reduced temperature boundaries at center-body tip and

quartz shell wall could be another contributing factor, since it shows the same trend as extinction time with hydrogen blend.

5. In all the tested confined and unconfined flames, the final extinction occurs shortly after the reaction zone immediately above the center-body fails, indicating a significant effect of this flame root on the final extinction. It is suggested that the ability to better sustain this flame root might extend the LBO limit to leaner conditions.

The results of this study can provide guidance to a combustion designer. While no design optimization is done here to extend LBO or extinction times, the results of this study indicates that for confined flames, adding additional hydrogen with higher molecular diffusivity than methane causes the flame structure to be located within the IRZ. Thus extinction times are controlled by the flow dynamics in the IRZ. Suitable geometric design changes may be needed to control or alter such behavior. These are left for future efforts.

CHAPTER 8 : SYNCHRONIZED PIV AND OH-PLIF MEASUREMENTS

8.1   Introduction

In this chapter, the simultaneous measurements of PIV and OH-PLIF are performed to assess the responses of the flow field and flame structure as equivalence ratio decreases and hydrogen content is increased. Methane only, 40%, 60%, and 80% hydrogen blended fuel mixtures are chosen, and for each fuel composition four different equivalence ratios are tested. The test matrix along LBO limits are shown in Figure 8-1 Test conditions. The corresponding temperatures on the center-body in Figure 8-1b) shows the maximum temperature variation in same fuel composition is within 25 ^{o}C.
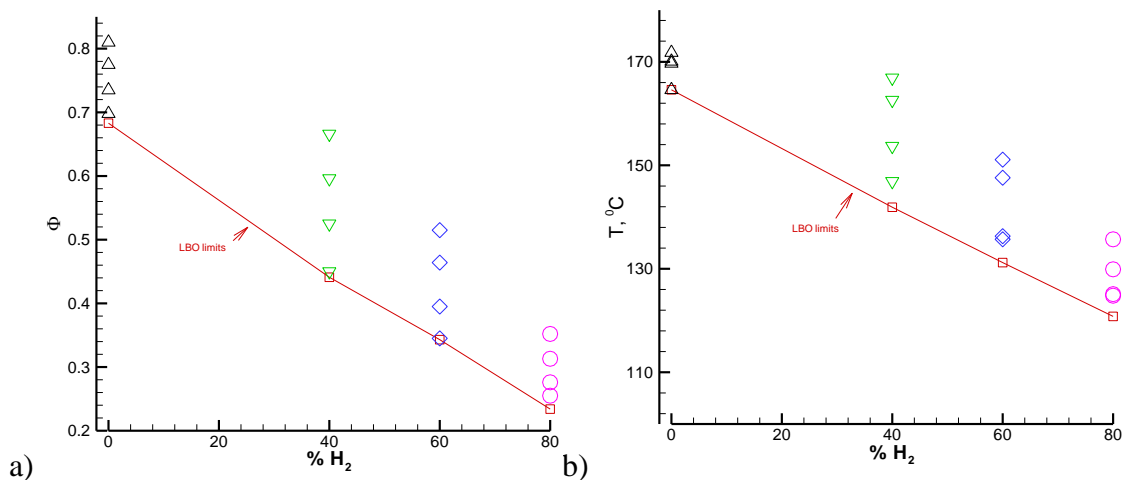
Figure 8-1 Test conditions

Figure 8-2 shows the verification of the mapping between PIV domain and OH-PLIF domain. Figure 8-2a) shows the target plane image captured by PIV camera superimposed with corresponding detected edges of grids on the target plane, and Figure 8-2b) shows the same image taken by OH-PLIF ICCD camera superimposed with the

detected edges of grids from PIV image. It clearly shows the two coordinate system match each other.
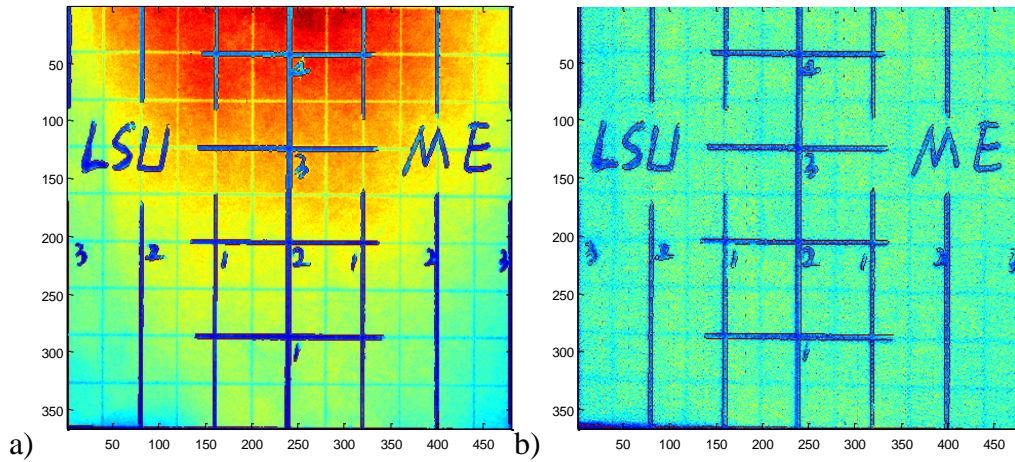
Figure 8-2 Verification of mapping between PIV and OH-PLIF coordinate system

8.2 Correlation between Vorticity Dynamics and Flame Fronts

As discussed in introduction section, the flow field, especially the vorticity dynamics of the flow could play an important role in flame blowout process. And the flame front involves key issues such as flame-vortex interaction, flame-wrinkling, flame holding and their relations to the flow field and turbulence levels. Thus, close scrutiny of flame front and vortex interaction is expected to provide deep insight into the blowout phenomena. Figure 8-3 shows the typical instantaneous PIV and OH-PLIF results for CH$_4$ flames at Φ=0.81. The left panel show the normalized OH-PLIF intensity contour superimposed with velocity vectors and detected flame fronts, which are drawn in thick black lines. The right panel show corresponding instantaneous vorticity contour superimposed with the flame fronts. At this equivalence ratio far away from LBO limit the flame is relatively stable. Figure 8-3 indicates that the flame fronts are wrinkled but connected, and more importantly, they are almost entirely located in low vorticity regions

along the shear layer – in between blue and red vorticity contour regions, that is, high magnitude counterclockwise and clockwise vorticity, respectively.
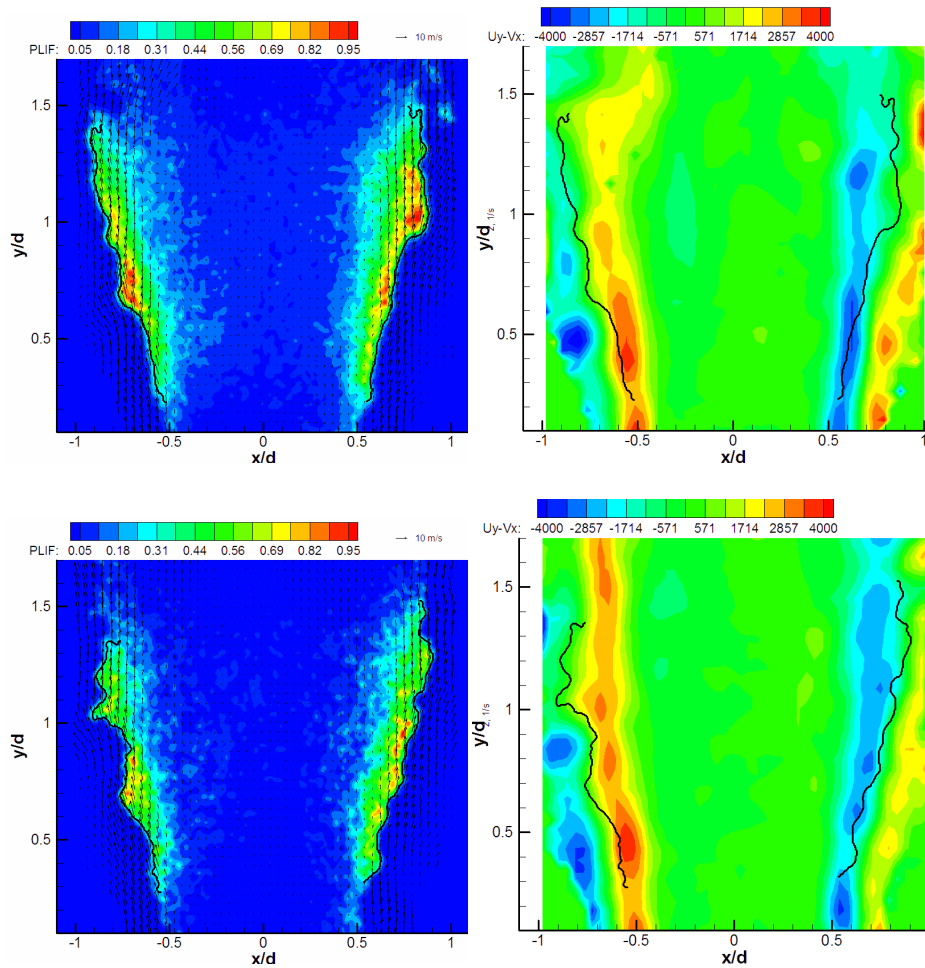
Figure 8-3 Typical instantaneous results of synchronized OH-PLIF and PIV for CH₄ flames at Φ=0.81. Left panel: normalized OH-PLIF intensity contour superimposed with PIV velocity vectors and detected flame fronts. Right panel: out-of-plane vorticity contour superimposed with flame fronts

As equivalence ratio decreases, flame is approaching LBO limit and appears to be unstable. Figure 8-4 shows the typical instantaneous results of simultaneous PIV and OH-PLIF for CH4 flames at Φ=0.70 and near blowout limit. The majority of flame fronts now shifts into the high vorticity regions. And the second image in the left panel of normalized OH-PLIF images clearly shows a break or hole along the flame fronts, as

circled by A and shown by quite low OH-PLIF intensities around the break indicating local low temperature. The corresponding vorticity plot shows this break coincides with high magnitude vorticity regions. Additionally, from the vorticity field, it is noted that the local high vorticity around the flame front break can entrain the unburnt fresh mixture directly into internal recirculation zone and allow reaction there.
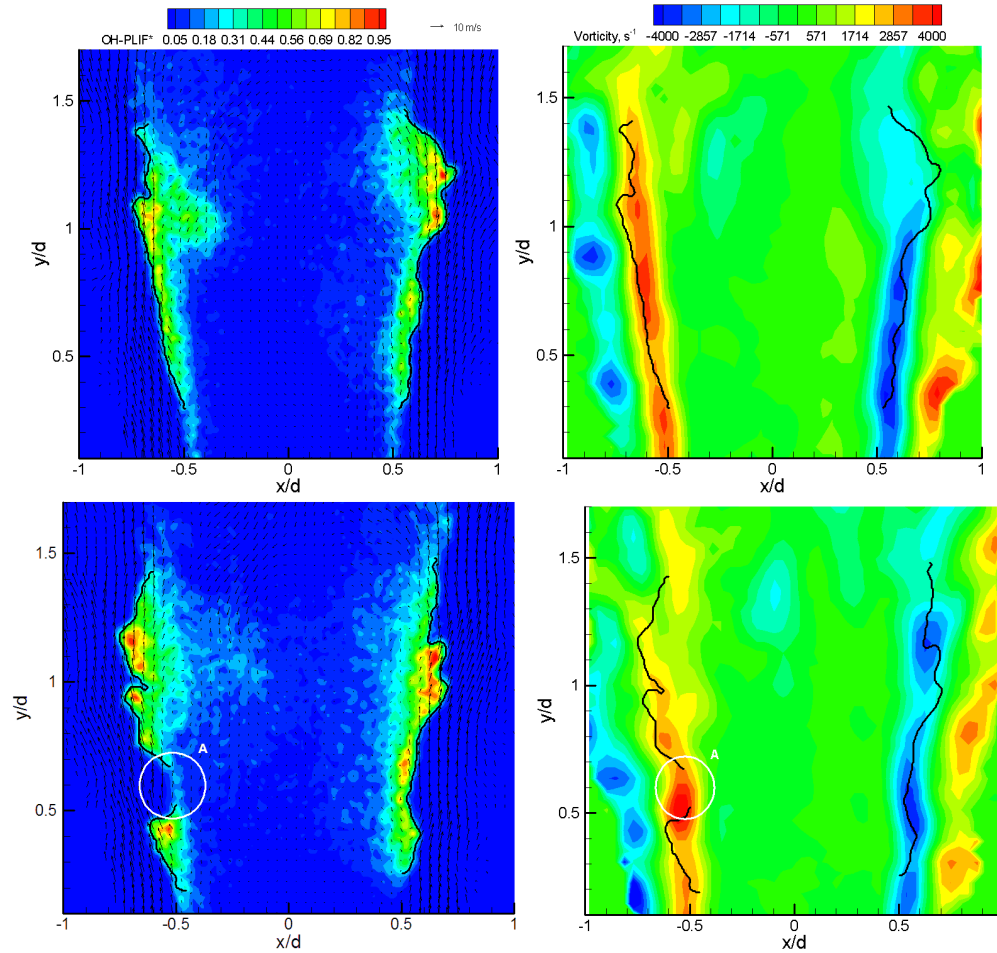
Figure 8-4 Typical instantaneous results of synchronized OH-PLIF and PIV for CH₄ flames at Φ=0.70. Left panel: normalized OH-PLIF intensity contour superimposed with PIV velocity vectors and detected flame fronts. Right panel: out-of-plane vorticity contour superimposed with flame fronts

Although the breaks of flame fronts detected can be simply interpreted as the flame itself is out of the 2-D measurement domain, the fact that majority of flame fronts are located in high vorticity regions implies the strong likelihood of flame experiencing

higher stretch rates induced by local intense vortices along the flame fronts, which will be discussed later in this paper.

To further examine the correlation between vortices and flame fronts, Figure 8-5a)-b) show the vorticity magnitude and OH-PLIF signal at y/d=1.0 f for flames at Φ=0.81 and 0.70, respectively. Comparing Figure 8-5a) and b), the peaks of vorticity magnitude and of OH-PLIF signal become closer to each other and therefore show more correlated as equivalence ratio is reduced.

a) Φ=0.81   b) Φ=0.70
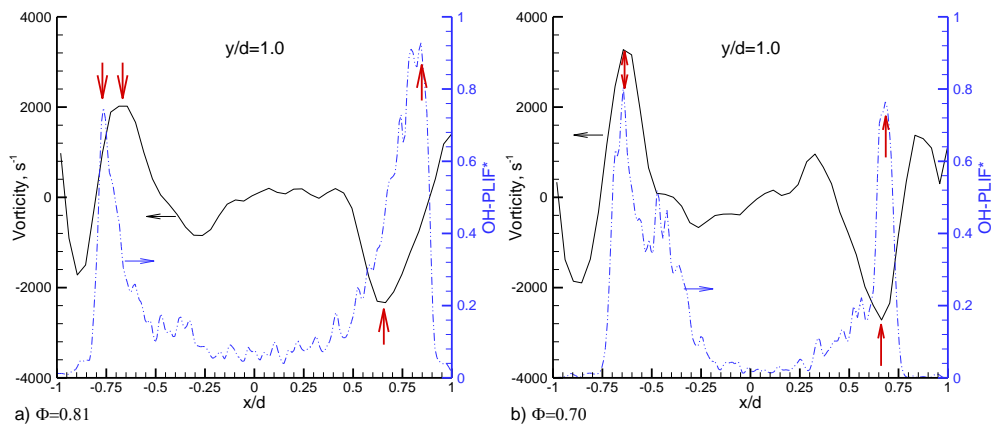
Figure 8-5 Instantaneous vorticity magnitude and PLIF intensity at y/d=1.0 for a) Φ=0.81 and b) Φ=0.70.
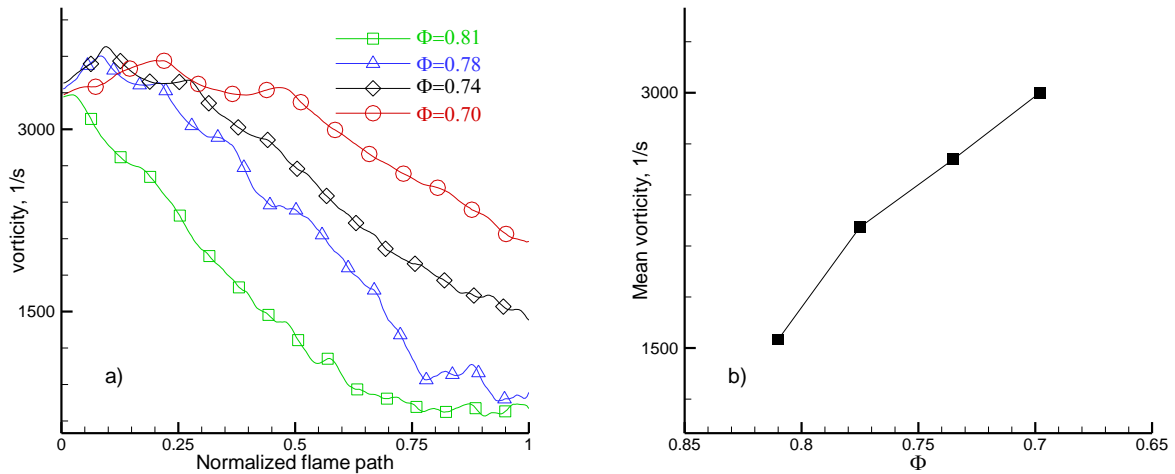
Figure 8-6 Vorticity along flame fronts.

Figure 8-6a) shows the mean vorticity along the normalized flame front. The mean vorticity map is first calculated from a set of 1000 PIV images. The time ensemble average flame front, defined as progress variable <c>=0.5 computed from the 500 OH-PLIF images, are then laid onto the mean vorticity map to interpolate the vorticity along flame fronts. Figure 8-6a) shows as equivalence ratio decreases, the local vorticity intensity increases relatively. In Figure 8-6b), the vorticity amplitudes are averaged over the entire flame fronts to obtain the representative vorticity for each case, and plotted with respect to equivalence ratio Φ. As Φ decreases from 0.81 to 0.70, vorticity increases up to about twice. This indicates that the vortex dynamics could play an important role in the flame LBO behavior. The further assessment of vortex flow effect in flame stretching or hydrodynamic stretch rate will be analyzed and discussed in next section.

8.3   Flame Stretch Rates

As equivalence ratio is reduced and flame is approaching LBO limit, the increase in correlation between strong vortices and flame fronts may indicate higher flame stretch rates along the flame fronts induced by higher strain or hydrodynamic stretch rates. For a given equivalence ratio, the fuel/air mixture has its stretch rate limit, or extinction stretch rate, in laminar flame. Theoretically flame stretch rates exceeding the limit will result in flame extinction. Thus, increase in flame stretch rates as flame approaches LBO limit could lead to excessive flame stretching, resulting in local flame extinction, as observed breaks along flame fronts. Therefore, the flame stretch rate is estimated here using detected flame fronts from OH-PLIF images and velocity field measured by PIV system.
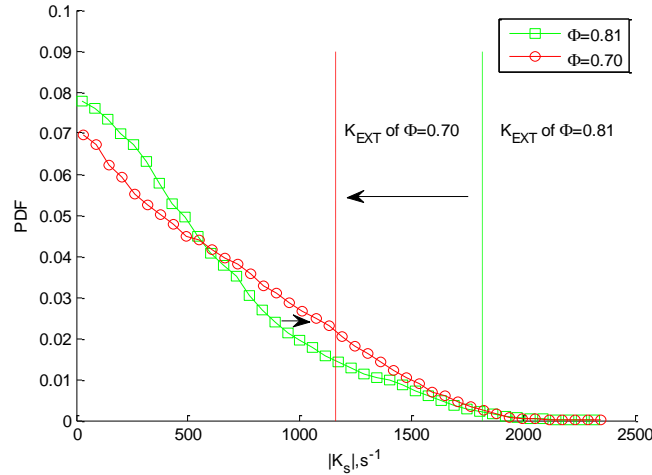
Figure 8-7 PDF distributions of hydrodynamic stretch rates.
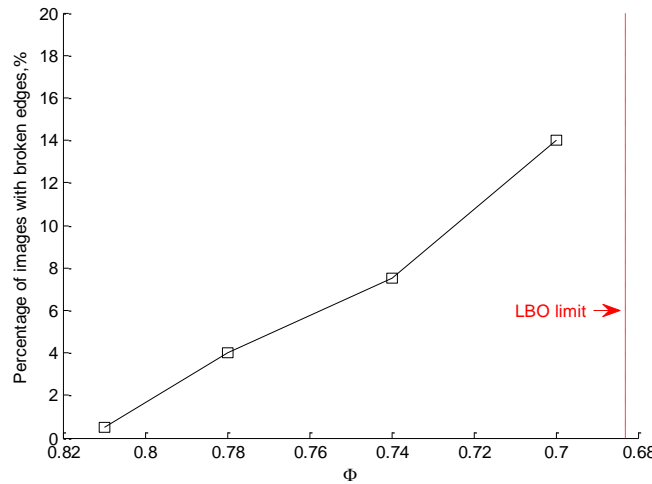
Figure 8-8 Percentage of OH-PLIF images with broken flame fronts.

In turbulence flame, there is a distribution of flame stretch rate, and the strain rate contribution is dormant. Bradley et al [102] suggests that for values of Karlovitz number Ka greater than 0.1 and of turbulent Reynolds number greater than 100, the PDF of stretch rate is similar to that of strain rate. So here, the flame curvature effect is no considered and only hydrodynamic stretch rate K_s is computed via PIV data and detected flame fronts from OH-PLIF images using[127]:

$$K_s = -n_x \times n_y \times \left(\frac{\partial u}{\partial y} + \frac{\partial v}{\partial x}\right) + (1 - n_x^2) \times \frac{\partial u}{\partial x} + (1 - n_y^2) \times \frac{\partial v}{\partial y}$$

Where n_x and n_y are the x and y components of the flame surface normal vector, and u and v are the radial and axial velocities.

Figure 8-7 shows the PDF distributions for calculated hydrodynamic stretch rates K_s for CH_4 flames. The dashed lines are corresponding flame-extinction strain rate values computed from opposite flow simulations for a premixed methane flame using CHEMKIN program with GRIMech3.0 reaction mechanisms. As equivalence ratio decreases from 0.81 to 0.70 and flame approaches LBO limits, the PDF distribution of K_s is shifted into higher value range, clearly indicated by the crossover at absolute K_s value about $600 s^{-1}$. In the other hand, the extinction strain rate is significantly reduced from 1800 to 1200 s^{-1}. It leads to higher possibility that flames experience too high stretch rate to sustain themselves, and as a result flames locally extinguish and breaks on flame sheets are expected. Figure 8-8 shows the percentage of OH-PLIF images with broken flame fronts observed based on 200 OH-PLIF images. At Φ=0.81, almost all flame fronts are connected. When Φ decreases to 0.70, about 14% of fluorescence images show broken flame sheets. It evidently shows the increase in the fraction of broken flame sheets as flames approach LBO limit.

8.4   Turbulence Intensity

The turbulent intensity can be defined as $U' = \sqrt{(u_{RMS}^2 + v_{RMS}^2 + w_{RMS}^2)/3}$ for a 3-D velocity field, where u_{RMS}, v_{RMS}, and w_{RMS} are the RMS velocity fluctuations in the axial, radial and tangential directions, respectively. Based on current 2-D PIV data, an estimate of turbulent intensity can be defined as $U' = \sqrt{(u_{RMS}^2 + 2 * v_{RMS}^2)/3}$, assuming

$v_{RMS}^2 = w_{RMS}^2$. With the time ensemble average flame front profile (<c>=0.5) from OH

fluorescence images and velocity field data from PIV, u_{RMS}, v_{RMS} and U' along the

average flame front are interpolated and plotted in Figure 8-9a)-c), respectively. The total

length of the flame front is used for normalization of flame path for each equivalence

ratio. From Figure 8-9a), u_{RMS} increases with a distance from burner dump plane due to

the turbulent transport of turbulences generated by high velocity gradients in the inner

shear layer and flames. As equivalence ratio decreases, u_{RMS} decreases overall. This is

explained by the fact that flames are stabilized in the inner shear layer between incident

swirling flow and internal recirculation zone and with inclination much closer to

horizontal or burner radial direction (compared to axial direction), thus the flame

introduced turbulence is more dominant in radial direction [128], as the similar

experimental observations as in open V-shaped flames[129,130]. So then decrease in

equivalence ratio reduces heat release rate, velocity jump across the flame fonts, and

therefore the flame generated turbulence, resulting in lower U_{RMS} in this swirl stabilized

burner. For v_{RMS} as shown in Figure 8-9b), however, it increases as equivalence ratio

decreases. This trend is actually associated with the flame front immigration into higher

turbulence regions. Figure 8-9a) and b) show line plots of velocity RMS and mean axial

velocity with respect to radial axis at y/d=0.75 for equivalence ratio 0.81 and 0.70,

respectively.   Axial velocity fluctuation v_{RMS} shows a local minimum coincidental with

maximum of mean axial velocity v_{mean}, and two local peaks distributed in two side of

maximum v_{mean}, that is, inner shear layer in left side and outer shear layer in right side.

Flames are stabilized in the inner shear layer as denoted by dashed lines. In Figure 8-10a)

of Φ=0.81, flames are close to the core of incident swirling flow where turbulent level is

relatively low. As equivalence ratio is reduced to 0.70 in Figure 8-10b), the decrease in flame burning speed leads to a reduction of flame inclination angle with respect to horizontal axis (flame shrinking), balancing the local flow velocity normal to flames and flame burning speed. Then flames shift into lower velocity regions and interact with the inner shear layer more intensely, and also progressively approach the local high turbulence peak in the inner shear layer. As a joining result of different behaviors of velocity fluctuations, the turbulent intensity along the flame front increases about 16% as equivalence ratio decreases from 0.81 to 0.70 as plotted in Figure 8-10c).
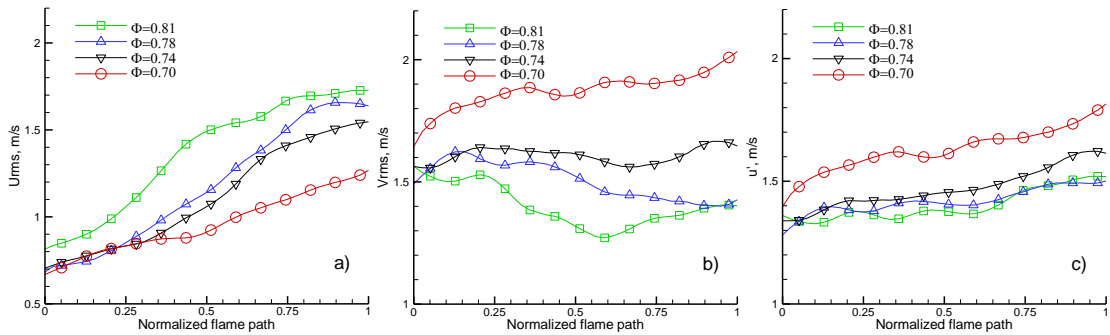
Figure 8-9 Turbulence intensities along flame fronts
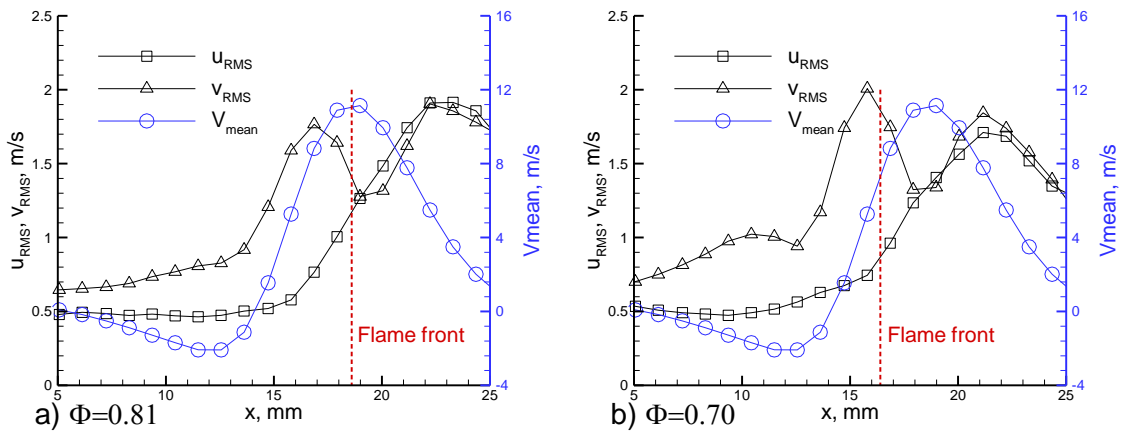
Figure 8-10 u_{RMS}, v_{RMS}, and v_{mean} at y/d=0.75 for a) Φ=0.81 and b)Φ=0.70. Dashed line denotes flame front location.

8.5 Local Da and Ka
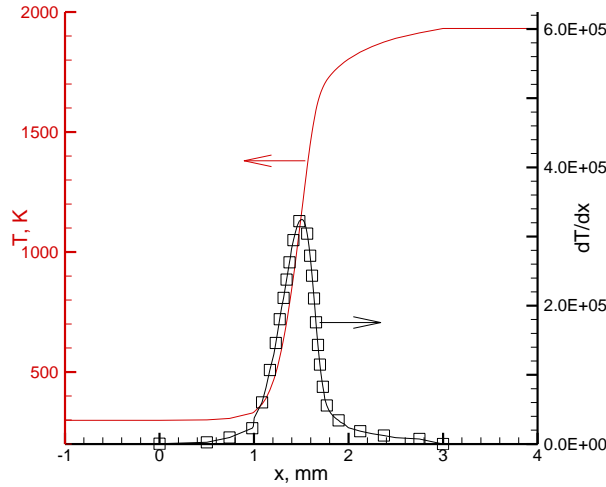
Figure 8-11 Temperature profile with its first derivative from CHEMKIN 1-D simulation for CH$_4$ flame at Φ=0.81.

The timescales related to chemical reaction and physical turbulence are often used to investigate the extinction of turbulent premixed flames. The most commonly used non-dimensional parameters are Damkohler number, Da, defined as the ratio of characteristic fluid time scale to chemical reaction time scale, and Karlovitz number, Ka, defined as the ratio of chemical time scale and smallest turbulent time scale. Here, these two parameters are calculated along the flame fronts using following formula [41]:

$$D_a = \frac{L_T}{\delta_L} \cdot \left(\frac{u'}{S_L}\right)^{-1}, \qquad K_a = \left(\frac{u'}{S_L}\right)^{1.5} \cdot \left(\frac{L_T}{\delta_L}\right)^{-0.5}$$

where L_T and u' are integral length scale and the turbulent intensity, and δ_L and S_L are the laminar flame thickness and speed. The laminar flame speeds were obtained by running 1-D free propagating flame simulation using CHEMKIN program with GRIMech3.0 reaction mechanisms. Figure 8-11 shows the corresponding temperature profile for the simulated methane flame at Φ=0.81. The first derivative of the temperature dT/dx is determined from the temperature profile. The laminar flame thickness is then defined as

106

$\delta_L=(T_b-T_u)/(dT/dx)_{max}$, where T_b and T_u are temperatures of burnt gas and unburnt gas, respectively.

For the integral length scale L_T along the flame fronts, it is evaluated using a two-point correlation of the axial turbulent velocity fluctuation and calculated as follows:

$$L_T = \int_0^\infty R_L(r)dr$$

$$R_L(r) = \frac{\overline{\Delta v(x) \cdot \Delta v(x+r)}}{v_{RMS}(x) \cdot v_{RMS}(x+r)}$$
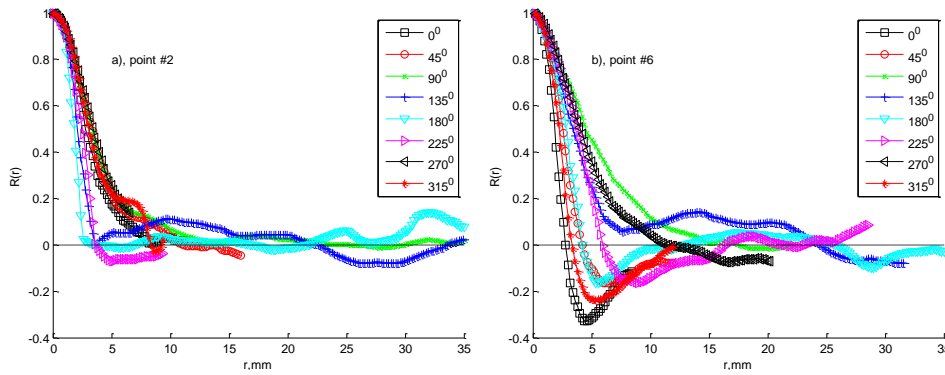
Figure 8-12 Two-point correlations of axial velocity fluctuations for flames at Φ=0.81
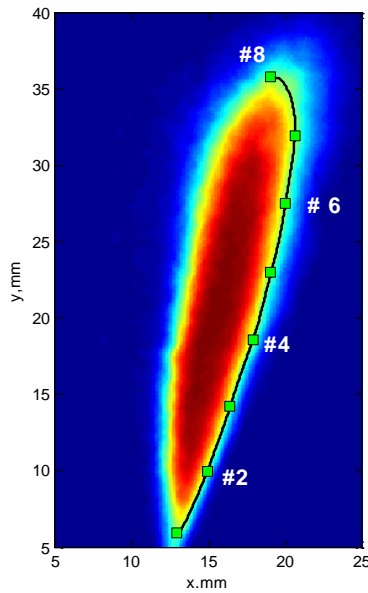
Figure 8-13 Progress variable <c> contour superimposed with flame front (<c>=0.5) for CH₄ flame at Φ=0.81(only RHS shown)

107

Since the flame is positioned in shear layer and the local turbulence is highly anisotropic, the anisotropy is considered when defining the local characteristic length scale. Here, the characteristic integral length scale at a point of interest along the flame front is computed by averaging those evaluated from eight different directions with 45^0 increments from the horizontal axis. Figure 8-12a)-b) show the two-point correlations of axial velocity fluctuations at two different positions along the flame front, as marked in Figure 8-13. From Figure 8-12, it is evident that the turbulent flow has different length scales in different directions. In the calculation of integral length scale at each direction, the corresponding correlation coefficient R(r) is integrated up to the first zero-crossing point. Then those integral length scales in different directions were averaged to represent the local characteristic length scale.
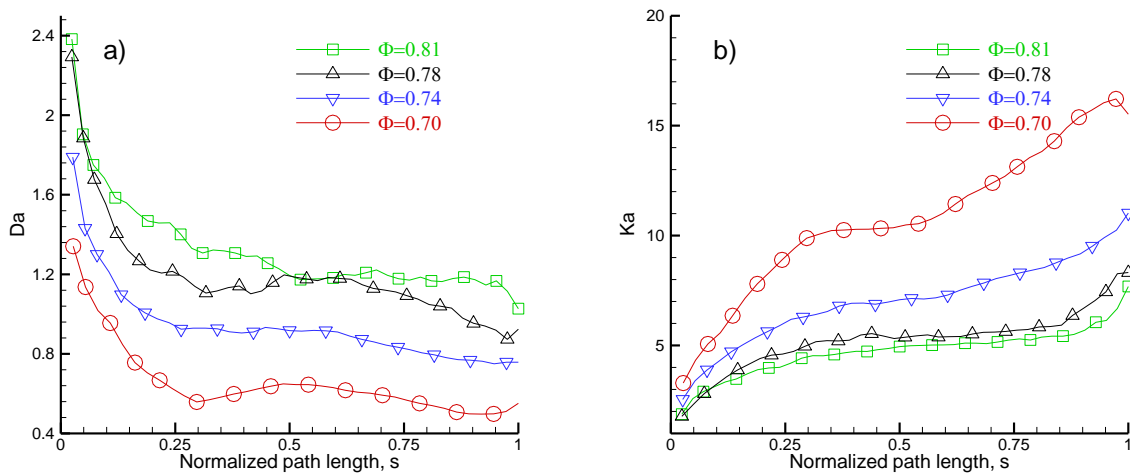
Figure 8-14 Local Da and Ka

With data of estimated turbulent intensities, laminar flame speeds and thicknesses, and characteristic length scales, Figure 8-14a) and b) show the local Damkohler number

Da and Karlovitz number Ka along the flame front for methane flames, respectively. The horizontal axis is the normalized flame path length. S=0 represents the end of flame front near dump plane, and s=1 for the flame tip in downstream. For each equivalence ratio, Da decreases and Ka increases with the distance from the burner dump plane. It indicates that susceptibility of flame extinction increases along flame path, and the last reaction survivor, if happening, would be most likely located near dump plane. This is in accordance with the OH-PLIF and high speed imaging at exactly LBO limits in our previous paper [125]. Moreover, as equivalence ratio decreases, the minimum and overall mean values of Da decreases, and Ka falls into the opposite trend to Da, with maximum and overall mean values of Ka increasing with distance from dump plane. It can be explained by the reduced laminar speed and the increased turbulence intensity as flame approaches LBO limits, as shown in Figure 8-9c). It implies the increase in flame stretch rate as flame approaches LBO limit, which therefore may be responsible for local flame extinction.

8.6   Effects of Hydrogen Addition

For hydrogen enriched flames, similar flame behaviors are observed as in methane flames. For example, as flame approaches LBO limit, flame fronts experience higher turbulence level, higher vorticity, and higher flame stretching rate and therefore have more breaks. As shown in Figure 8-15, the effect of hydrogen addition on these four parameters is non-linear, especially in mean stretch rate (absolute value) and fraction of broken flame sheets with 80% hydrogen blend. In fact, due to high molecular diffusivity associated with hydrogen content (Le<1), hydrogen flames are prone to be burning in

cellular structure- localized intense reactions and quenching. That is, unlike methane flames, flame stretching (positive curvature) with hydrogen fuel even promotes localized enrichment of fuel and therefore reaction to some extent. From Figure 8-15d), this phenomenon is not significant until hydrogen level blended is greater than 60%.
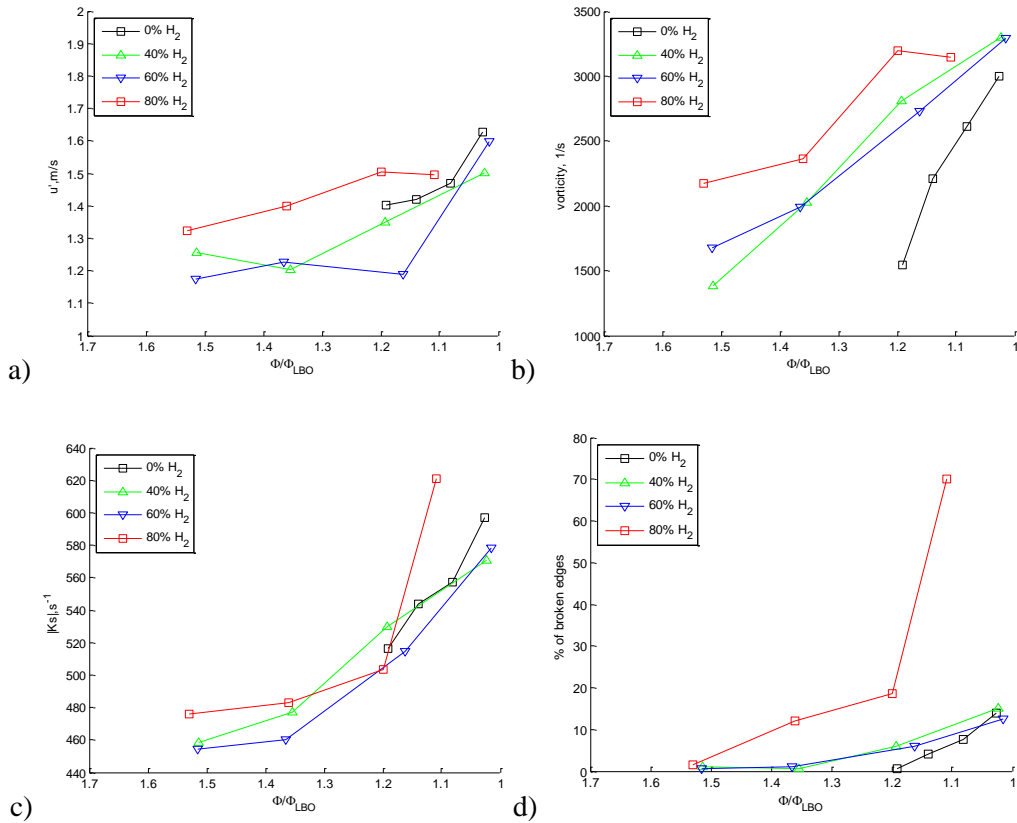
Figure 8-15 Hydrogen effects on a) mean turbulent intensity, b) mean vorticity, c) mean stretch rate(|Ks|), and d) percentage of broken flame sheets

8.7   Conclusions

In this study, synchronized PIV and OH-PLIF has been performed for four different equivalence ratios for methane flames in a swirl-stabilized burner. OH fluorescence images have been used to determine the flame front via an image intensity threshold technique. Results presented include the flow-flame interaction, vorticity along flame fronts, estimates of turbulent anisotropy, local Damkohler number and Karlovitz

number, and hydrodynamic strain rates. The following are the main conclusions of this study:

1. For a stable flame, the flame front is winkled but connected, and located in regions of low vorticity. As equivalence ratio decreases, the flame front breaks appear more and more frequent, majority of flame fronts are overlapping strong vortices. From equivalence ratio 0.81 to 0.70, the average vorticity increases about 100%.

2. In four tested lean conditions, flames are all stabilized in the inner shear layer between incident swirling flow and internal circulation zone. The normal of flame brush is more inclined to horizontal axis and therefore flame-generated turbulence is dominant in that direction. Thus the horizontal velocity fluctuation deceases as equivalence ratio decreases. However the escalated interaction between flame fronts and shear layer caused by reduced flame burning speed increases the turbulent intensities along the flame front overall. The mean turbulence intensity increases about 16% as equivalence ratio decreases from 0.81 to 0.70.

3. As equivalence ratio decreases, the flame extinction strain rate is reduced, while the PDF distribution of hydrodynamic stretch rate shifts toward higher value. This inverse trend is believed to result in local flame extinction and flame front breaks, as indicated by increased fraction of broken flame sheets.

4. Along the flame front starting from dump plane, the calculation shows Damkohler number decreases, while Karlovitz number increases. The decrease in equivalence ratio leads to decrease in Damkohler number and increase in Karlovitz number. It implies the increased susceptibility of flame local extinction along the flame path.

5. For tested three hydrogen blend levels of 40%, 60%, and 80%, hydrogen effect is not significant in term of turbulence intensity, vorticity, stretch rate and broken flame edges until 80% hydrogen present.

CHAPTER 9 : SUMMARY AND OUTLOOK

9.1 Summary and Conclusions

In this study, swirl-stabilized dump premixed flames have been investigated experimentally for different Reynolds numbers and different hydrogen levels. Simultaneous measurements of PIV and OH*/CH* Chemiluminescence, high speed imaging, and PIV and OH-PLIF images have been conducted to investigate the flow field, reaction zone, heat release, flame structure properties, and flow-flame interaction as equivalence ratio decreases and hydrogen addition increases. For high speed imaging of flames at LBO limits, both unconfined and confined flames are studied.

In unconfined flames, as equivalence ratio decreases, the flame orientation angle between flames and dump plane increases due to reduced flame speed, leading to flame receding toward IRZ. Then the correlation between flame fronts and flow strong vorticity is increased. The flame edges experience higher hydrodynamic stretch rate, resulting in higher flame local extinction, and breaks along the flame fronts. Those breaks, in turn, entrain the unburnt fuel air mixture into IRZ passing through the shear layer, further leading to reaction taking place within IRZ. In the flow field, the width of IRZ in methane-only flames decreases. It causes the methane flame to straddle the boundary of the IRZ with the outer half of the methane flame in the high-turbulence shear layer region, resulting in a very unstable flame. High speed imaging shows that periodic flame rotating with extinction and re-light events are evident. This results in high RMS of heat release rate, and therefore a shorter extinction time scale. With hydrogen addition, flames remain in relatively axisymmetric burning structure and stable with the aid of low minimum ignition energy and high molecular diffusivity associated with hydrogen.

Additionally, the opposite advancing between reaction zone (moving toward IRZ) and IRZ (expanding outward) also leads to the flame region to be further within IRZ with a relatively favorable combustion environment. High speed flame imaging shows hydrogen enriched flame is relatively symmetric and stable, even right before flame entering extinction transition at LBO limit equivalence ratio, leading to lower heat release fluctuation and a longer extinction time scale.

For confined flames, however, the hydrogen effect on the extinction transient is completely opposite due to spiraling columnar burning structure, in comparison of a relatively stable conical shape in methane flames.

Additionally, hydrogen addition evidently lowers the LBO limit, and for a given fuel composition, confined flames can burn at even leaner conditions compared to unconfined flames. Calculation based on adiabatic flame temperature and heat release rates shows hydrogen addition also increases the heat retention.

High speed flame imaging in all tested confined and unconfined flames, the final extinction occurs shortly after the reaction zone immediately above the center-body fails, indicating a significant effect of this flame root on the final extinction. It is suggested that the ability to better sustain this flame root might extend the LBO limit to leaner conditions.

9.2 Recommendations for Future Work

High speed imaging in confined flames shows strong correlation between elevated boundary temperature and flame extinction transition time scales. In fact, there are two distinct extinction limits for laminar premixed flames: a radiation (heat loss) extinction

limits and a stretch extinction limit. It suggests that the boundary temperature effect on the LBO process. Detailed investigation on the contribution from this factor would provide more insights into the flame extinction mechanisms.

Better understanding of the vortex breakdown and its transition between different modes in reacting flow especially in low flow dilation is needed to explain the flame behavior when it is approaching LBO limit. In swirling flow, it is the vortex breakdown induced recirculation zone that provides the flame holding.

The key challenge is still the understanding of what ultimately leads to the blowout. Then, the time-resolved measurements of flow field and flame structure very near LBO limit are very important and critical.

In addition, the pressure affect on LBO is of practical importance. As is well known, most of turbine engines are operated on high pressure and high temperature condition. And conclusions and techniques on normal pressure and temperature may not be directly applied onto those cases.

REFERENCES

[1] D. Littlejohn, R.K. Cheng, "*Fuel Effects on a Low-Swirl Injector for Lean Premixed Gas Turbines*," Proc.Combust.Inst., 31 (2007), pp. 3155–3162.

[2] M. B. Hilt and J. Waslo, "*Evolution of NOx Abatement Techniques through Combustor Design for Heavy-Duty Gas Turbines*," Journal of Engineering for Gas Turbines and Power, 106(1984), pp. 626.

[3] W. S. Y Hung, "The *Reduction of NOx Emissions from Industrial Gas Turbines*," The Eleventh International Congress on Combustion Engines, 3(1975), pp. 161-181.

[4] A. H. Lefebvre, Gas Turbine Combustion, Taylor & Francis, Philadelphia, 1998.

[5] Toshio Shudo, Kento Omori, and Osamu Hiyama, "*NOx Reduction and NO$_2$ Emission Characteristics in Rich-Lean Combustion of Hydrogen*," International Journal of Hydrogen Energy, 32(2008), pp. 4689-4693.

[6] Vivek K. Khanna, A Study of the Dynamics of Laminar and Turbulent Fully and Partially Premixed Flames, Dissertation, Virginia Tech, 2001.

[7] C.K. Westbrook, and F. L. Dryer, "*Chemical Kinetic Modeling of Hydrocarbon Combustion*," Progress in Energy and Combustion Science, 10(1984), pp. 1-57.

[8] V. L. Zimont, "*The Theory of Turbulent Combustion at High Reynolds Numbers*," Combustion Explosions and Shock Waves, 15(1979), pp. 305-311.

[9] S. Nair, Acoustic Characterization of Flame Blowout Phenomenon, Ph.D. Thesis, Georgia Institute of Technology, Georgia, USA, 2006.

[10] Y. C. Chao, Y. L. Chang, C. Y. Wu and T. S. Cheng, "*An Experimental Investigation of the Blowout Process of a Jet Flame*," Proc. Comb. Inst., 28(2000), pp. 335-342.

[11] H. Nicholson and J. Field, "*Some Experimental Techniques for the Investigation of Mechanism of Flame Stabilization in the Wakes of Bluff Bodies*," Proc. Comb. Inst., 3(1951), pp. 44-68.

[12] S. R. N. De Zilwa, J. H. Uhm and J. H. Whitelaw, "*Combustion Oscillations Close to the Lean Flammability Limit*," Combust. Sci. Technol., 160(2000), pp. 231-258.

[13] T. M. Muruganandam, S. Nair, Y. Neumeier, T. Lieuwen and J. M. Seitzman, "*Optical and Acoustic Sensing of Lean Blowout Precursors*," 38th AIAA/ASME/SAE/ASEE Joint Propulsion Conference & Exhibit, Indianapolis, Indiana, 2002, AIAA Paper No. 2002-3732.

[14] S. Nair and T. Lieuwen, "*Acoustic Detection of Blowout in Premixed Flames*," J. Prop. Power, 21 (2005), pp. 32–39.

[15] M. Thiruchengode, S. Nair, S. Prakash, D. Scarborough, Y. Neumeier, T. Lieuwen, J. Jagoda, J. Seitzman and B. Zinn, "*An Active Control System for LBO Margin Reduction in Turbine Engines*," 41st AIAA Aerospace Sciences Meeting and Exhibit, Reno, Nevada, 2003, AIAA Paper No. 2003–1008.

[16] E. E. Zukoski and F. E. Marble, "*Experiments Concerning the Mechanism of Flame Blowoff from Bluff Bodies*," Proceedings of the Gas Dynamics Symposium on Aerothermochemistry, 1956, pp. 205-210.

[17] E. E. Zukoski and F. E. Marble, "*The Role of Wake Transition in the Process of Flame Stabilization on Bluff Bodies*," AGARD Combustion Researches and Reviews, 1955, pp. 167-180.

[18] C. R. King, "*Experimental Investigation of Effects of Combustion Chamber Length and Inlet Total Temperature, Total pressure, and Velocity on Afterburner Performance*," NACA RM E57C07, 1957.

[19] H. C. Hottel, G. C. Williams, W. P. Jensen, A. C. Tobey and M. R. Burrage, "*Modeling Studies of Baffle-type Combustors*," Ninth Symposium (International) on Combustion, 9(1), 1963, pp. 923-935.

[20] I. Glassman, Combustion, Academic Press, New York, 1996.

[21] D. R. Noble, Q. Zhang, A. Shareef, J. Tootle, A. Meyers and T. Lieuwen, "*Syngas Mixture Composition Effects upon Flashback and Blowout*," Proceedings of ASME Turbo Expo, Barcelona, Spain, 2006, ASME Paper No. GT2006-90470.

[22] H. Li, X. Zhou, J. B. Jeffries and R. K. Hanson, "*Active Control of Lean Blowout in a Swirl-Stabilized Combustor Using a Tunable Diode Laser*," Proc. Combust. Inst., 31(2007), pp. 3215-3223.

[23] E. Gutmark, T. P. Parr, D. M. Hanson-Parr and K. C. Schadow, "*Use of Chemiluminescence and Neural Networks in Active Combustion Control*," Proc. Combust. Inst., 23(1990), pp. 1101–1106.

[24] G. J. Sturgess, S. P. Heneghan, M. D. Vangsness, D. R. Ballal, A. L. Lesmerises and D. Shouse, "*Effects of Back-Pressure in a Lean Blowout Research Combustor*," J. Eng. Gas Turbines Power, 115(1993), pp. 486–498.

[25] M. D. Durbin and D. R. Ballal, "*Studies of Lean Blowout in a Step Swirl Combustor*," J. Eng. Gas Turbines Power, 118(1996), pp. 72–77.

[26] J. P. Longwell, "*Flame Stabilization by Bluff Bodies and Turbulent Flames in Ducts*," Proc. Combust. Inst., 4(1953), pp. 90–97.

[27] F. A. Williams, "*Flame Stabilization of Premixed Turbulent Gases*," Applied Mechanics Surveys, 1966, pp. 1157–1170.

[28] G. C. Williams, H. C. Hottel and A. C. Scurlock, "*Flame Stabilization and Propagation in High Velocity Gas Streams*," Proc. Combust. Inst., 1951, pp. 21–40.

[29] K. M. Kundu, D. Banerjee and D. Bhaduri, "*On Flame Stabilization by Bluff-Bodies*," Journal of Engineering for Power, 1980, pp. 209–214.

[30] K. M. Kundu, D. Banerjee and D. Bhaduri, "*Theoretical Analysis on Flame Stabilization by a Bluff-Body*," Combust. Sci. Technol., 1977, pp. 153–162.

[31] E. E. Zukoski, "*Flame Stabilization on Bluff Bodies at Low and Intermediate Reynolds Numbers*," Ph.D. Thesis, California Institute of Technology, Pasadena, California, 1954.

[32] D. B. Spalding, "*Theoretical Aspects of Flame Stabilization*," Aircraft Engineering, 25(1953), pp. 264–276.

[33] E. E. Zukoski, "Afterburners," in: Aero-thermodynamics of Gas Turbine and Rocket Propulsion, G. C. Oates, Eds, 1997.

[34] S. Yamaguchi, N. Ohiwa and T. Hasegawa, "*Structure and Blow-Off Mechanism of Rod-Stabilized Premixed Flame*," Combust. Flame., 62(1985), pp. 31-41.

[35] J. C. Pan, M. D. Vangsness and D. R. Ballal, "*Aerodynamics of Bluff-Body Stabilized Confined Turbulent Premixed Flames*," J. Eng. Gas Turbines Power, 1992, pp. 783-789.

[36] S. Chaudhuri, S. Kostka, M. W. Renfro and B. M. Cetegen, "*Blowoff Dynamics of Bluff Body Stabilized Turbulent Premixed Flames*," Combust. Flame., 157(2010), pp. 790–802.

[37] S. Shanbhogue, S. Husain and T. Lieuwen, "*Lean Blowoff of Bluff Body Stabilized Flames: Scaling and Dynamics*," Prog. Energy Combust. Sci., 35(2009), pp. 98–120.

[38] Q. Zhang, D. R. Noble, S. J. Shanbhogue and T. Lieuwen, "*Impacts of Hydrogen Addition on Near-Lean Blowout Dynamics in a Swirling Combustor*," *Proceedings of ASME Turbo Expo*, Montreal, Canada, 2007, ASME Paper No. GT2007-27308.

[39] M. Füri, P. Papas and P. A. Monkewitz, "*Non-premixed Jet Flame Pulsations Near Extinction*," Proc. Combust. Inst., 28(2000), pp. 831–838.

[40] E. W. Christiansen, C. K. Law and C. J. Sung, "*The Role of Pulsating Instability and Global Lewis Number on the Flammability Limit of Lean Heptane/Air Flames*," Proc. Combust. Inst., 29(2000), pp. 807–814.

[41] N. Peters, "*Laminar Flamelet Concepts in Turbulent Combustion*," Proc. Combust. Inst., 21(1986), pp. 1231-1250.

[42] J. F. Driscoll, "*Turbulent Premixed Combustion: Flamelet Structure and its Efect on Trubulent Burning Velocities*," Progress in Energy and Combust Science, 34(1) (2008), pp. 91-134.

[43] A. L. Birbaud, D. Durox, S. Ducruix and S. Candel1, "*Dynamics of Confined Premixed Flames Submitted to Upstream Acoustic Modulations*," Proc. Combust. Inst., 31(1) (2007), pp. 1257-1265.

[44] D. Durox, T. Schuller and S. Candel, "*Combustion Dynamics of Inverted Convical Flames*," Proc. Combust. Inst., 30(2005), pp. 1717–1724.

[45] C. Kulsheimer and H. Buchner, "*Combustion Dynamics of Turbulent Swirling Flames*," Combust. Flame, 131(2002), pp. 70–84.

[46] S. S. Archer, Morphology of Unconfined and Confined Swirling Flow Under Non-reacting and Combustion Conditions, Dissertation, University of Maryland, 2005.

[47] E. R. Hawkes and J. H. Chen, "*Direct Numerical Simulation of Hydrogen-Enriched Lean Premixed Methane Air Flames*," Combust. Flame, 138(2004), pp. 242–258.

[48] A. R. Choundhuri and S. R. Gollahalli, "*Combustion Characteristics of Hydrogen–Hydrocarbon Hybrid Fuels*," Hydrogen Energy, 25(2000), pp. 451–462.

[49] A. R. Choundhuri and S. R. Gollahalli, "*Characteristics of Hydrogen–Hydrocarbon Composite Fuel Turbulent Jet Flame*," Hydrogen Energy, 28(2003), pp. 445–454.

[50] G. A. Karim, I. Wierzba and Y. Al-Alousi, "*Methane–Hydrogen Mixture as Fuels*," Hydrogen Energy, 21(1996), pp. 625–631.

[51] S. R. Turns, An Introduction to Combustion: Concepts and Applications, 2nd Edition, McGraw Hill, Columbus, Ohio, 2000.

[52] O. Tuncer, S. Acharya and J. H. Uhm, "*Effects of Hydrogen Enrichment on Confined Methane Flame Behavior*," Proceedings of ASME Power 2006, Atlanta, Georgia, ASME Paper No: PWR2006-88079.

[53] M. Braun-Unkhoff, T. Kick, P. Frank and M. Aigner, "*An Investigation on Laminar Flame Speed as Part of Needed Combustion Characteristics of Biomass-Based Syngas Fuels*," Proceedings of GT2007, ASME Turbo Expo: GT2007-27479.

[54] A. Gaydon, The Spectroscopy of Flames, 2nd Ed. Chapman and Hall, London, 1974.

[55] A. J. Marchese, F. L. Dryer, V. Nayagam and R. O. Colantonio, "*Hydroxyl Radical Chemiluminescence Imaging and the Structure of Microgravity Droplet Flames*," Proc. Combust. Inst., 26(1996), pp. 1219–1226.

[56] M. D. Smooke, Y. Xu, R. M. Zurn, P. Lin, J. H. Frank and M. B. Long, "*Computational and Experimental Study of OH and CH Radicals in Axisymmetric Laminar Diffusion Flames*," Proc. Combust. Inst., 24 (1992), pp. 813–821.

[57] C. J. Lawn, "*Distributions of Instantaneous Heat Release by the Cross-Correlation of Chemiluminescent Emissions*," Combustion and Flame, 123 (2000), pp. 227–240.

[58] L. C. Haber and U. Vandsburger, "*A Global Reaction Model for OH* Chemiluminescence Applied to a Laminar Flat-Flame Burner*," Combust. Sci. Technol., 175 (2003), pp. 1859–1891.

[59] J.M. Samaniego and T. Mantel, "*Fundamental Mechanisms in Premixed Turbulent Flame Propagation via Flame–Vortex Interactions: Part I: Experiment*," Combustion and Flame, 118 (1999), pp. 537–556.

[60] I.R. Hurle, R.B. Price, T.M. Sugden and A. Thomas, "*Sound Emission from Open Turbulent Premixed Flames*," Proc. R. Soc. London A, 303(1968), pp. 409–427.

[61] Y. Hardalupas and M. Orain, "*Local Measurements of the Time-Dependent Heat Release Rate and Equivalence Ratio Using Chemiluminescent Emission from a Flame*," Comb. Flame, 139(2004), pp. 188-207.

[62] J. F. Griffith and J. A. Barnard, Flame and Combustion, Blackie Academic, London, 1995.

[63] V. Bychkov, "Velocity *of Turbulent Flamelets with Realistic Fuel Expansion*," Phys. Rev. Letters, V84, N26(2000), pp. 6122-6125.

[64] M. Zaytsev and V. Bychkov, "*Effect of the Darrieus-Landau Instability on Turbulent Flame Velocity*," Physical Review, E66, 026310 (2002).

[65] G. Darrieus, Propagation d'un front de flamme, presented at La Technique Moderne (Paris) and in 1945 at Congre`s de Me ćanique Applique é, Paris,1938 (unpublished work).

[66] L. D. Landau, "*On the Theory of Slow Combustion*," Acta Physicochim, USSR 19 (1944), pp. 77–85.

[67] M. Matalon, "*Flame Dynamics*," Proc. Comb. Inst., 32(2009), pp. 57-82.

[68] R. Weber, F. Boysan, J. Switchenbank and P. A. Robers, "*Computation of Near Field Acrodynamcis of Swirling Expanding Flows*," 21st International Symposium on Combustion, 1988, pp. 1435-1443.

[69] A. K. Gupta, D. G. Lilley and N. Syred, Swirl Flows, Abacus Press, London, 1984.

[70] J. M. Beer and N. A. Chigier, Combustion Aerodynamics, Krieger Publishing Company, 1983.

[71] T. Sarpkaya, "*On Stationary and Travelling Vortex Breakdowns*," J Fluid Mech 45 (1971), pp. 545-559.

[72] S. Leibovich, "*The Structure of Vortex Breakdown*," Annual Review of Fluid Mechanics, 1978, pp. 221-246.

[73] S. Leibovich, "*Vortex Stability and Breakdown: Survey and Extension*," AIAA Journal, 22(1984), pp. 1192-1206.

[74] Y. Huang and V. Yang, "*Dynamics and Stability of Lean-Premixed Swirl-Stabilized Combustion*," Progress in Energy and Combustion Science, 35(2009), pp. 293–364.

[75] J. H. Faler and S. Leibovich, "*Disrupted States of Vortex Flow and Vortex Breakdown*," Phys. Fluids, 20(1977), pp. 1385-1400.

[76] M. P. Escudier and N. Zehnder, "*Vortex-Flow Regimes*," Journal of Fluid Mechanics, 115(1982), pp. 105-121.

[77] Ch. Briicker, "*Study of Vortex Breakdown by Particle Tracking Velocimetry. Part2: Spiral-Type Vortex Breakdown*," Experiments in Fluids, 14(1993), pp. 133-139.

[78] S. I. Shtork, N. F. Vieira and E. C. Fernandes, "*On the Identification of Helical Instabilities in a Reacting Swirling Flow*," Fuel, 87(2008), pp. 2314-2321.

[79] D. Froud, T. O'Doherty and N. Syred, "*Phase Averaging of the Precessing Vortex Core in a Swirl Burner under Piloted and Premixed Combustion Conditions*," Combustion and Flame, 100(1995), pp. 407–412.

[80] N. Syred, W. Fick, T. O'Doherty and A. J. Griffiths, "*The Effect of the Precessing Vortex Core on Combustion in a Swirl Burner*," Combustion Science and Technology, 125(1997), pp. 139–157.

[81] P. M. Anacleto, E. C. Fernandes, M. V. Heitor and S. I. Shtork, "*Swirl Flow Structure and Flame Characteristics in a Model Lean Premixed Combustor,*" Combustion Science and Technology, 175(2003), pp. 1369–1388.

[82] T. Sarpkaya, "*Vortex Breakdown in Swirling Conical Flows,*" AIAA J., 9(1971), pp. 1792-1799.

[83] J. P. Narain, "*Numerical Prediction of Confined Swirling Jets,*" Computers and Fluids, 5(1977), pp. 115-125.

[84] A. Melling, "*Tracer Particles and Seeding for Particle Image Velocimetry,*" Meas. Sci. Technol., 8(1997), pp. 1406-1416.

[85] L. M. Lourenco and A. Krothapalli, "*True Resolution PIV: a Mesh-Free Second Order Accurate Algorithm,*" Proceeding of the International Conference on Applications of Laser Fluid Mechanics, Lisbon, 2000, pp. 10-13.

[86] J. Westerweel, Digital Particle Image Velocimetry-theory and application, Delft University Press, 1993.

[87] N. L. Garland and D. R. Crosley, " *Energy Transfer Processes in CH $A^2\Delta$ and $B^2\Sigma$ in an Atmospheric Pressure Flame,*" Application Optics., 24(1985), pp. 4229-4237.

[88] H. P. Dorn, R. Neuroth and A. Hofzumhaus, "*Investigation of OH Absorption Cross Sections of Rotational Transitions in the $A2\Sigma$, $v=0 \leftarrow X^2II$, $v''=0$ Band under Atmospheric Conditions: Implications for Tropospheric Long-Path Absorption Measurements,*" Journal of Geophysical Research, 100(1995), pp. 7397-7409.

[89] K. K. Hoingghaus, "*Laser Techniques for the Quantitative Detection of Reactive Intermediates in Combustion Systems,*" Progress in Energy and Combustion Science, 20(1994), pp. 203-279.

[90] J. B. Kelman and A. R. Masri, "*Simultaneous Imaging of Temperature and OH Number Density in Turbulent Diffusion Flames,*" Combustion Science and Technology, 122(1997), pp. 1-32.

[91] T. G. Chasteen, http://www.files.chem.vt.edu/chem-ed/quantum/jablonsk.html

[92] V. Santhanam, OH PLIF Imaging of Swirl Stabilized Combustor, LSU, 1998.

[93] H. Becker, P. B. Monkhouse, J. Wolfrum, R. S. Cant, K. N. C. Bray, R. Maly, W. Pfister, G. Stahl and J. Warnatz, "*Investigation of Extinction in Unsteady Flames by 2-D LIF of OH Radicals and Flamelet Analysis,*" Twenty-Third Symposium (International) on Combustion, 1990, pp. 817-823.

[94] G. H. Dieke and H. M. Crosswhite, "*The Ultraviolet Bands of OH Fundamental Data*," J. Quant. Spectrosc. Radiat. Transfer, 2(1961), pp. 97-199.

[95] M. J. Dyer and D. R. Crosley, "*Fluorescence Imaging for Flame Chemistry*," Proc. Int. Conf. Laser, 84(1985), pp. 211-218.

[96] R. K. Hanson, "*Combustion Diagnostics: Planar Flow Field Imaging*," Proc. Combust. Inst., 21(1986), pp. 1677-1691.

[97] L. Muniz and M. G. Mungal, "*Instantaneous Flame-Stabilization Velocities in Lifted-Jet Diffusion Flames*," Combustion and Flame, 111(1997), pp. 16-31.

[98] S. Tachibana, L. Zimmer and K. Suzuki, "*Flame front detection and dynamics using PIV in a turbulent premixed flame*," Applications of Laser Techniques to Fluid Mechanics, 2004.

[99] A. Soika, F. Dinkelacker and A. Leipertz, "*Pressure Influence on the Flame Front Curvature of Turbulent Premixed Flames: Comparison between Experiment and Theory*," Combust. Flame, 132(2003), pp. 451-462.

[100] I. G. Shepherd, "*Flame Surface Density and Burning Rate in Premixed Turbulent Flames*," Twenty-sixth Symposium (International) on Combustion/The Combustion Institute, 1996, pp. 373-379.

[101] S. H. Sung and C. K. Law, "*An Invariant Derivation of Flame Stretch*," Combust. Flame., 55 (1984), pp.123–125.

[102] D. Bradley, P. H. Gasell, A. Sedaghat and X. J. Gu, "*Generatation of PDFS for Flame Curvature and for Flame Stretch Rate in Premixed Turbulent Combustion*," Combust. Flame, 135(2003), pp. 503-523.

[103] O. H. Nestor and H. N. Olsen, "*Numerical Methods for Reducing Line and Surface Probe Data*," SIAM Rev. 2(1960), pp. 200–207.

[104] M. W. Blades and G. Horlick, "*Photodiode Array Measurement System for Implementing Abel Inversions on Emission from an Inductively Coupled Plasma*," Appl. Spectrosc., 34(6) (1980), pp. 696–699.

[105] U. Engel, C. Prokisch, E. Voges, G. M. Hieftje and J. A. C. Broekaert, "*Spatially Resolved Measurements and Plasma Tomography with Respect to the Rotational Temperatures for a Microwave Plasma Torch*," J. Anal. At. Spectrom., 13(1998), pp. 955–961.

[106] L. Sirovich, Q. Appl. Math. XLV(3), 1987, pp.561-571.

[107] D. Caver, and K.E. Meyer, "*LES of Turbulent Jet in Cross Flow: Part 2- POD Analysis and Identification of Coherent Structures*," International Journal of Heat and Fluid Flow, 36(2012), pp.35-46.

[108] K. M. Kopp-Vaughan, T.R. Jensen, B.M. Cetegen, and M.W. Renfro, , "*Analysis of Blowoff Dynamics from Flames with Stratified Fueling*," Proc.Combust. Inst., 2012. http://dx.doi.org/10.1011/j.proci.2012.06.074

[109] N. Syned, A. K. Gupta and J. M. Beer, "*Temperature and Density Gradients Arising with the Precessing Vortex Core and Vortex Breakdown in Swirl Burners*," Proceedings of the 15th international symposium on combustion, 1975, pp. 587-597.

[110] O. H. Nestor and H. N. Olsen, "*Numerical Methods for Reducing Line and Surface Probe Data*," SIAM Review, 2(3) (1960), pp. 200-207.

[111] M. W. Blades and G. Horlick, "*Photodiode Array Measurement System for Implementing Abel Inversions on Emission From an Inductively Coupled Plasma*," Appl. Spectrosc., 34(6) (1980), pp. 696-699.

[112] U. Engel, C. Prokisch, E. Voges, G. M. Hieftje and J. A. C. Broekaert, "*Spatially Resolved Measurements and Plasma Tomography with Respect to the Rotational Temperatures for a Microwave Plasma Torch*," J. Anal. At. Spectrom., 13(1998), pp. 955-961.

[113] R. S. Barlow, R. W. Dibble, J. Y. Chen and R. P. Lucht, "*Effect of Damkohler Number on Superequilibrium OH Concentration in Turbulent Nonpremixed Jet Flames*," Combust. Flame, 82(3-4) (1990), pp. 235-251.

[114] N. Peters, Turbulent Combustion, Cambridge Univ. Press, Cambridge, UK, 2000.

[115] P. Kalt, J. Frank and R. W. Bilger, "*Laser Imaging of Conditional Velocities in Premixed Propane-Air Fames by Simultaneous OH PLIF and PIV*," Proc. Combust. Inst., 27(1) (1998), pp. 751-758.

[116] A. M. Steinberg, I. Boxx, M. Stohr, C. D. Carter and W. Meier, "*Flow-Flame Interactions Causing Acoustically Coupled Heat Release Fluctuations in a Thermoacoustically Unstable Gas Turbine Model Combustor*," Combust. Flame, 157(12) (2010), pp. 2250-2266.

[117] J. Canny, "A *Computational Approach to Edge Detection*," IEEE Trans. Pattern Anal. Mach. Intell., 8(1986), pp. 679-698.

[118] I. G. Shepherd, "*Flame Surface Density and Burning Rate in Premixed Turbulent Flames*," Proc. Combust. Inst., 26(1996), pp. 373-379.

[119] C. Ghenai, F. C. Gouldin and I. Gokalp, "*Mass Flux Measurements for Burning Rate Determination of Premixed Turbulent Flames,*" Proc. Combust. Inst., 27 (1998), pp. 979-988.

[120] A. N. Lipatnikov and J. Chomiak, "*Turbulent Flame Speed and Thickness: Phenomenology, Evaluation, and Application in Multi-Dimensional Simulations,*" Progress in Energy and Combustion Science, 28(2002), pp. 1-74.

[121] P. Griebel, P. Siewert and P. Jansohn, "*Flame Characteristics of Turbulent Lean Premixed Methane/Air Flames at High Pressure: Turbulent Flame Speed and Flame Brush Thickness,*" Proc. Combust. Inst., 31(2007), pp. 3083-3090.

[122] R. Sadanandan, M. Stohr and W. Meier, "*Simultaneous OH-PLIF and PIV Measurements in a Gas Turbine Model Combustor,*" Appl. Phys. B 90(3-4) (2008), pp. 609-618.

[123] H. Becker, P. B. Monkhouse, J. Wolfrum, R. S. Cant, K. N. C. Bray, R. Maly, W. Pfister, G. Stahl and J. Warnatz, "*Investigation of Extinction in Unsteady Flames in Turbulent Combustion by 2D-LIF of OH Radials and Flamelet Analysis,*" Proc. Combust. Inst., 23(1) (1990), pp. 817-823.

[124] M. Z. Haq, C. G. W. Sheppard, R. Woolley, D. A. Greenhalgh, and R. D. Lockett, "Wrinkling and Curvature of Laminar and Turbulent Premixed Flames," Combust. Flame, 131(2002), pp. 1-15.

[125] S. Zhu and S. Acharya, "*Dynamics of Lean Blowout in Premixed Combustion with Hydrogen Addition,*" Proc. ASME Turbo Expo 2012, Copenhagen, Denmark, GT2012-69189.

[126] Kuchta, J.M., "*Investigation of Fire and Explosion Accidents in the Chemical, Mining, and Fuel-Related Industries- A Manual,*" United States Department of the Interior, Bureau of Mines, Bulletin 680, 1985.

[127] S. H. Sung and C. K. Law, "*An Invariant Derivation of Flame Stretch,*" Combust. Flame., 55 (1984), pp.123–125.

[128] A. N. Lipatnikov and J. Chomiak, "*Effects of Premixed Flames on Turbulence and Turbulent Scalar transport,*" Prog. Energy. Combust. Sci., 36(2010), pp.1-102.

[129] R. K. Cheng and T.T. Ng, "*Velocity Statistics in Premixed Turbulent Flames,*" Combust. Flame., 52(1983), pp.185-202.

[130] R.K. Cheng, I.G. Shepherd and I. Gokalp, "*A Comparison of the Velocity and Scalar Spectra in Premixed Turbulent Flames,*" Combust. Flame., 78(1989), pp.205-221.

APPENDIX A: DETAILED SETUP FOR SYNCHRONIZED PIV AND PLIF MEASUREMENTS

In this chapter, the detailed experimental setup and procedure is described for synchronized PIV and PLIF measurements, along with phase-locked recording of fuel/air flow rates, temperatures, and photodiode signal. The following designed triggering scheme also includes phase-locked high speed flame imaging, which can be configured at a high framing rate and capture a certain number of flame chemiluminescence images before and after each triggering pulse. The measurement configuration will first be introduced, and then followed with the detailed operation procedure.

Measurement system and configuration

Figure A-1 shows the experimental setup diagram. The measurement systems mainly include a function generator (SRS DS345; used as a primary triggering source), IDT-PIV system, a high speed camera equipped with an intensifier, OH-PLIF system, and two additional computers – one used for recording data such as flow rates and the other for generating triggering signal for OH-PLIF system as a pulse delay generator. The goal is to synchronize the PIV measurement and OH-PLIF imaging, and at the same time, to take a certain number of flame images at high framing rates using a high speed camera before and after each triggering signal for OH-PLIF imaging. The corresponding timing diagram is shown in Figure A-2. Each OH-PLIF image is captured in the middle of the two PIV consecutive images.

In this test, PIV measurement and OH-PLIF imaging are operated at 5 Hz. The high speed camera will take 20 images at 2000 Hz framing rate before and after each PIV

image pair and OH-PLIF image. Detailed setting for each component of this measurement system is described as follows.
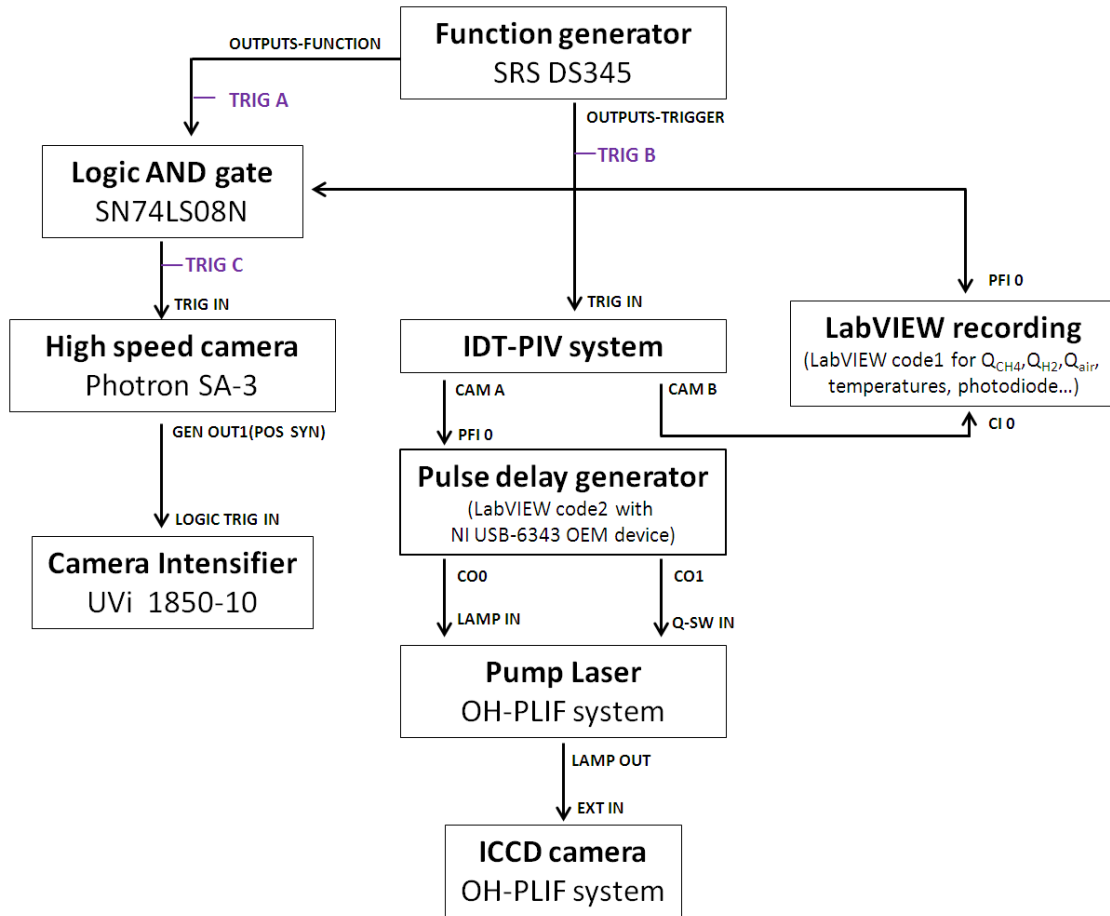

Figure A-1 Experimental setup diagram

The function generator, once configured, will generate the programmed waveform signal continuously, as shown as the square wave signal in Figure A-2. In order to produce triggering signal sources for high speed camera and other measurement systems having the exactly same starting point that can be controlled and given manually, Burst modulation is used, and a logic AND gate is implemented to synchronize these two triggering signals. The function generator SRS DS345 is then configured with a square function at 96 Hz (period =10.42 ms) and burst count at two. When sweep mode is off,

the FUNCTION OUTPUT will generate the specified square waveform only and continuously, and the real-panel TRIGGER OUTPUT signal goes low. When sweep mode is on by pressing the button "SWEEP ON/OFF", the FUNCTION OUTPUT will generate the pulse bursts of two square waveform cycles, and the TRIGGER OUTPUT will produce simultaneously TTL compatible signal that goes high when the pulse burst is on and low when it complete. By combining with these two signals with a logic AND gate, the triggering signal for high speed camera- the two-pulse burst signal as TRIG C in Figure A-2, and the triggering signal for PIV system – the TTL compatible signal as TRIG B in Figure A-2 – then can be manually controlled by pressing/depressing the sweep mode button in the front panel of the function generator.
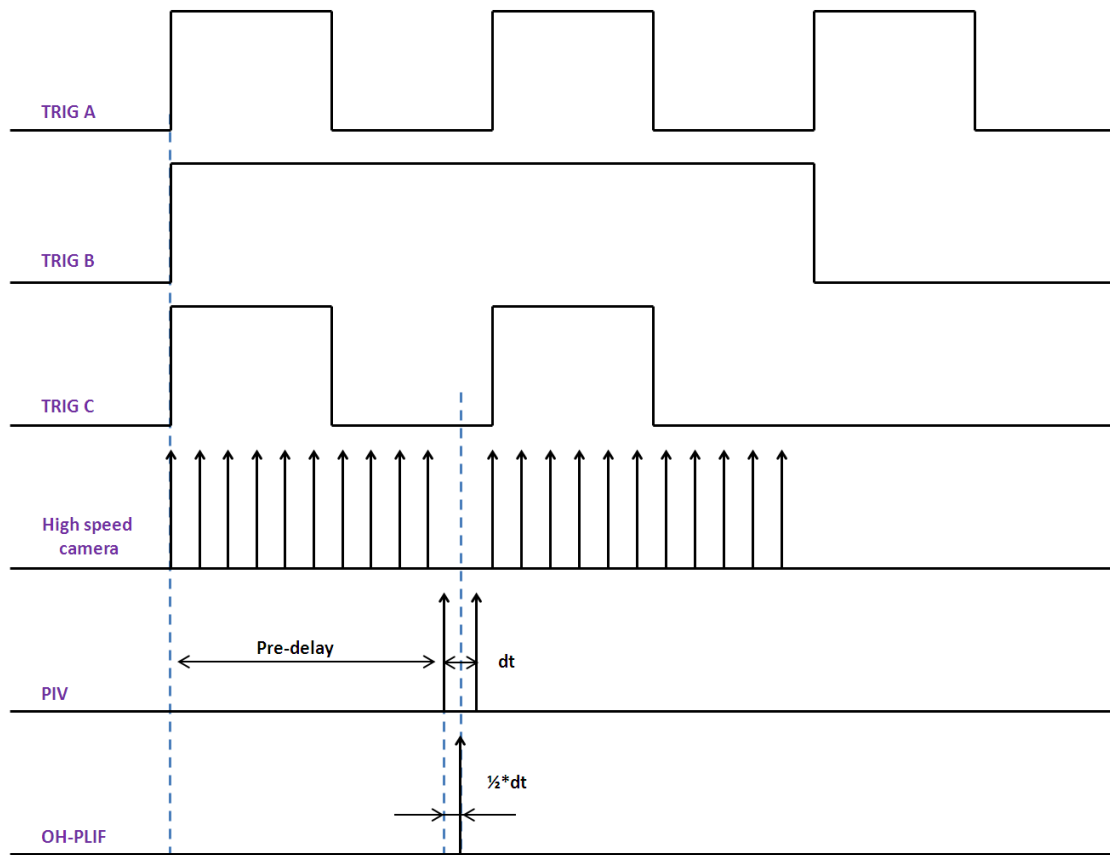

Figure A-2 Timing diagram

The high speed camera is configured at 2000 Hz framing rate, 768×768 resolution, reset Random-20 mode, trigger-in delay at 0 and general out1 at positive synchronized signal for synchronizing the UVi intensifier. It will start taking 20 images at 2000 Hz framing rate when the external triggering signal goes high.
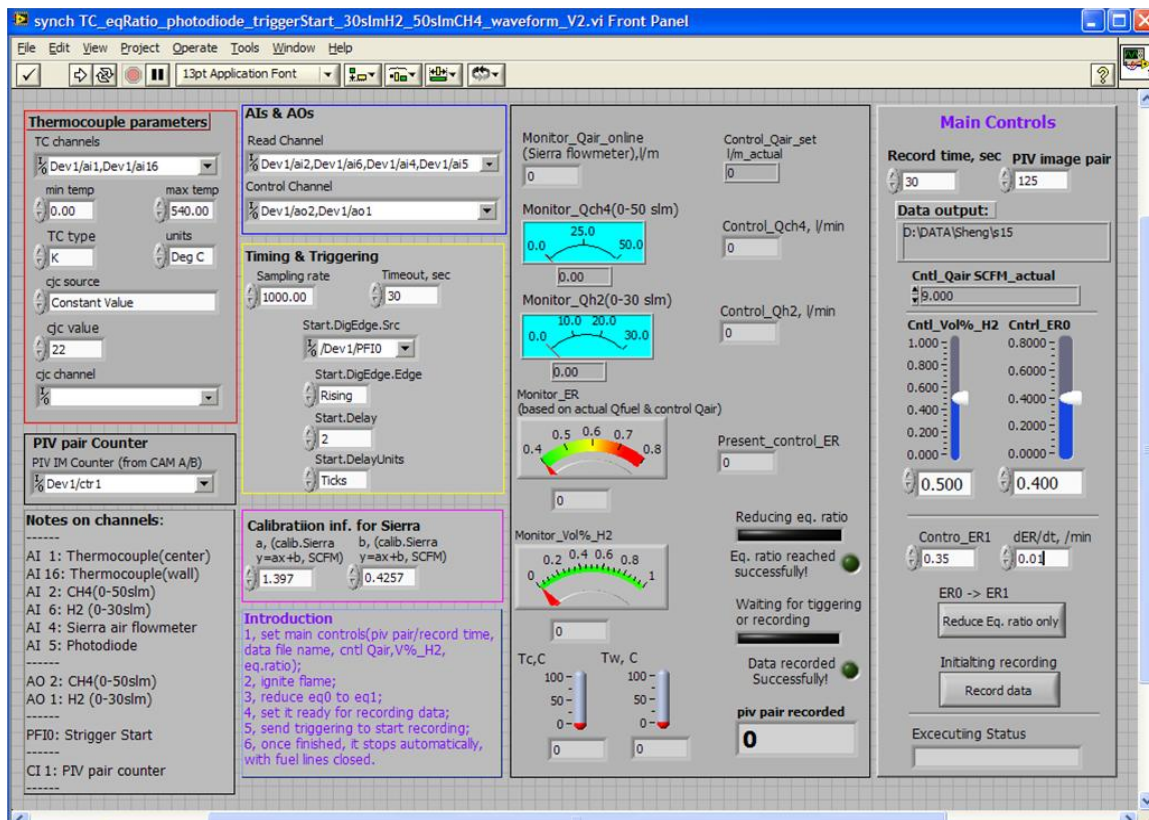

Figure A-3 Screenshot of LabVIEW code1 for data recording

PIV system is set in external trigger mode. The pre-delay is set at 10 ms, right after high speed camera finishes taking first 20 images. The time delay for PIV measurement, dt, is configured at 20 us. The synchronized camera A signal is then used to serve as external triggering signal for OH-PLIF system. And the synchronized camera B signal is used to count the PIV image number through the LabVIEW program, which

also records fuel/air flow rates, temperatures, and photodiode signals. The screenshot of the LabVIEW code1 is shown in Figure A-3.
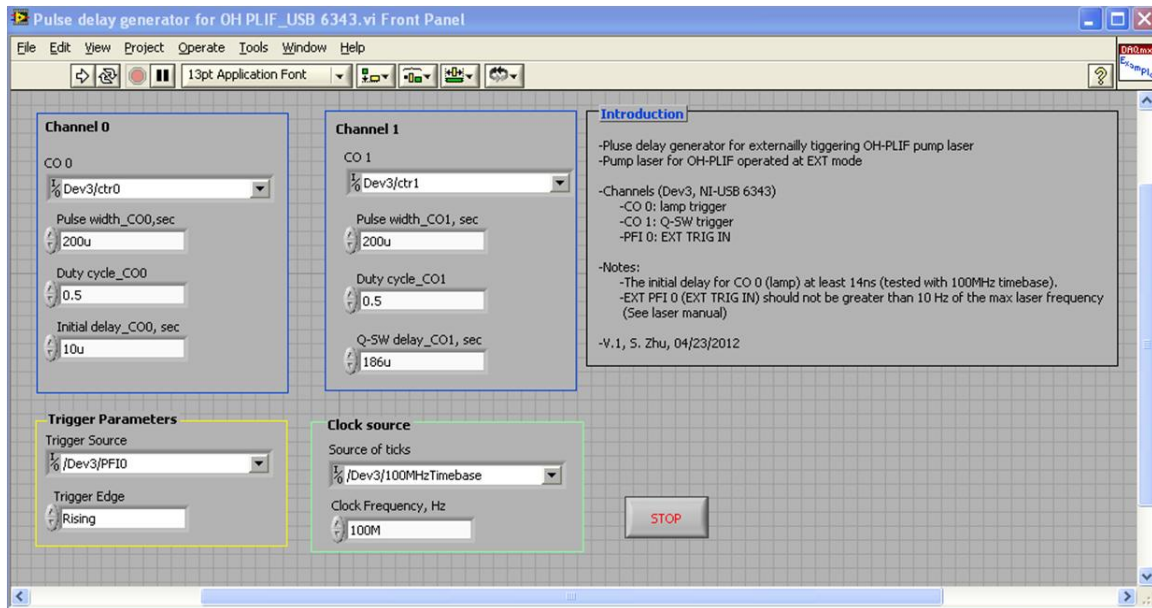

Figure A-4 Screenshot of LabVIEW code2: pulse delay generator

The pump laser for OH-PLIF system is operated at external trigger mode for both lamp and Q-switch trigger sources. These two triggering signals are generated by the labVIEW coded pulse delay generator whose input pulse is the synchronized PIV imaging signal. The screenshot of the corresponding LabVIEW code2 is shown in Figure A-4. To capture the PLIF images at the middle of two PIV consecutive images, the time delay between OH-PLIF imaging and PIV imaging is set 10 us, half of the time delay for PIV measurement.

Operation procedure

The operation procedures described here are steps after all measurement systems such as PIV and OH-PLIF systems are positioned, focused, calibrated and ready to take measurements.

1. Run LabVIEW code2- pulse delay generator-program;

2. Run LabVIEW code1-LabVIEW Recording-to set fuel flow rates and open fuel lines;

3. Ignite the flame, adjust equivalence ratios if needed, and monitor the center-body temperature through LabVIEW program, till it reaches the equilibrium value (the constant maximum temperature);

4. Enable external trigger mode for both lamp and Q-Switch for OH-PLIF pump laser;

5. Set ICCD camera for OH-PLIF imaging at gate mode, and enable image capturing in external trigger mode to ensure both laser system and imaging system are ready to taking measurement for external triggering;

6. Start PIV image pair recording in external trigger mode to ensure it is ready to take measurement for external triggering;

7. Arm UVi intensifier, adjust the gain if needed, and start high speed camera recording to ensure it is ready to capture images for external triggering;

8. Click the "Record data" button in LabVIEW code1to ensure the program will start recording data once the external triggering signal is received;

9. Slowly open PIV seeding particle line till it is fully open;

10. Turn on the sweep mode on the function generator by pressing the "SWEEP ON/OFF" button, to simultaneously start taking data;

11. Once the data collection is finished, the flame will be automatically turned off. Then close the PIV seeding particle lines; (Note: As soon as the PIV system finishes recording the pre-set number of image pairs, which is also counted by LabVIEW code1, the LabVIEW code1 program will automatically stop recording data and then shut down the fuel lines, and finally exit the program.)

12. Depress the "SWEEP ON/OFF" button in the front panel of function generator, to stop sending triggering signals;

13. Change the lamp and Q-switch back to internal mode for pump laser;

14. Put ICCD camera in safe mode, and save OH-PLIF image data;

15. Stop running UVi intensifier, and save image sequence captured by the high speed camera;

16. Save PIV image pair data;

17. Repeat above steps for different fuel mixtures and equivalence ratios.

VITA

Shengrong Zhu was born in Sanming, Fujian province, China, on October 10, 1981. He received a Bachelor of Science in Mechanical Engineering degree from Nanjing University of Aeronautics and Astronautics (NUAA), China, in 2005. In fall 2004 he entered the 3+2 program and started to pursue his master degree in NUAA, China. Since fall 2006, he attended Louisiana State University Graduate School to pursue his Doctor of Philosophy degree in mechanical engineering.